Fakultät für Medizin

Klinik und Poliklinik für Innere Medizin II

Analysis of Inflammatory and Mutational alterations in mouse models of Esophageal Carcinogenesis

Akanksha Anand

Vollständiger Abdruck der von der Fakultät für Medizin der Technischen Universität München zur Erlangung des akademischen Grades eines

Doctor of Philosophy (Ph.D.)

genehmigten Dissertation.

Vorsitzende/r: Prof. Dr. Thomas Korn

Betreuer/in: Prof. Dr. Michael Quante

Prüfer der Dissertation:

1. Prof. Dr. Angelika Schnieke

2. Priv.-Doz. Dr. Guido von Figura

3. Prof. Dr. Michael Vieth

Die Dissertation wurde am 30.08.2021 bei der Fakultät für Medizin der Technischen Universität München eingereicht und durch die Fakultät für Medizin am 11.10.2021 angenommen.

Dedicated to my mother, thank you for your hardwork, strong will and positive approach towards life.

Table of contents

List of Figures and Tables

Zusamenfassung

Barrett-Ösophagus (BE) ist die Vorläuferläsion des Adenokarzinoms des Gastro-Ösophagealen Übergangs (EAC) und korreliert mit dem Auftreten von gastroösophageale Refluxkrankheit (GERD). BE kann durch einen wiederholten Kontakt des squamokolumnaren Übergangs (squamous-columnar junction, SCJ) mit Magensäure und Gallensäuren entstehen und sich zu einer Dysplasie und letztendlich zum Adenokarzinom der Speiseröhre entwickeln. Bei der Entstehung von BE wird Plattenepithel an der SCJ durch Säulenepithel ersetzt. Obwohl die Inzidenz von EAC steigt und eine schlechte Prognose zur Folge hat, ist das Wissen über das Fortschreiten von BE zu EAC begrenzt. Ein tiefergreifendes Verständnis der Erkrankung ist daher von besonderer Bedeutung um bessere Krankheitsmodelle und Therapiestrategien entwickeln zu können. Ziel dieser Arbeit war es, ein besseres Verständnis der Mikroumgebung des Tumors und der BE-auslösenden Mutationen zu gewinnen. Dabei wurde mit einem genetischen BE Mausmodell gearbeitet, welches sich durch eine spezifische Überexpression von Interleukin-1beta (IL-1B) im Ösophagus auszeichnet. Diese Mäuse entwickeln zunächst Ösophagitis, dann Barrett Metaplasie und zuletzt Adenokarzinome des Ösophagus.

Stromazellen spielen eine wichtige Rolle in der Mikroumgebung des Tumors. Die Aktivierung des NF-kB Signalweges in dieser Mikroumgebung setzt Entzündung und Krebsentstehung in Verbindung. Um die Interaktion zwischen entzündlichen Epithel- und Stromazellen zu untersuchen entwickelten wir das Mausmodell L2-IL-1beta.Vim-CreTM.p65, in dem der NF-kB-Signalweg in Vimentin+-Stromazellen ausgeschaltet ist. Das Mausmodell wurde charakterisiert und der Phänotyp der Mäuse auf makro- und mikroskopischer Ebene erfasst. Die gezielte Abschaltung von NF-kB mildert den schweren dysplastischen Phänotyp bei IL-1beta-Mäusen ab und verringert die Entzündung und Proliferation von Epithelzellen an der SCJ. Zudem konnten wir in humanen und murinen 3D-Organoid-Modellen ein eingeschränktes Migrationspotential von NF-kB-gehemmten Fibroblasten im Vergleich zu den NF-kB-ungehemmten Fibroblasten zeigen. Daraus schlossen wir, dass in einer entzündlichen Umgebung der NF-kB in Stromazellen aktiv ist und, dass das Fortschreiten von BE durch eine Ausschaltung des NF-kB-Signalweges verringert werden kann. Zudem

lässt sich vermuten, dass Stromazellen ein therapeutisches Potential zur Behandlung von BE haben könnten.

Die Entstehung von BE und -progression zu EAC ist ein multimodaler Prozess, der durch verschiedene Aspekte wie Ernährung, Mikroumgebung und Genetik beeinflusst wird. In unserem zweiten Ansatz konzentrierten wir uns auf die Analyse der Auswirkungen verschiedener Mutationen auf die Entwicklung von BE. Auf der Grundlage von Erkenntnissen aus Genomsequenzierungsdaten menschlicher EAC-Patienten haben wir drei Gene - KRas, TP53 und Rb - ausgewählt, um ein Mausmodell für EAC zu erstellen. Es hat sich gezeigt, dass diese Gene bei EAC häufig mutiert und an entscheidenden Signalwegen für die Karzinogenese beteiligt sind. Das IL-1beta überexprimierende BE-Mausmodell zeigt eine Expansion von Vorläuferzellen am squamokolumnaren Übergang (SCJ), welche maßgeblich am Fortschritt der Erkrankung beteiligt ist. Basierend auf diesem Wissen induzierten wir die Mutationen spezifisch auf expandierenden Lgr5+-Stammzellen. Zur Erzeugung des mutationsgetriebenen Mausmodells kreuzten wir L2-IL-1b-Mäuse mit Lgr5-CreERT-Mäusen (L2-L). Diese Mäuse wurden dann mit KRas (K), p53 (P) und Rb (R) gekreuzt, um einfach (L-LK, L2-LP, L2-LR), doppelt (L2-LPR, L2-LKP, L2-LKR) und dreifach mutierte (L2-LKPR) Modelle zu erzeugen. Wir analysierten und charakterisierten diese Mäuse makroskopisch und histopathologisch. Zur Untersuchung der Modulationen in homogenen Epithelzellen nutzten wir außerdem aus den Mäusen isolierte 3D-Organoide. Zusammenfassend lässt sich sagen, dass wir ein mutationsgetriebenes L2-LKPR-Mausmodell entwickelt haben, bei dem sich innerhalb von 6 Monaten basierend auf der durch IL-1beta Überexpression bestehenden Metaplasie ein invasives Karzinom bildete, das dem menschlichen EAC ähnelt und die Stadien der des Fortschreitens von BE zu EAC zeigt. Dieses Mausmodell ist ein hervorragendes Instrument, um verschiedene chemotherapeutische und medikamentöse Therapien zur Behandlung des Ösophagus-Adenokarzinoms zu erforschen.

Diese Arbeit zeigt die Bedeutung der Interaktion zwischen Stroma- und Epithelzellen und die Rolle von NF-kB bei der Beschränkung und Förderung des stromazellabhängigen Wachstums von BE. Sie veranschaulicht auch die Rolle stammzellspezifischer Mutationen bei der Beschleunigung der Entwicklung von BE zu EAC.

Abstract

Barrett's esophagus is the replacement of the squamous epithelium with the columnar epithelium. It is a premalignant condition of the distal esophagus. BE is the precursor lesion, which means it can progress to dysplasia and further to esophageal adenocarcinoma. Gastroesophageal reflux disease has been strongly correlated with the occurrence of BE/EAC. Repeated exposure of gastric acid and bile reflux creates an inflammatory environment at the squamous-columnar junction, which changes the mucosa and causes BE. The rising incidence and limited knowledge of the advancement of the disease make it very critical to understand. There is an urgent need to understand the mechanisms of the disease to develop treatment strategies and provide new tools and models to study the disease.

This thesis aims to provide tools in the form of unique mouse models to understand the tumor microenvironment and genetic mutations that drive BE. To investigate both these aspects, we utilized the IL-1beta overexpression mouse model for BE. This mouse model induces inflammation in the basal epithelial cells in the squamous esophagus which, causes metaplasia and dysplasia specific in the esophagus and stomach.

Stromal cells play an important role in the tumor microenvironment and, NF-kB is one of the pathways which link inflammation and cancer. Therefore, we eliminated the NF-kB signalling pathway in the vimentin+ stromal cells to study the interaction between inflammatory epithelial and stromal cells. We generated a mouse model for the same termed as L2-IL-1beta.Vim-Cre^{TM}.p65. We characterized these mice, analysed the phenotype and described the model with macroscopic and microscopic techniques. We also implemented 3D- tissue culture systems in mouse as well as human settings. The results showed us that NF-kB elimination attenuates the severe dysplastic phenotype in IL-1beta mice. It also shows a decreased inflammation and proliferation of epithelial cells at the SCJ. This inference was also supported by the 3D organoid cultures wherein the migration potential of NF-kB inhibited fibroblasts was limited compared to the NF-kB non-inhibited fibroblasts. This was also replicated in the human organoids as well. Hence, we concluded that NF-kB plays an active role in the movements of stromal cells of the inflammatory environment. By eliminating this pathway, it is possible to reduce the progression of BE. Hence, this study shows that

stromal cells could be a potential target to develop new therapeutic strategies in the treatment of BE.

Disease initiation and progression is a multimodal process that affects various aspects, including diet, microenvironment, and genetics. In our second approach, we focussed on analysing the effect of different mutations in the development of BE. From the knowledge of genomic sequencing data on human EAC patients, we selected three genes, KRas, TP53 and Rb, to generate a mouse model for EAC. These genes have been seen to be frequently mutated in EAC and also participate in crucial pathways involved in cancer progression. BE model of IL-1beta overexpression shows an expansion of progenitor cells at the SCJ with the disease progression. We utilized this knowledge and selected Lgr5+ stem cells to induce the three mutations. To generate the mutation-driven mouse model, we crossed L2-IL-1b mice with Lgr5-CreERT mice (L2-L). These mice were then crossed with KRas (K), p53 (P) and Rb (R) to generate single (L-LK, L2-LP, L2-LR), double (L2-LPR, L2-LKP, L2-LKR) and triple mutated (L2-LKPR) models. We analysed and characterized these mice macroscopically and histopathologically. We also generated 3D organoid model systems for these mutations to investigate the modulations in homogenous epithelial cells. To summarize, we developed a mutation-driven L2-LKPR mouse model that progressed to invasive carcinoma resembling human EAC in 6 months and showcases the stages of initiation, mediation, and advancement from BE to EAC. This model is a poignant tool to uncover various chemotherapeutic and drug targeted therapies to treat esophageal adenocarcinoma.

This study portrays the importance of stromal-epithelial cell interaction and the role of NF-kB in restricting and promoting the growth of stromal cell-dependent development of BE. It also illustrates the role of stem cell-specific mutations in accelerating BE to EAC.

Aims of the Project

AIM I: To study and characterize the effect of elimination of NF-kB signalling in vimentin+ stromal cells on a BE transgenic mouse model

The main objective of this aim is to genetically eliminate NF-kB signalling in Vimentin+ stromal cells and to study the importance of stromal cells' activation on tumorigenesis progression by utilizing the L2-IL-1b overexpressing BE transgenic mouse model, discussed in chapter 3.

AIM II: Generation and Characterization of mutation-driven esophageal adenocarcinoma transgenic mouse models and to outline the role of distinct mutations during carcinogenesis

The main objective of this aim is to focus on the role of key driver mutations such as p53, Rb, KRas and p16 in accelerating the progression from BE to EAC in the L2-IL-1b mouse model and to give an insight into the mutational heterogeneity of esophageal adenocarcinoma, discussed in chapter 4.

Chapter 1: Introduction

1.1 The Esophagus

1.1.1 Anatomy and Physiology

The esophagus is an 18-26 cm long tubular structure that connects to the stomach's oral cavity. The primary function of the esophagus in the human body is to propel the food or liquid through active peristalsis into the stomach for digestion and absorption. Unlike the rest of the GI tract, the esophagus wall lacks a serosal layer but is mainly composed of a thin layer of connective tissues. The inner wall, however, is composed of mucosa, submucosa and muscularis propria. The mucosa comprises stratified squamous epithelium, which is further classified into three sublayers: mucous membrane, lamina propria and muscularis mucosae [1]. The squamous epithelium extends to the lower esophageal sphincter (LES), where it joins with the gastric columnar epithelium [2], as shown in Figure 1.1.1.

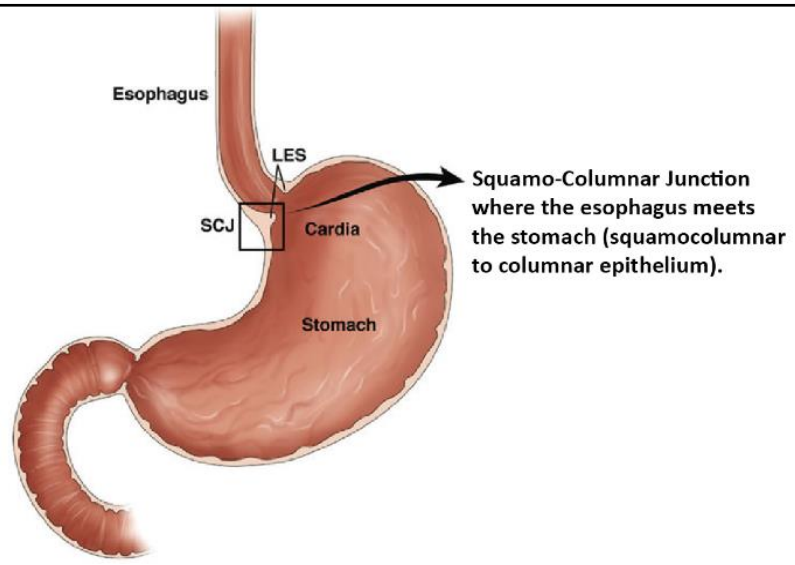

Figure 1.1.1: Anatomy of the human esophagus and stomach.
The esophagus is a muscular tube that connects the pharynx with the stomach. SCJ is the junction where esophagus connects to the stomach, and LES is the sphincter where the squamous epithelium joins with the gastric columnar epithelium. Figure adapted and used with permission from M. Quante [3].

The LES is a high-pressure zone that is under the influence of hormones intrinsically and respiratory pressure via the diaphragm extrinsically. Any abnormality in this zone can result in symptoms like dysphagia, chest pain or heartburn. These dysfunctions can lead to esophageal motility disorders

such as achalasia, distal esophageal spasm and the most common and crucial one of them, gastroesophageal reflux disease [4].

1.1.2 GERD

Gastroesophageal reflux disease (GERD) is a common occurrence that affects 10-20% of the Western population and around 5% population of Asia. As encountered by primary care physicians and gastroenterologists, this prevalence has been perceived to be increasing [5, 6]. This condition mainly arises from repeated reflux of stomach contents into the esophagus, which leads to mucosal damage in the distal esophagus. The symptoms for GERD can be subdivided into typical, atypical and extraesophageal symptoms. The most typical and common symptom includes heartburn and acid regurgitation. Atypical symptoms include gastric pain, belching, bloating and nausea. A severe GERD symptom can be seen as chronic cough, laryngitis and dental erosions [7].

GERD is suspected to be one of the primal causes of chronic inflammation in the esophagus. This condition is termed esophagitis [8]. GERD is considered one of the main causative reasons for the development of the Barrett Esophagus (BE). However, only 5-10% of patients with GERD are diagnosed with BE [9]. But the increased risk of chronic GERD enhances the chances of BE. The increasing rate of obesity has been directly related to the occurrence of GERD. Although there has not been a clear mechanism to prove this, it has been hypothesized that an increase in visceral fat causes an increase in reflux disease. This eventually damages the squamous-columnar junction between the stomach and the esophagus and causes malignant changes in the basal cells of the distal esophagus. It has been postulated that visceral abdominal fat results in the release of specific cytokines such as IL-1β, IL-6, TNF-α, which can be directly linked to the initiation of BE [10, 11]. Even though other factors also play a role in causing damage to the esophageal mucosa, such as high-fat diet and alcohol intake, GERD plays a crucial role in esophagitis, leading to BE and carcinogenesis [12, 13]. However, the exact mechanism and pathway remain to be understood.

1.1.3 Barrett Esophagus and Esophageal Adenocarcinoma

Barrett's esophagus is a condition of chronic inflammation which is a result of severe mucosal injury. Norman R. Barrett described BE as columnar lining in epithelium which is ‘‘histologically gastric in type’’ [14]. In humans, this injury is mainly caused by GERD, in which there is repeated exposure of the squamo-columnar junction to the gastric acid [11]. The esophageal lining is made up of stratified squamous epithelium. On continuous exposure to gastric acids, inflammation is induced in this region to repair the tissue injury; the squamous epithelium is replaced metaplastically with columnar epithelium [15].

Earlier it was believed that BE results from the extension of the proximal esophageal epithelium to the SCJ [14, 16]. However, recent advancement in the disease's understanding suggests that the damage to the distal esophagus causes the influx of progenitor cells from the cardia to the esophagus [11, 17, 18]. However, it is still uncertain which cells are the cells-of-origin for BE, but the fact that BE is the precursor condition prevails before the onset of EAC has been proven and established [8].

Esophageal adenocarcinoma is one of the two subtypes of esophageal cancer. In the past years, it has become the predominant subtype because of its rapid increase. EAC accounts for 50% of all esophageal cancer [19]. The overall incidence rate of EAC has increased from 1.8 to 3.9, which is almost 7.6-fold higher in risk over the last decades [20]. EAC currently ranks as the eighth most common cancer worldwide, with an overall mortality rate of 5.3%. However, due to the uneven sex distribution, it is more predominant in males than in females [21]. The various risk factors for EAC include GERD, obesity and smoking. One of the effects of these risk factors is the alteration of the microbiome at SCJ, which accelerates the progression of the disease [22]. However, these microbial changes are still being explored.

The significance of BE lies in the fact that 0-4-0.5% BE patients per year develop EAC [23]. Hence, it is essential to detect BE and start an early treatment therapy for BE to prevent the advancement of the disease. However, the average age of diagnosis is 55 years which is too late for the patients to respond to therapies hence increases the risks for the patients with overall 5-year survival of <15% [20, 24]. This lifetime risk of BE, which progresses to EAC, is about 5% [9]. Hence, it is crucial to detect the onset of the disease and detect it soon enough.

The risk factors associated with EAC can be classified as genetic and non-genetic factors. The genetic factors include germline and somatic mutations. Approximately 7% of BE and EAC cases are hereditary and occur within families [25]. The most common driver mutations that are associated with EAC in various genome-wide studies are TP53, CDKN2A, SMAD4, KRAS, PIK3CA [24]. The non-genetic factors mainly include obesity, GERD, smoking, excessive alcohol intake and intake of dietary fat. Current findings suggest that excess body weight and energy consumption are important risk factors for EAC development. The prevalence of obesity and GERD together accelerates the development of EAC. Hence there is an urgent need to identify the high-risk patients and develop protocols to extend the disease-free survival.

1.1.4 Disease Progression and Hypothesis

The progression of the disease from BE to EAC initiates with chronic inflammation, also called esophagitis at the SCJ. Chronic inflammation gives rise to BE, which further advances to EAC.

However, according to histopathology, in between BE and EAC, there are stages of metaplasia, low-grade dysplasia and high-grade dysplasia, as shown in Figure 1.1.4a. Metaplasia is graded for the presence of mucous cells and metaplastic glands, whereas dysplasia is scored as the structural abnormalities, the architecture of the epithelial cells and their granular complexity [26]. Furthermore, EAC can be classified as different grades depending on the differentiation of the cells and the infiltration of these cells to different epithelial and mucosal sublevels. At a later stage, EAC can also be sub-classified based on metastasis [27].

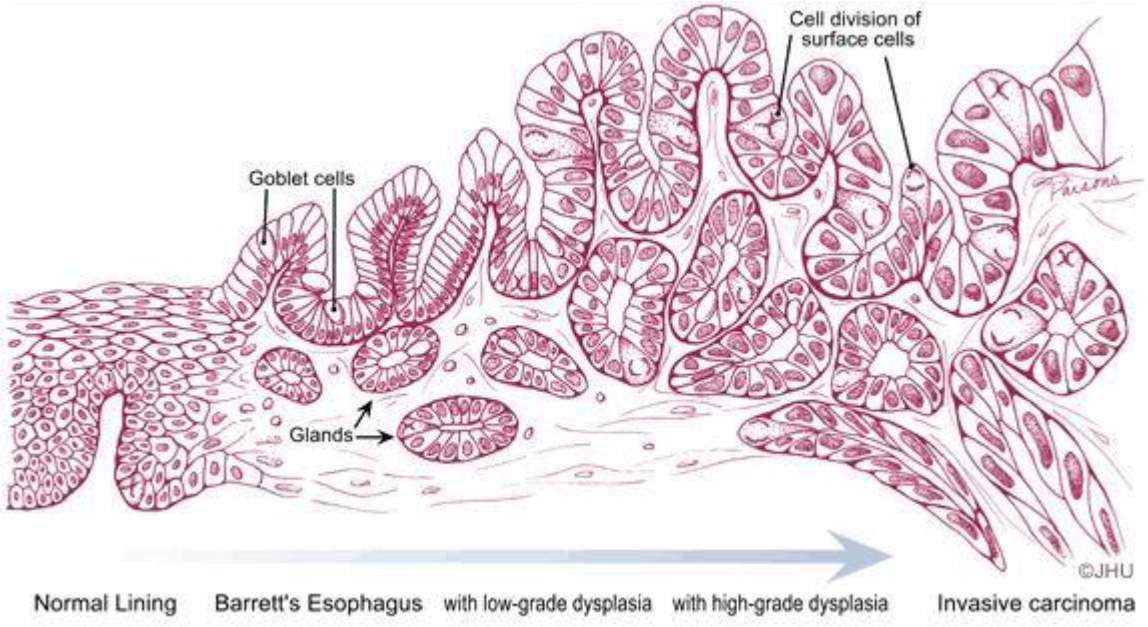

Figure 1.1.4a: Schematic representation of the disease progression

Development of the disease from the normal squamous esophageal lining to invasive carcinoma along with the intermediate stages of Barrett's esophagus, low-grade dysplasia and high-grade dysplasia [28]

The fact that BE replaces squamous with the columnar epithelia and is a precursor of EAC is established. However, the origin of BE is still in question. There have been various hypotheses and speculations to identify the basis of the advancement of the disease. Figure 1.1.4b illustrates very closely some of the current hypotheses which explain the pathogenesis of BE.

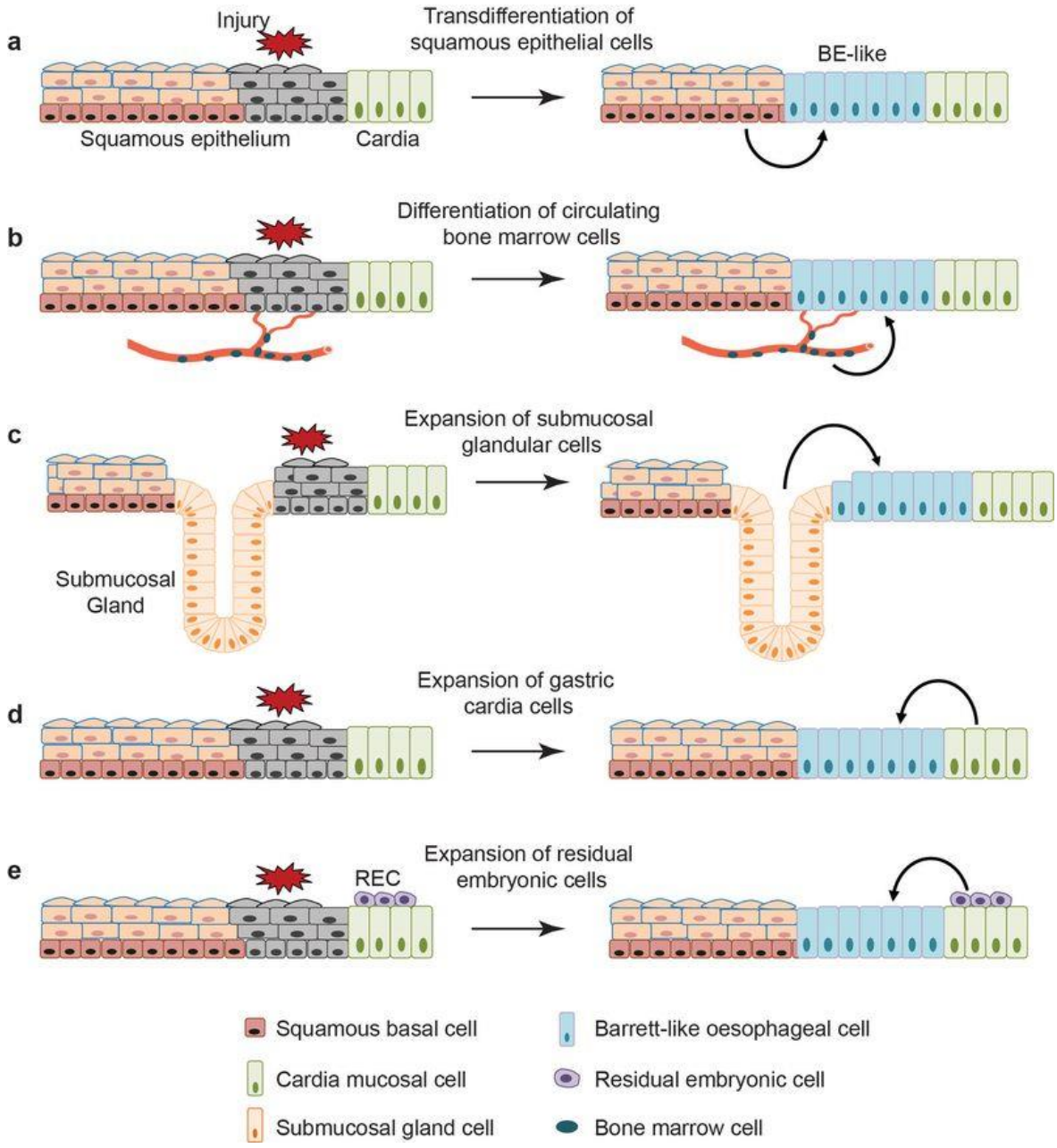

Figure 1.1.4b: Different models illustrating the pathogenesis of BE

A: Transdifferentiation of squamous epithelial cells, **B:** Differentiation of circulating bone marrow cells, **C:** Expansion of submucosal glandular cells, **D:** Expansion of gastric cardia cells, **E:** Expansion of residual embryonic cells. The figure is taken from [29]

On tissue injury, the transdifferentiation of squamous epithelium occurs, which results in BE-like columnar epithelium. Transdifferentiation is the switch from one type of differentiated cell to another type with or without any cell division in between [30]. Another hypothesis shows bone-marrow derived

cells (BMDCs) circulate through the peripheral organs and reach the site of inflammation or injury. The presence of these cells at the SCJ shows the contribution of stem cells in neoplastic lineages [31]. A study on irradiated rats used bone marrow transplantation and esophagojejunostomy to induce BE. The results showed that circulating BMDCs could contribute to the formation of intestinal metaplasia in the esophagus [31]. This study indicates that multiple progenitor cells originate from bone marrow to induce esophageal regeneration [31].

Another hypothesis claims the expansion of submucosal glandular cells as the origin of BE. Multipotent progenitor cells in submucosal gland ducts at the base of the squamous epithelium reprogram themselves when triggered by injury. This tissue injury leads them to differentiate into columnar epithelium [8, 11, 32, 33]. It has been shown that the transition from the submucosal gland to BE epithelium is followed by a gradual morphological change of the duct cells to the columnar epithelium in humans [34]. The metamorphosis can trigger tumor suppressor genes (mainly p53 and p16) in stem cells, leading to metaplasia [32, 34]. This hypothesis can explain the heterogeneity of the disease as it arises from multiple independent clones instead of being monoclonal [8, 34].

Apart from the expansion of submucosal cells, a hypothesis suggests the expansion of residual embryonic cells to the SCJ. These cells can migrate to the site of inflammation and induce Barrett metaplasia on tissue injury [8, 35]. It has been found out that there is a population of KRT7+ cells at the SCJ. A recent study demonstrated through lineage-tracing experiments that cells which were p63+KRT5+KRT7+ contribute to BE at SCJ [29].

Even though there are several different approaches to understand and explain the origin of BE, this thesis is based on the hypothesis that when there is inflammation at the distal esophagus, which joins the proximal stomach known as the gastric cardia, a number of different progenitor cells expand at this junction. Among these progenitor cells, a particular stem cell population expressing Lgr5 actively responds to this imbalanced state, leading to higher production and accumulation of these Lgr5+ stem cells at SCJ in the human cardia and BE [11, 36-38].

1.2 Tumor Microenvironment

Tumor cells are surrounded by different types of other cell types that provide a sustainable environment to malignant cells and help them survive and proliferate. These cells create a niche which is termed as tumor microenvironment (TME). The tumor microenvironment differs from the normal extracellular matrix with respect to the cellular interactions between the tumor cells and the cells in the TME. The tumor microenvironment is infiltrated with inflammatory immune cells, blood

vessels and stromal cells. Each of these cell types has different cellular and molecular interactions with the tumor cells and hence affect the expansion of TME.

1.2.1 Immune cell infiltration in Tumor Microenvironment

The link between inflammation and cancer is well established. Inflammation induces various pro-carcinogenic mediators in the tumor niche [39]. These mediators recruit immune cells such as T-cells, dendritic cells, Natural killer (NK) cells, Tumor-associated macrophages (TAMs), and Myeloid-derived suppressor (MDSCs) cells which secrete a series of cytokines and chemokines that contribute to the development of tumor growth. Cytokines such as IL-6, IL-4, IL-10, IL-13 and TGF-β modulate the immune response and regulate tumor development [40]. Neutrophils serve as the first line of defense against invasion. Tumor-associated neutrophils play a pivotal role in tumor angiogenesis and metastasis. These cells release an array of cellular molecules such as FGF-2, VEGF, CXCL1, CXCL8, CCL3, CCL4, which are involved in remodelling the extracellular matrix surrounding the tumor cells [41]. On the other hand, macrophages play an essential role in the maintenance of a chronic inflammatory environment. The growth factors released from tumor-associated macrophages (TAMs) such as PDGF, TGF-β, IL-10, and PGE2 initiate tissue remodelling and vasculature, which promotes tumor development [40]. NK cells, however, control the growth of the tumor. They are involved in the immunosurveillance of the tumor site. They release chemokines such as CCR2, CCR5, CXCR3 to suppress tumor growth [42]. Hence, immune cells have a vast contribution to maintain the tumor niche and support cell survival and development.

1.2.2 Role of Stromal cells in Tumor Microenvironment

Apart from the immune cells, stromal cells are also an integral part of the inflammatory milieu. Stromal cells in interaction with the tumor niche execute mechanisms that promote angiogenesis, proliferation, cancer progression and immunosuppression. The most predominant stromal cells are fibroblasts and myofibroblasts (MF), which are important residents of the aberrant microenvironment [39, 43, 44]. Fibroblasts in their quiescent state express Vimentin and desmin, however when stimulated, they also express a-SMA additionally [45, 46]. These a-SMA expressing activated fibroblasts are called myofibroblasts [47]. MFs resemble cancer-associated fibroblasts; however, CAFs have altered biology, and they appear only in the tumor niche and not in the typical setting [48]. A shift in the epithelial homeostasis triggers a stromal reaction against the tumor. Upon this stromal reaction during the wound healing, the myofibroblasts undergo apoptosis, whereas they continue to exist at the tumor site [49]. Furthermore, tumors which are surrounded by a desmoplastic stroma have a poor prognosis [50]. Also, according to a study, the tumors with a high number of MFs

show a shorter disease-free survival rate [51], making MFs a potential prognostic marker and clinically relevant.

1.2.3 Role of NF-kB in carcinogenesis

NF-kB is one of the classical pathways which is linked to inflammation and cancer. This signalling pathway modulates a myriad of cellular processes. The initiation of this pathway is regulated by IkB family members. Once the stimuli activate the signalling, the downstream NF-kB targets get phosphorylated and translocated to the nucleus to regulate the transcription of the genes involved in immune and inflammatory responses [52]. The classical or the canonical NF-kB pathway gets activated by proinflammatory cytokines TNF-a, IL-1b, TLRs or viruses [53, 54]. These stimuli activate the intermediate kinases in the cytoplasm, which phosphorylates RelA (p65). The phosphorylated p65 translocates to the nucleus to further participate in gene regulation for cell survival or innate immunity. NF-kB is a critical player in promoting tumorigenesis in several cancer types [55-57]. The chemokines and the cytokines released at the site of inflammation triggers NF-kB signalling. This can further proceed to inhibit apoptosis, either by the regulation of anti-apoptosis proteins [58] or by accumulating reactive oxygen species (ROS) [59]. However, both these mechanisms promote tumorigenesis.

1.3 Mutagenesis in Esophageal Adenocarcinoma

Mutations are genotypic alterations in the nucleotide sequences of the DNA. They are capacitated to incorporate structural changes in the chromosomes, which can cause phenotypic alterations and may result in malignancy. On the basis of occurrence, mutations can be broadly classified into two types: Germline mutations, which are hereditary and can be passed over generations, and somatic mutations, which are not inherited but are developed during an individual's life [60]. It is essential to track down these aberrations to improve the prognosis, diagnosis and future therapies of a disease.

From a mutational perspective, esophageal adenocarcinoma is a highly heterogenous disease with a high mutational burden [18, 24]. This means that EAC is not mutation-specific. It involves several mutations combined for the progression of the disease. This pool of mutations can vary from patient to patient. Through exome and whole genome sequencing on patient biopsies, there has been an effort to identify the potential driver mutations and passenger mutations. Although based on this genetic knowledge, there have been two theories that explain EAC's clonal evolution from its precursor BE. One theory suggests that a single driver mutation is at an advantage. This mutation forms a clonal niche and is present in most of the cell population, which expands to the SCJ. This event has been termed as selective sweep. Once this particular mutation gets induced in the cells,

they are accompanied by other advantageous mutations which cause clonal expansion at SCJ. This accumulation of mutations causes EAC [61, 62]. Another theory proposes that there is a competition between these clones in the heterogenous mutational environment wherein multiple independent clones exist. Whatever of these mutations survive creates the genetic aberrations, leading to a more heterogenous BE and EAC clonal niche [34].

According to the data collected from whole-genome and exome sequencing from different EAC patients in separate studies, some of the most relevant mutated genes in EAC were TP53, CDKN2A and SMAD4. And the most potential amplifications were observed for ERBB2, KRAS, EGFR and VEGF genes [18, 24, 63, 64].

1.3.1 L2-IL-1b

IL-1 beta is a pro-inflammatory cytokine that is released with the onset of inflammation. A high concentration of these cytokines has been seen to be released in the squamous mucosa of human BE patients. This projects IL-1 beta as an important factor involved in the progression of BE to EAC [65].

The transgenic interleukin (IL) -1 beta mouse model (L2-IL-1b mouse model) is a model for esophagitis that progresses to BE and eventually to EAC. This mouse model was developed and established at Columbia University, USA, in the lab of Dr. Timothy C. Wang by Dr. Michael Quante. The model possesses the “modified human IL-1b cDNA downstream of Epstein-Barr virus (ED-L2), which is a promoter that targets the in the basal epithelial cells in the squamous esophagus, i.e., oral cavity, esophagus and squamous forestomach”, as shown in Figure 1.3.1 [11]. These mice show moderate inflammation and hyperplasia at 6 months, which develops to high-grade dysplasia until 18-20 months [11].

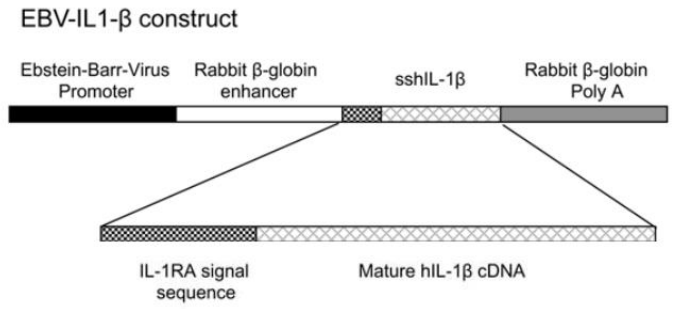

Figure 1.3.1 Generation of human IL-1beta transgenic mice: Human IL-1beta transgenic mice were generated by targeting the expression of the h-IL-1beta gene in the esophagus and stomach using the Epstein Barr virus promoter [11].

1.3.2 KRas

KRas, when it gets mutated, behaves as an oncogene. It is frequently mutated in human cancers. The statistics reveal that 95% pancreatic ductal adenocarcinoma, 50% colon cancers, and 30% non-small-cell lung cancers have shown RAS pathway activation, which otherwise remains inactivated in normal conditions [66]. RAS is responsible for the hydrolysis of GTP to GDP through GTPase activity in cell processing. When RAS gets mutated, it disrupts GTPase activity which affects various downstream signalling pathways. RAS regulates several cellular activities such as proliferation, survival, differentiation, migration and extracellular communication. When this protein gets mutated, all these pathways get dysregulated, which causes the accumulation of RAS protein that interferes with the cell cycle and cell survival [67, 68]. The wild-type and mutant KRas pathway have been illustrated in Figure 1.3.2a.

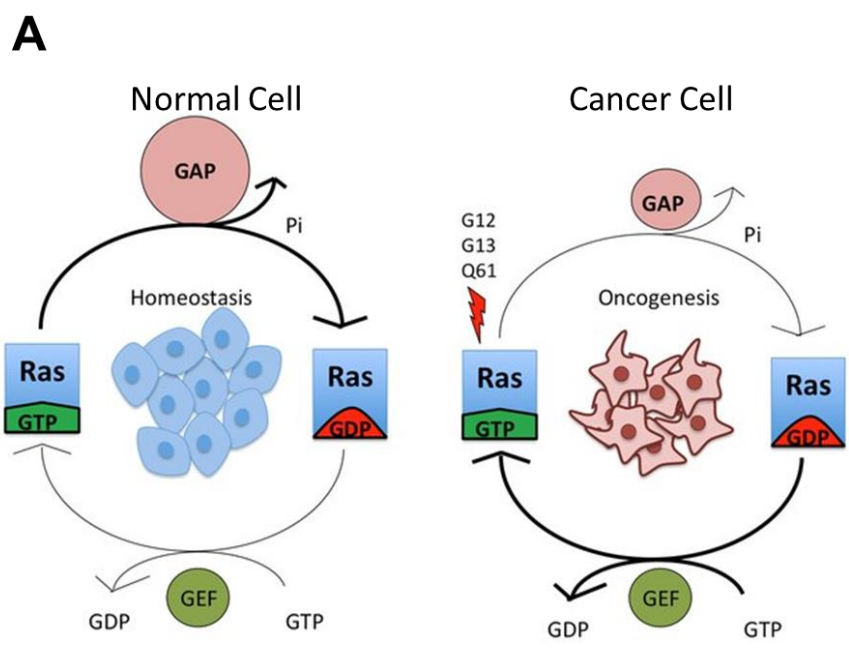

Figure 1.3.2a Diagrammatic representation of Wild-type and mutant KRas pathways [69].

The high importance but limited understanding of the biology of this gene led to the generation of a mouse model with a KRasG12D gene construct to induce the amplification of the RAS protein in different cancer types. The gene is located on chromosome 12 at exon 1. The model used the conditional cre-lox system to induce the gene expression at the desired site in the body depending on the cancer type [70]. Hence, the allele name is KRastm4Tyj, which remains inactive in normal conditions, but when the stop cassette is excised, the KRas allele gets activated, as shown in Figure 1.3.2b.

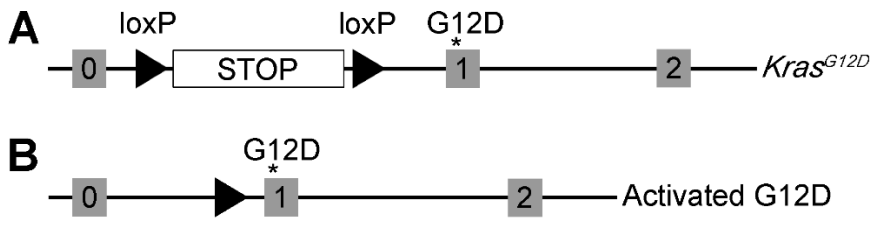

Figure 1.3.2b: Schematic representation of KRas alleles in transgenic mice

(A) KRas allele located within exon 0, 1 and 2 under the KRas locus, (B) On activation, the STOP cassette gets excised and leads to KRas G12D activation [71]

1.3.3 TP53

TP53 is a tumor suppressor gene. It is one of the most common tumor suppressor genes which have been found to have a loss of function in 50% of human cancers [72]. In EAC, p53 has been identified as a risk factor for the progression from BE. It is one of the gene markers recurrent in non-dysplastic BE patients who have progressed to EAC [73]. P53 is activated to respond to stimuli such as DNA damages through therapeutic drugs or radiations, viral oncogenes or hypoxia. The main focus of p53 protein is to regulate the cell cycle function. As a response to the stimuli, p53 undergoes specific changes involved in controlling the transition from phase G1/S to G2/M. The effects of p53 control include DNA repair, programmed cell death or apoptosis, senescence, autophagy and genomic stability [74, 75]. Hence these functions of p53 prevent premalignant lesions. However, when the function of this gene is disturbed, it leads to uncontrolled cell proliferation, which might lead to malignancy, as shown in Figure 1.3.4c.

P53 has been already used to generate transgenic mouse models. The gene is located on chromosome 11 and a conditional p53 mouse model is used based on the cre-lox system where the lox P sites flank the gene between intron 1 and 10 (Trp53tm1Brn). Upon activation of Cre recombinase the p53 gene between intron 1 and 10 is excited inducing a conditional elimination of p53 protein ceases [76] as shown in Figure 1.3.3.

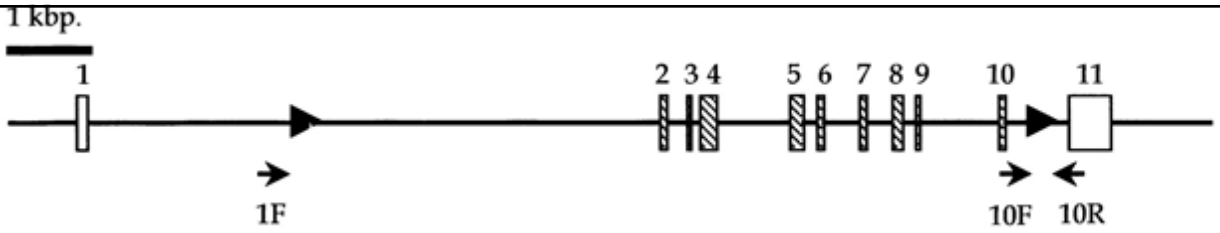

Figure 1.3.3: Schematic representation of structure of p53 floxed allele
Floxed p53 located between intron 1 and 10, on cre activation, conditional p53 deletion occurs [76]

1.3.4 Cdkn2a and Rb

Cdkn2a, also known as $p16^{Cdkn2a,}$ is a cell cycle inhibitor that bears a striking resemblance with the tumor suppressor gene, p53. It has also proven to be an important cell growth regulator. This gene has been found to be somatically mutated in several cancer types [77-79]. Cdkn2a usually blocks abnormal cell growth and proliferation by inhibiting the kinase activity of the enzymes and arrests the cell cycle at the G1 phase. However, in the case of mutant p16, the progression of abnormal cell division is not inhibited, leading to aberrant cell growth [80, 81].

The retinoblastoma (Rb) pathway comprises p16INK4A and p21CIP1. Rb is a downstream gene product of the Cdkn2a cell cycle regulation pathway, as shown in Figure 1.3.4a. It is involved in the regulation of the cell cycle for tumor suppression. The Rb pathway inhibits the kinase activity of cyclin-cyclin dependent (CDK) complexes. In normal conditions, these complexes inactivate Rb protein and two other family members of Rb, p107 and p130, by hyperphosphorylation during G1/S to G2/M transition phase in the cell cycle [82], as shown in Figure 1.3.4c.

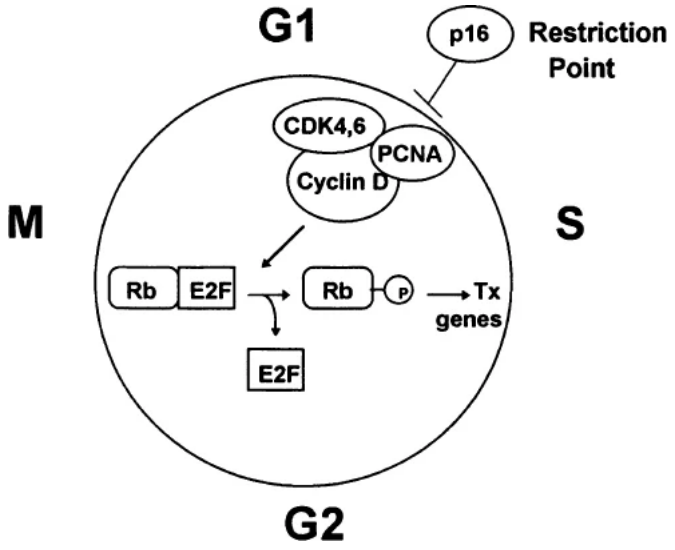

Figure 1.3.4a Schematic representation of the cell cycle pathway regulated by Cdkn2a/Rb genes
The diagram shows p16 as an early check-point and Rb as a downstream regulator which inhibits the abnormal cell growth [80]

Although in GWAS studies, few EAC patients show deletion of the Cdkn2a gene, which is upstream of Rb [24, 64]. It is crucial to study the regulation of Rb protein in EAC since it directly interacts with E2F protein complexes involved in tumorigenesis [80, 83].

Since the Rb gene has been more widely studied in lung cancer than in EAC, a conditional knock-out cre-lox mouse model for lung adenocarcinoma has been generated to study the Rb1tm3Tyj gene. Rb gene is located on exon 3 in chromosome 13. Once the cre mediated recombination occurs, the Rb gene gets inactivated [84], as shown in Figure 1.3.4b.

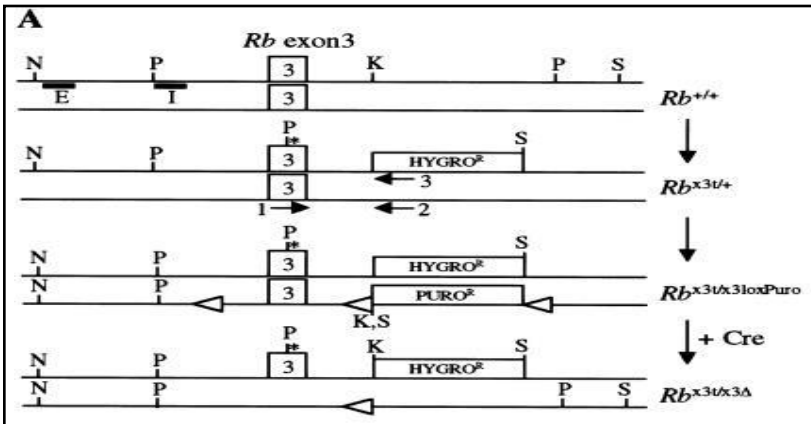

Figure 1.3.4b: Schematic representation of Rb locus at exon 3 in transgenic mice
Rb alleles located on exon 3, upon introduction of Cre, Rb exon 3 gets deleted hence inactivating Rb functionality [85]

The diagram below depicts the cell cycle regulatory pathways mediated by p53 and Rb (Figure 1.3.4c).

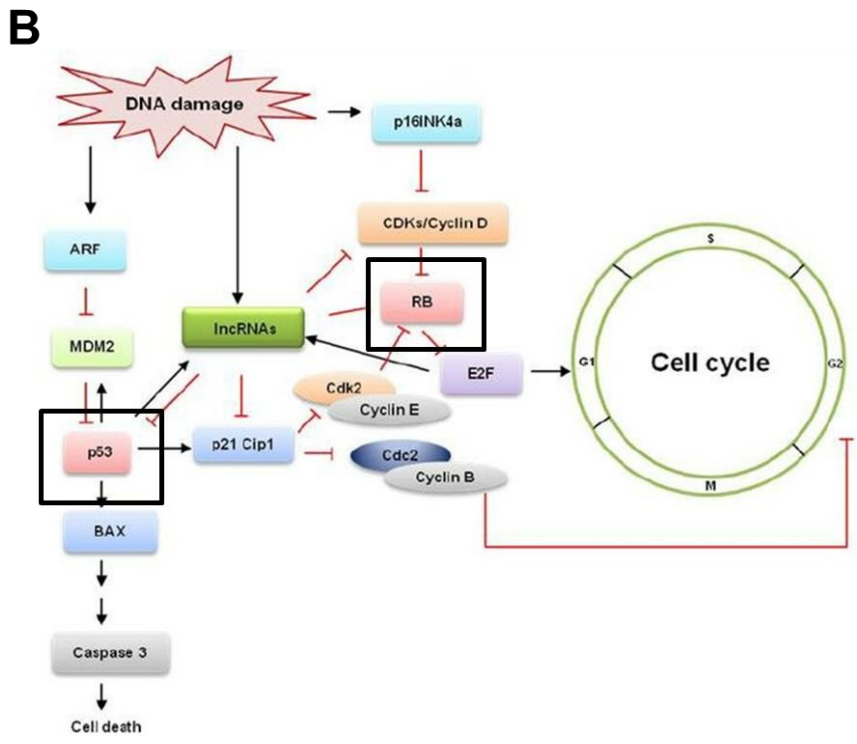

Figure 1.3.4c Diagrammatic representation of cell cycle regulation and the role of p53 and Rb as cell cycle regulators: Shows detailed pathway illustration of cell cycle triggered by DNA damage and the role of p53 and Rb in its regulation.

1.4 Diagnosis and Therapy

The diagnosis of EAC is dependent on endoscopic surveillance and histological evaluations. The patient undergoes biopsy collection from the suspected region, which is evaluated histologically based on the TNM classification and then an appropriate therapy or treatment is prescribed. However, continuous surveillance programs are tedious and time-consuming for patients as well as medical personnel. This process can be made simpler by identifying different biomarkers and adequate genomic knowledge of EAC so that it becomes easy to diagnose the disease and helps to identify non-dysplastic patients that have a chance to develop EAC.

There have been a few options in the field of treatment and therapies for EAC, such as proton pump inhibitors, which are widely used to normalize the esophageal pH. This method is helpful to lower cell proliferation and promote cell differentiation, which could reduce progression. Regardless of the extensive use of these inhibitor pumps, the incidence of BE and EAC is still rising [8].

With the rising advancement of Next-Generation Sequencing, there has been some development in predicting different biomarkers and translating this knowledge into clinical practices. Apart from these genetic biomarkers, another non-endoscopic technology has become evident known as cytosponge. Cytosponge is a capsule which the patient ingests. After 5 mins, it releases the sponge and is then retrieved with the cytological specimen from the patient's esophageal mucosa. This specimen is analysed with staining for trefoil factor 3, which is a diagnostic marker for Barrett's. Cytosponge is a promising upcoming technique with a sensitivity of 73.3% and a specificity of 93.8% [86, 87].

Furthermore, different drug therapies are either being used to treat a specific group of EAC patients or are under trial. Cisplatin, 5-Fluorouracil and epirubicin are to name a few [88].

Chapter 2: Material and Methods

All animal experiments were conducted in accordance with the Federation of European Laboratory Animal Science Association (FELASA) under the approval of the district government of Upper Bavaria (Regierung von Oberbayern). The license numbers were *ROB-55.2-2532.Vet_02-15-29* and *ROB 55.2-2532.Vet_02-20-69.*

All animal procedures were approved by the Institutional Animal Care and Use Committee at the Technical University Munich.

2.1 Mouse Lines and Husbandry

All the mice were backcrossed to a C57BL/6 background and were intercrossed to obtain the required genetic combinations. The following genes were used to generate the required mouse lines:

L2-IL-1beta, Vim-Cre^{TM}, p65, Lgr5-EGFP-ires-CreERT/2, KRas G12D, TP53, Rb

Table 2.1 List of different mouse lines

Genotype	**Abbreviation**
Vim-Cre^{TM}	
L2-IL-1beta.Vim-Cre^{TM}.p65	IL-1b.Vim-Cre^{TM}.p65$^{fl/fl}$
Lgr5-EGFP-ires-CreERT/2	
L2-IL-1beta.Lgr5-EGFP-ires-CreERT/2	L2-L/L2-IL-1b
L2-IL-1beta.Lgr5-EGFP-ires-CreERT/2. KRastm4Tyj	L2-LK
L2-IL-1beta.Lgr5-EGFP-ires-CreERT/2.Trp53tm1Brn	L2-LP
L2-IL-1beta.Lgr5-EGFP-ires-CreERT/2.Rb1tm3Tyj	L2-LR
L2-IL-1beta.Lgr5-EGFP-ires-CreERT/2.KRastm4Tyj.Trp53tm1Brn	L2-LKP
L2-IL-1beta.Lgr5-EGFP-ires-CreERT/2.KRastm4Tyj. Rb1tm3Tyj	L2-LKR
L2-IL-1beta.Lgr5-EGFP-ires-CreERT/2.Trp53tm1Brn.Rb1tm3Tyj	L2-LPR
L2-IL-1beta.Lgr5-EGFP-ires-CreERT/2.KRastm4Tyj.Trp53tm1Brn.Rb1tm3Tyj	L2-LKPR

All mice were bred under specific pathogen free (SPF) conditions in the animal facility of Klinikum rechts der Isar of Technische Universität München. The mice were housed Sealsafe NEXT Blue line cages (1145T, Scanbur). A maximum group of six mice were housed in the stock cages and in the breeding cages maximum of two females were housed with one male in a cage. The cages were maintained at a temperature of 20-25 ºC, 50-60% humidity along with a 12-hour light-dark cycle. All the animals were fed with the standard chow diet (ssniff, Spezialdiäten GmbH, Soest, Germany) and water *ad libitum*.

2.2 Determining Genes of Interest

2.2.1 DNA Extraction

The pups in the breeding cages were weaned at the age of 3-4 weeks. Every new pup was given a unique number by ear marking, i.e, punching the ear to collect the piece of tissue. These tissue samples were used for extracting DNA. The samples were lysed with lysis buffer containing 200 µl DirectPCR-Tail Lysis Reagent (31-102-T, Peqlab) and 2 µl Proteinase K (03115828001, Roche Diagnostics) at 55 ºC and 500 rpm overnight. The lysis was inactivated by heating the samples at 85 ºC for 60 mins. These lysed samples were used as the DNA template for detecting the genes of interest using Polymerase Chain Reaction (PCR).

2.2.2 Genotyping PCR

For each PCR reaction a total volume of 10 µl was prepared. This reaction volume constituted of 5 µl of ReadyMixTM REDTaq® PCR Reaction Mix with $MgCl_2$ (R2648, Sigma), 1mM of each primer (forward and reverse; Sigma, Germany), 1 µl of lysed sample as template and the volume was filledup with DNase-RNase free water.

In general, a PCR reaction runs for 35-40 cycles. It consists of denaturation (95, 3mins), annealing (primer specific) and elongation (72, 30 secs). DNA amplification was carried out on Thermal Cycler (T100, BioRad, California) with the following conditions tabulated in Table 2.2.2:

Table 2.2.2: Description of PCR reactions for each gene				
Gene Target	**Primer Sequence**	**Annealing Temperature**	**Elongation Time**	**Band Size**
L2-IL1beta	5´- CTT CCT GTT CCA TTC AGA GAC GAT - 3´ 5´-CTC CAG CTG TAG AGT GGG CTT ATC - 3´	57°C	30sec	277bp
Vim-Cre™	5´- CCT GGA AAA TGC TTC TGT CCG - 3´ 5´- CAG GGT GTT ATA AGC AAT CCC - 3´	55°C	30sec	392bp
p65	5´- GAG CGC ATG CCT AGC ACC AG - 3´ 5´- GTG CAC TGC ATG CGT GCA G - 3´	58°C	30sec	WT 264bp Mut 300bp
Lgr5-CreERT	5´- ATA CCC CAT CCC TTT TGA GC - 3´ 5´- CTG CTC TCT GCT CCC AGT CT - 3´ 5´- AA CTT CAG GGT CAG CTT GC - 3´	57°C	30sec	WT 298bp Mut 174bp
KRasG12D	5´- CAC CAG CTT CGG CTT CCT ATT - 3´ 5´- AGC TAA TGG CTC TCA AAG GAA TGT A - 3´ 5´- CCA TGG CTT GAG TAA GTC TGC - 3´	57°C	30sec	WT 273bp Mut 180bp
p53	5´- CAC AAA AAC AGG TTA AAC CCA - 3´ 5´- AGC ACA TAG GAG GCA GAG AC - 3´	58°C	30sec	WT 288bp Mut 350bp
Rb	5´- CTC TAG ATC CTC TCA TTC TTC - 3´ 5´- CCT TGA CCA TAG CCC AGC AC - 3´	57°C	30sec	WT 258bp Mut 308bp

2.2.3 Agarose Gel Electrophoresis

A 2.5% agarose gel containing Roti®GelStain (Carl Roth, Germany) was used to visualize the PCR products. Roti®GelStain is a less toxic substitute of ethidium bromide which functions on a similar principle of intercalating with DNA and is visible under LED or UV light. Once the gels were prepared in 1X TAE buffer containing 0.005% Roti®GelStain. 10 µl of each sample was loaded along with 5 µl of 100kb DNA ladder (N0467L, BioLabs) as a control to monitor the band size. Gels were run at a constant voltage of 120-150V depending on the size of the gel for 2-3 hrs. In order to visualize the band size, gels were photographed with a GelDocTM XR system (BioRad) using the Quantity One software (BioRad). Images were saved as TIFF and evaluated manually.

2.3 Induction of Mice

All the mice were induced with tamoxifen food (GENOdiet CreActive T400, Radiated, Genobios Sarl, Laval, France) at the age of 4 months for 3 weeks which was followed by standard chow diet. Tamoxifen food cycle was repeated every second month for two weeks.

2.4 Evaluation of Mice and Necropsy

2.4.1 Health report and evaluation

All the mice were examined physically and weighed at least once a week. Each mouse was scored once in a week and the observations were recorded in the score sheet as approved by the Govt. of Upper Bavaria.

2.4.2 End-of-Experiment

The end-point of an experiment was mostly at the age of 6, 7 and 12 months or prior if there was any noticeable sign of illness (hunched back, erected fur, papilloma or abscess). The mice were euthanized by inhalation of, Isofluran CP® (CP-Pharma, Germany). The animal was exposed to isofluan in a closed chamber till there were no sign of breathing after which they were taken out from the chamber and verified for death.

Once it was confirmed that the animal was dead, immediately blood was drawn from the heart using 20-gauge needle in a 2ml syringe. The blood was collected in a microvette (500 z-Gel, Sarstedt, Germany) and stored at room temperature. Once the organ collection was complete, blood was centrifuged for 5 minutes at 10,000g. Serum was separated from plasma. The serum was collected in a separate microfuge tube and snap frozen in liquid nitrogen and stored at -80ºC until further use.

Once all the organ sampling was completed, the organs were thoroughly washed in PBS. Two separate pieces of tissue each was collected from liver, spleen, esophagus, small intestine and colon. Stomach tissue was divided in three parts – forestomach, cardia and rest of stomach. One piece of tissue from these organs was snap frozen in liquid nitrogen and the other piece was stored in RNA Stabilization Buffer (Qiagen, Germany) and stored at 4ºC overnight and was moved to -80ºC the next day until further use. Two pieces of the tail was also cut and stored in -20ºC for regenotyping.

2.4.3 Macroscopic Scoring

2.4.3.a Imaging

Once the mice were sacrificed. All the organs were collected and washed thoroughly in PBS. The stomach was cut open along the longer curvature and the esophagus was opened in the direction

from distal SCJ to proximal upper esophagus. The organ was rinsed with PBS from inside. Then it was placed flat on the Whatman paper and macroscopic images were taken using a camera.

2.4.3.b Scoring

In order to score the phenotype of the mice macroscopically, a scoring system was established taking two factors into account. First, tumor extent and second, tumor size. Both these entities were scored separately and an average of both the scores was calculated to obtain the final score. The scoring scheme for the same has been shown below in Figure 2.4.3b.

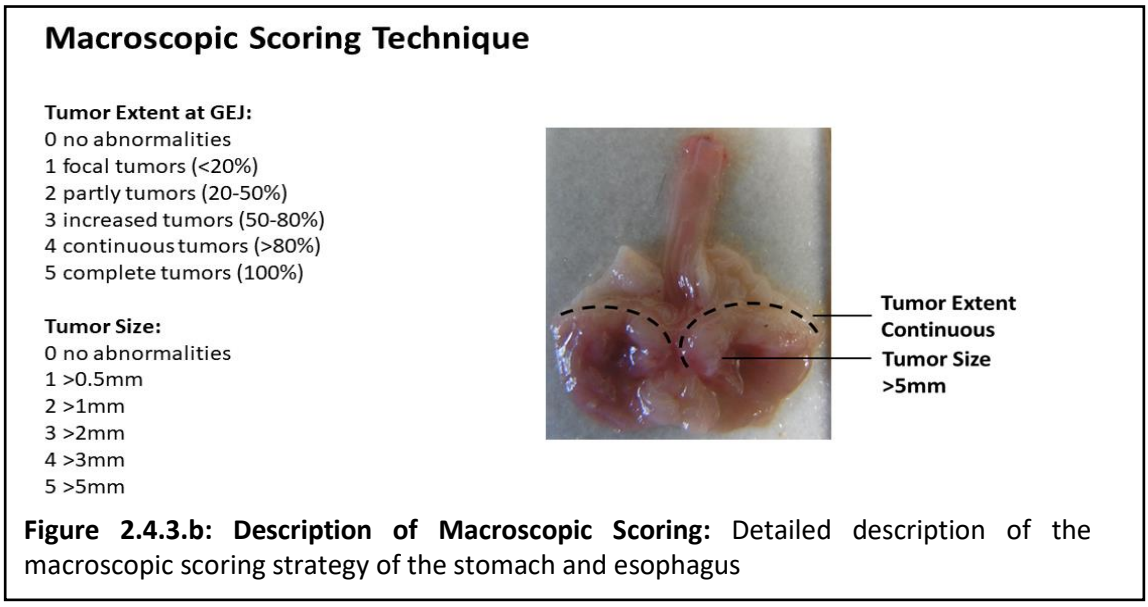

Figure 2.4.3.b: Description of Macroscopic Scoring: Detailed description of the macroscopic scoring strategy of the stomach and esophagus

2.5 Histological Analysis

2.5.1 Preparation of PFPE-Tissue samples

After the mice were euthanized and the tissue samples were collected as described in Section 2.4.2., the remaining tissue from the organs liver, spleen, pancreas, kidney, lungs, small intestine, colon and stomach was placed in histocassettes (7-0014, neoLab). These cassettes were stored in 4% paraformaldehyde solution prepared in PBS for fixation. After an overnight incubation in PFA, the tissue cassettes were dehydrated in increasing concentration of ethanol, xylene and paraffin. This process of dehydration was carried out in a Leica S300 tissue-processing unit. The next day, the PFA-fixed tissue samples were embedded in liquid paraffin and were allowed to cool down and harden. These blocks were stored at room temperature.

2.5.1a Tissue Sectioning

The PFPE tissue blocks were pre-cooled at -20ºC overnight. The next day the blocks were cut into 2.5µm thick sections on microtome (Thermo Scientific, Microm HM 355S, USA). The sections were immediately transferred in a water bath heated to a temperature of 50ºC to stretch and flatten the tissue. After few minutes they were collected on Superfrost Ultra (Thermo Scientific) slides and were allowed to dry overnight. The slides were incubated in oven at 60ºC for 60 minutes to ensure that the sections attach to the slide.

2.5.1b Hematoxylin and Eosin Staining

Hematoxylin and Eosin staining was performed to view the histology of the cellular structure of the tissue. The paraffin sections were deparaffinized in Xylene twice for 20 mins each. Followed by a descending order of alcohols (Isopropanol, 96%, 70%) for 2 mins each to rehydrate the sections. After the sections were incubated in distilled water for 5 mins, they were stained with Meyer's hemalaun (1.09249.2500; Merck) for 3 minutes to stain the nuclei violet. After the slides were washed off under running tap water for 10 mins to get rid of excess hemalaun, they were counterstained with Eosin (1.7% ethanolische Eosinlösung, Apotheke Klinikum rechts der Isar, diluted 1:5 in 96% ethanol) for 3.5 minutes to stain acidic structures including the extracellular matrix and cytoplasm in pink. The sections were dehydrated in ascending order of alcohols (96%, Isopropanol) and twice for 2 minutes each in Xylene. The slides were then mounted with VectaMount (H-5000, Vector Laboratories). Slides were scanned at 20X magnification on Leica Scanner in the Core Facility at the Department of Pathology, Klinikum rechts der Isar.

Table 2.5: Rehydration and Dehydration of paraffin sections for staining *All the paraffin slides were passed through the rehydration and dehydration steps.*			
Rehydration Steps (Pre-Staining)		**Dehydration Steps (Post-Staining)**	
Solution	**Incubation Time (mins)**	**Solution**	**Incubation Time (mins)**
Xylene I	15	**70% Ethanol I**	15
Xylene II	15	**70% Ethanol II**	15
Isopropanol I	2	**96% Ethanol I**	2
Isopropanol II	2	**96% Ethanol II**	2
96% Ethanol I	2	**Isopropanol I**	2
96% Ethanol II	2	**Isopropanol II**	2
70% Ethanol I	2	**Xylene I**	2
70% Ethanol II	2	**Xylene II**	2

2.5.1c Alcian Blue-Periodic Acid Schiff (Alcian Blue-PAS) Staining

Alcian blue-PAS is a pan mucin combination to differentiate between acidic and basic mucus producing cells respectively. The slides were subjected to deparaffinization, and rehydration of the tissue as indicated in Table 2.5. After incubation in distilled water the slides were stained with alcian blue for 15-20 secs. Followed by another wash with running tap water for 3 mins. This stained the acidic mucus-producing cells blue. Then the slides were incubated in Periodic acid for 5 - 10 mins followed by another wash with distilled water for 3 mins. To complete the PAS reaction the slides were incubated in Schiff's reagent for 15 mins and washed again to counterstain with hematoxylin for 30 secs. After washing of the excessive counterstain under tap water the slides were dehydrated according to Table 2.5 and mounted.

2.5.1d Immunohistochemistry (IHC)

Immunohistochemistry was used as a tool to detect the expression of particular antigen proteins using antibodies. This staining was performed on paraffin slides. The slides were deparaffinized and rehydrated according to Table 2.5. Antigen unmasking was performed in antigen retrieval solution (Citrate buffer or EDTA buffer) using microwave for 5 mins at 900 W, 5 mins at 90 W and 10 mins at

360 W. The slides were cooled down at room temperature (RT) for at least 30 mins. After the slides were cooled, they were briefly washed in PBS. The section on the slides were encircled using a ImmunoEdge Pen and transferred to wet chamber. This was followed by endogenous peroxidase blocking with 3% H_2O_2 for 10 mins. In order to block unspecific binding sites, the sections were incubated with blocking solution prepared in 3% BSA with 5% Goat serum with Streptavidin for 30 – 60 mins. After blocking, the sections were incubated with primary antibody as described in Table 2.5.4 along with Biotin. The sections were washed 3X with TBST (Tris Buffer saline - 0.1% Tween 20) or PBST (Phosphate Buffer saline - 0.1% Tween 20) for 5 mins each. A biotinylated secondary antibody solution was prepared, and the sections were incubated in it for 30 mins. During the incubation with secondary antibody, ABC solution was prepared (Vectastain ABC kit, Vector Labs, PK-6100). ABC was prepared fresh every time 30 mins prior to incubation at RT. After washing off the sections with a suitable wash buffer, the slides were incubated in ABC solution for 30 mins. In case of double staining for the second primary antibody ABC-AP solution kit (Vector Labs, AK-5000) was used instead of ABC. This was followed by the final step of colour development with DAB solution. The DAB solution was freshly prepared using the DAB Peroxidase Substrate Kit (Vector Labs, SK-4100) and the sections were incubated with it for approximately 30 sec – 5 mins at RT, depending on the protein expression. The sections were rinsed and counterstained with hematoxylin for 30 sec followed by washing, dehydration and mounting.

p53 and p21 stainings were performed in autostainer (Bond RXm, Leica) in the Core facility at the department of Pathology, Klinikum rechts der Isar.

Table 2.5.1d: Primary antibodies and conditions for IHC

Antibody	Manufacturer	Antigen Retrieval Buffer	Dilution	Primary Incubation Conditions
Ki67	Abcam (ab15580)	Citrate Buffer	1:1000	4ºC Overnight
α-SMA	Abcam (ab5694)	Citrate Buffer	1:400	2hrs, RT
y-H_2AX	Cell Signalling (9718)	Citrate Buffer	1:750	4ºC Overnight
Vimentin	Abcam (ab92547)	Citrate Buffer	1:1000	2hrs, RT
p-IKαβ	Cell Signalling (2697P)	Citrate Buffer	1:50	4ºC Overnight
p53	Leica (NCL-L-p53-CM5p)	EDTA Buffer	1:150	4ºC Overnight
p21	Abcam (ab107099)	EDTA Buffer	1:350	4ºC Overnight

2.5.2 Quantification of Stainings

Histopathological evaluation of Hematoxylin and Eosin staining as described in Section 2.5.2 was carried out blindly by a pathologist or an experienced gastroenterologist. The scoring criteria followed for the evaluation was as below.

Inflammation Score	Metaplasia Score
0 no inflammation	0 no metaplasia
1 mild inflammation	1 rare mucus cells
2 moderate inflammation	2 single metaplastic glands
3 severe inflammation	3 multiple metaplastic glands

Dysplasia Score	Carcinoma Grade
0 no dysplasia	G1sm1 well differentiated carcinoma but very focal
1 superficial epithelial atypia	G1T1 HGD with transition to well differentiated carcinoma
2 atypia in granular complexity	G1T2 well differentiated carcinoma
3 low-grade dysplasia	G2T3 moderately differentiated carcinoma
4 high-grade dysplasia	G3T3 poorly differentiated carcinoma
5 carcinoma	

For Alcian Blue-PAS and stainings from immunohistochemistry quantification was done using ImageJ in which % positive region or % positive cells was calculated in 3-4 regions of the stomach and esophagus per mouse. The cohorts for these stainings included 5-8 mice per genotype.

2.5.3 TUNEL Assay

TUNEL assay was performed to detect apoptosis or cell death in tissue. The assay was used to label cleaved DNA fragments with dUTP which was imaged through fluorescent microscopy. PFPE slides were used for this assay. The slides were deparaffinized and rehydrated according to Table 2.5.2. Antigen unmasking was done for 20 mins with antigen retrieval buffer (10mM Tris base + 0.05% Tween-20 adjusted to pH 9). The slides were cooled down overnight at RT. After a brief wash with PBS, the slides were incubated with blocking buffer (0.1M Tris-HCl, pH7.5 + 3%BSA + 20%FBS) for 30 mins. The slides were rinsed 3X with PBS for 5 mins each. In situ Cell Death Detection Fluorescein

kit (Roche, Germany) was used to prepare the TUNEL reaction. The TUNEL mix was prepared with enzyme and the label mix in a ratio of 1:9. The slides were incubated with 50 µl TUNEL mix on each slide and were incubated at 37ºC for 60 mins in dark. After washing the slides with PBS, they were mounted with mounting media containingDAPI (Vector Labs, Germany) and the sections were viewed under fluorescent microscope (1016-758, Zeiss). Quantification was carried out by calculating % positive cells in 4-5 field of views.

2.6 Flow Cytometry

Flow cytometry was used for immune cell profiling in which the stomach and the esophagus tissue was evaluated for the presence of different immune cell populations in different genotypes.

2.6.1 Preparation of Buffers

All the buffers and the antibodies except Krebs Ringer buffer were prepared fresh on the day of the sample preparation.

Table 2.6.1a: Composition of Buffers		
Krebs Ringer Buffer (Prepared in distilled water)	118 mM	NaCl
	24.8 mM	$NaHCO_3$ (S5761, Sigma)
	1.2 mM	KH_2PO_4 (P5379, Sigma)
	4.8 mM	KCl (P4504, Sigma)
	1.25 mM	$CaCl_2$
	1.2 mM	$MgSO_4$ (208094, Sigma)
	10 mM	HEPES (9105.3, Roth)
Digestion buffer esophagus	5 ml	Krebs Ringer Buffer (see Above)
	4% (w/v)	BSA (A2153, Sigma)
	2 mg/ml	Collagenase P (11213873001, Roche)
Digestion buffer cardia and rest of stomach	5 ml	RPMI (11875-093, Invitrogen)
	2 mg/ml	Collagenase P (11213873001, Roche)
	2 mg/ml	Pronase (10165921001, Roche)
FACS buffer	1X	PBS (14190094, Invitrogen)
	2%	FBS (10500064, Invitrogen)
	2 mM	EDTA (AM9260G, Invitrogen)

Table 2.6.1b: Surface marker panel for immune cell stainings All the antibody cocktails were prepared in FACs Buffer	
Myeloid Staining	Anti-mouse CD45 eFluor450 (48-0451-82, eBioscience)
	Anti-mouse CD11b APC-eFluor 780 (47-0112-82, eBioscience)
	Anti-mouse F4/80 (14-4801-81, eBioscience)
	Anti-mouse Ly-6G Alexa Flour700 (56-5931-82, eBioscience)
	Anti-mouse CD11c FITC (11011481, eBioscience)
	Anti-mouse Ly-6C PE (12-5932-82, eBioscience)
T-Cell Staining	Anti-mouse CD4 e450 (48004180, eBioscience)
	Anti-mouse CD8a APC (17-0081-82, eBioscience)
	Anti-mouse CD3 FITC (11003381, eBioscience)
	Anti-mouse NK1.1 APC-eFluor780 (47-5941-82, eBioscience)
	Anti-mouse γδTCR PE (12-5711-82, eBioscience)
	Anti-mouse CD69-Alexa Fluor700 (104539, BioLegend)
	Anti-mouse CD25 PE Cy7 (25-0251-82, eBioscience)
	Anti-mouse CD45 PerCP Cy5 (45-0451-82, eBioscience)

2.6.2 Preparation of Tissue

Mice were sacrificed with inhalation of Isofluran. Approximately 1ml of blood was retrieved from the heart and added to 5 ml red blood cell lysis buffer (Sigma. Germany). This was stored at RT till further processing. Spleen, esophagus and stomach was resected from the mouse and the organs were quickly rinsed in PBS. Spleen was stored in 5 ml PBS till further processing. Esophagus, cardia and rest of stomach was separated and washed thoroughly in PBS. These organs were transferred separately in 6cm petri dishes containing 1 ml of 0.5M EDTA (Invitrogen. Germany). These organs were then disintegrated into small pieces using a fine-tip scissor. Tissue pieces from esophagus was added in 5 ml Krebs Ringer buffer (as shown in Table 2.6.1a). Tissue pieces from cardia and rest of stomach were added in their organ specific buffer (as indicated in Table 2.6.1a) in separate tubes. The tubes with esophagus, cardia and rest of stomach tissue were incubated in a shaker at 150 rpm at 37ºC for 40 mins. Meanwhile, the spleen was mashed using a plunger and passed through 40 µm cell strainer (Corning, USA). The strained cells were collected in 5 ml red blood cell lysis buffer and incubated at RT for 10 mins. The blood and the spleen samples were centrifuged at 400-500g for 10 mins at 4ºC. Supernatant was discarded and the pellet was lysed again with 1 ml red blood cell lysis

buffer. Once the esophagus, cardia and rest of the stomach tissues were digested, they were also passed through 40 µm strainer using a plunger and were centrifuged at 400-500g for 10 mins at 4ºC. After the supernatant was discarded, the pellets for all the organs were suspended in FACs buffer (see Table 2.6.1a) and transferred to a plate. The plate was centrifuged at 400-500g for 10 mins at 4ºC. All the antibodies (see Table 2.6.1b) were diluted in a dilution of 1:100. After washing with FACs buffer, the cells were stained for surface markers by incubating the plate for 30 mins in dark on ice. 150 µl of FACs buffer was added in each well and the plate was again centrifuged at 400-500g for 10 mins at 4ºC for washing. After the pellet was retrieved, 150 µl of FACs buffer was added and the samples were transferred to FACs tubes. 5 µl of live-dead cell marker was added to each sample before they were measured on the Flow Cytometer (Gallios, Beckmann Coulter).

2.7 Cell Culture

All the cell culture work was done under specified primary or secondary conditions. All the cultures were maintained at 37ºC in Herasafe Class II biological safety cabinet (ThermoFisher) under an atmosphere of 5% CO_2.

2.7.1 Culture of Cell Lines

The human esophageal cancer cell lines used were OE19 and OE33. These cell lines were purchased from the European Collection of Animal Cell Cultures (ECACC; OE19 – 96071721; OE33 – 96070808). The cells were cultured in Roswell Park Memorial Institute (RPMI) 1640 media (11875-093, Invitrogen) along with 10% FBS (Fetal Bovine Serum, 10500064, Invitrogen) and 1% P/S (Penicillin/Streptomycin, 15140122, Invitrogen) in a 10-cm cell culture dish (83.3902, Sarstedt).

The human fibroblast cell line known as FEF (Fetal Embryonic Fibroblast) cells were cultured in Dulbecco's Modified Eagle Medium (DMEM) media along with 10% FBS and 1% P/S in a 10-cm culture dish.

To maintain the cell lines, the cells were grown to be 80% confluent. They were then trypsinized with 0.25% Trypsin-EDTA (25200056, Invitrogen). The cells were collected and centrifuged at 300-500g for 5 mins. The supernatant was discarded, the cell pellet was resuspended in the media, plated in a flask or culture dish and incubated at 37ºC.

2.7.2 L-WRN Media Production

Conditioned media produced from the L-WRN cells served as the basal media for the 3D organoid cultures. These cells were transfected with R-spondin and noggin hence they secreted Wnt3A, R-spondin and noggin into the media. L-WRN cell line was cultured in DMEM (Dulbecco's Modified

Eagle Medium, 41965039, Invitrogen) with 10% FBS and 1% P/S. After 24 hours, the media was replaced with new media along with the addition of two selection markers G-418 (0.5mg/ml, 1:100,345812, Merck-Millipore) and Hygromycin B (H3274, Sigma). Once the cells were confluent, they were expanded in enough number of cell culture dishesand were allowed to become overconfluent for 3-4 days. To these overconfluent cells the primary media was added which consisted of Advanced DMEM-F12 (12634010, Invitrogen) + 20% FBS (10500064, Invitrogen) + 1% PenStrep (15140122, Invitrogen) + 1% HEPES (15630080, Invitrogen) + 1% Glutamax (35050038, Invitrogen). The petri dishes were incubated for 24 hours. This conditioned media was collected after every 24 hours for 4-5 days. The media was centrifuged to get remove dead cells and to prevent the filter from getting clogged. Once all the media was collected, it was passed through 0.2µm bottle-top sterile filter (595-4520, Invitrogen). An equal volume of primary media was added to this sterile filtered media to dilute it in 1:1 ratio. This lot of media was aliquoted and stored in -80ºC for long term use.

2.7.3 Cardia Organoid Culture

In order to isolate cardia organoids, the cardia region of stomach was resected from a euthanized mouse, the tissue was washed thoroughly in PBS and was cut into small pieces in 300µl of Accutase (A6964, Sigma) using fine-tip scissors. The tissue pieces were incubated in accutase for 15 mins at RT on a shaker. It was then transferred in to 20ml of another digestion buffer (see Table 2.7.3) on ice at 4ºC for 45 mins on the shaker. Once the digestion was complete, the workplace was moved to primary cell culture hood to maintain sterile conditions for the isolation. The tissue was allowed to settle down at the bottom of the tube. Supernatant was carefully removed. 10 ml of cold wash buffer (see Table 2.7.3) was added to the tissue sediment and was pipetted 8-10 times for mechanical shearing. This suspension was passed through 70 µm sterile filter. This step was repeated 3 times till the total volume of the filtered suspension reached 40 ml. The suspension was then centrifuged at 4ºC, at 400-500g for 10 mins. Once the pellet was formed, the supernatant was discarded. The pellet was resuspended according to 50 µl per well Matrigel™ (356235, BD Corning) and Matrigel™ drops were plated in 24-well plate. The drops were allowed to solidify. L-WRN media was prepared along with other growth factors (see Table 2.7.3). 500 µl per well media was added and the plate was incubated at 37ºC in the incubator at 5% CO_2. The media was replaced by new media every second day. Growth and the number of organoids was recorded by microscopy.

Table 2.7.3: Preparation of buffers and media for murine cardia organoid culture			
	Reagent /Growth Factor	**Final Concentration**	**Amount to be added**
For 20ml Digestion Buffer	PBS (14190094, Invitrogen)	1X	20ml
	EDTA (AM9260G, Invitrogen)	0.5M	100 µl
	EGTA (3054.2, Carl Roth)	0.5M	100 µl
For 500ml Wash Buffer	PBS (14190094, Invitrogen)	1X	500 ml
	FBS (10500064, Invitrogen)	10%	50 ml
	Penicillin/Streptamycin (15140122, Invitrogen)	1%	5 ml
For 40ml L-WRN media	N-2 Supplement (100x) (1750248, Invitrogen)	1X	400 µl
	B-27 Supplement (50x) (17504044, Invitrogen)	1X	800 µl
	n-acetyl-L-cysteine (A9165, Sigma)	1mM	100 µl
	Human EGF (AF-100-15, Peprotech)	50 ng/ml	5 µl

2.7.4 Human Organoid Culture

For culturing organoids from human patients, a freshly resected piece of tissue from the SCJ was obtained in PBS. The tissue was cut into fine pieces in Accutase. It was incubated at RT for 20 mins with sporadic shaking. After the incubation, 1ml of 2mM of EDTA in cold sterile PBS solution was added and the suspension was incubated on ice for 15 mins on a shaker. After the tissue was digested, the cell suspension was adjusted to a final volume of 10 ml using wash buffer (see Table 2.7.3). This was centrifuged for 7 mins at 500g at 4ºC. The supernatant was discarded, and the pellet was suspended in Matrigel™ and seeded in a 24-well plate with 50 µl drop per well. Once the Matrigel™ solidified, 500 µl of media (see Table 2.7.4) was added per well. The media was replaced every second day. Growth and the number of organoids was recorded by microscopy.

Table 2.7.4: Preparation of media for human organoid culture			
	Reagent /Growth Factor	**Final Concentration**	**Amount to be added**
For 40ml L-WRN media	N-2 Supplement (100x) (1750248, Invitrogen)	1X	400 µl
	B-27 Supplement (50x) (17504044, Invitrogen)	1X	800 µl
	n-acetyl-L-cysteine (A9165, Sigma)	1mM	100 µl
	Human EGF (AF-100-15, Peprotech)	50 ng/ml	5 µl
	Human FGF-10 (100-26, Peprotech)	100ng/ml	40 µl
	Nicotinamide (72340, Sigma)	10mM	200 µl
	SB431542 TGFb inhibitor (1614, TOCRIS)	10 µM	40 µl
	Y27632 ROCK inhibitor (1254, TOCRIS)	10 µM	400 µl
	SB202190 MAP kinase inhibitor (1264, TOCRIS)	5 µM	20 µl
	Anti-Anti (15240062, Thermo Fisher)	1X	400 µl

2.7.5 Passaging and Maintenance of Organoids

After 7-10 days, the organoids were passaged to keep them in culture. The splitting ratio was decided by viewing the presence of healthy organoids under the microscope and by checking the size of the pellet. The media was removed and 1ml of cold wash buffer (in case of murine organoids) or PBS (in case of human organoids) was added per well. The Matrigel™ was disrupted with mechanically by pipetting up and down several times. The solution was collected from all the wells and was collected in a centrifugation tube. This cell suspension was centrifuged at 4ºC for 10 mins at 300-500g. The supernatant was discarded carefully leaving behind the pellet and the Matrigel™. In order to remove Matrigel™ completely, along with the pellet it was resuspended in 500 µl of cell recovery solution (354253, Corning). This suspension was incubated on ice for a minimum of 30 mins. After which the volume was adjusted to 10 ml with cold PBS and the solution was pipetted several times and centrifuged at 4ºC for 5 mins at 300-500g. A clean pellet was obtained after discarding the supernatant. The pellet was resuspended in Matrigel™ and expanded according to a suitable splitting ratio.

2.7.6 Freezing and Thawing of Organoids

For freezing the organoids, the media was removed from the well. 1ml of cold wash buffer or PBS was added and the Matrigel™ was pipetted vigorously. The suspension was collected in a centrifugation tube at centrifuged at 4ºC for 10 mins at 300-500g. The supernatant was discarded along with the Matrigel™ so much so that the pellet was not disturbed. The pellet was then resuspended in 500 – 800 µl cell culture freezing media (12648010, Thermo Fisher Scientific) and the suspension was transferred into cryovials. The cryovials were stored in freezing container containing isopropanol filled with isopropanol and kept at -80ºC overnight and were transferred to liquid nitrogen the next day.

For thawing, the organoids were retrieved from liquid nitrogen and were warmed at 37ºC for few seconds. 1 ml of cold PBS was used to suspend the cells. This suspension was transferred to the microfuge or centrifugation tubes and was centrifuged at 4ºC for 5 mins at 300-500g. Supernatant was discarded, and the pellet was resuspended in Matrigel™ and plated. Once the Matrigel™ solidified, 500 µl media was added per well and the plates were incubated at 37ºC. Medium was replaced every second day.

2.7.7 Processing of Organoids

To perform further downstream applications on organoids, they were subjected to fixation and were embedded in paraffin. For fixing the organoids they were passaged and plated in 24 well plates on a glass coverslip (Ø12mm, LOT0783, ThermoScientific). On the day of fixation, media was removed and replaced with 500 µl PBS+ (see the recipe in Table 2.7.7a) per well twice, for 5 mins each. This was exchanged with 4% PFA in PBS+, 500 µl per well. The wells were stored at RT for 30 mins on a shaker. The fixation solution was discarded, and the wells were washed again with PBS+ twice for 5 mins each. The glass coverslip along with the Matrigel™ was transferred on cassettes and was run in the dehydration machine on the same day. In case the organoids were unable to be run in the dehydration machine on the same day, they were incubated with 0.1% PFA in PBS+ for maximum one week and then were dehydrated in the machine overnight.

Table 2.7.7a: Preparation of PBS+	
For 1 lt. 1X PBS	100mg $CaCl_2$ (Final conc. 0.9mM)
	470mg $MgCl_2$ (Final Conc. 0.493mM)
	Adjust pH to 7.4

For embedding the fixed and dehydrated organoids in paraffin, the steel mould was filled partly with paraffin. The organoids were scratched off from the glass coverslip using a scalpel into the paraffin. It was then cooled down and the blocks were stored at RT.

Paraffin-fixed organoid blocks were cut into 2 µm thick sections. Cutting was done at the Core Facility at the department of Pathology, Klinikum recht der Isar. PFPE organoid sections were stained for HE, Ki67 and y-H_2AX. The staining procedure wasfollowed as described in sections 2.5.2 and 2.5.4. The staining conditions were as shown in Table 2.5.4. For the histopathological evaluation of organoids, the HE staining was evaluated according to the scoring system as shown in Table 2.7.7b.

Table 2.7.7b: Histopathological Scoring of Organoids

Score	Description
0	Cuboidal cells, intermediate stage between squamous to columnar epithelium, nucleus located at the center of the cell
1	Columnar epithelium structure of the cells intact, elongated structure of cells, nuclei located towards the base of a cell
2	Columnar structure of the cells comparatively lost, apoptotic cells, non-aligned with spherical empty spaces positioned randomly within the epithelium
3	Columnar structure of the cells completely lost; clusters of undifferentiated cells observed

2.7.8 Isolation of Primary Fibroblasts

The esophagus was resected from the mouse to isolate fibroblast and was cut and washed in Hank's Balanced Salt Solution (14175053, Invitrogen) in a microfuge tube. The tissue pieces were allowed to sediment and the supernatant was decanted. Digestion buffer (See Table 2.7.8) was added to the tissue and was digested for 30 mins at RT on a shaker. The tube was centrifuged at 200g for 10 mins. Supernatant was discarded, the tissue was washed with wash buffer and centrifuged for 10 mins at 500g. After the supernatant was discarded, the pellet was resuspended in 2ml media (as described in Table 2.7.8) and plated in T25 flasks (TC Flask T25 Cell+, 83.3910.300). The basal media used was DMEM + 10%FBS + 1%P/S along with the growth factors as mentioned in the Table 2.7.8. The flask was incubated at 37ºC. The media was exchanged with new media the next day. Once the cells were confluent enough, they were trypsinized with 0.25% Trypsin-EDTA and expanded.

Table 2.7.8: Preparation of Buffers and Media for fibroblast isolation			
	Reagent/Growth Factor	**Final Conc.**	**Amount to be add**
For 6ml Digestion Buffer	Collagenase XI (C9407, Sigma)	0.375mg/ml	2.25mg
	Dispase II (D4693, Sigma)	0.1 mg/ml	0.6mg
For 50ml Wash Buffer	DMEM (41965039, Invitrogen)	50ml	49ml
	Sorbitol (6213.1, Carl Roth)	2%	1ml
For 40ml Basal Media	Insulin-Transferin-Selenium (41400045, ThermoFisher)	1X	400 µl
	Murine EGF (315-09, Peprotech)	50ng/µl	1 µl
	FGF-10 (100-26, Peprotech)	100 ng/µl	40 µl
	Gentamicin	5 µg/ml	4 µl

2.8 Molecular Techniques

2.8.1 DNA/RNA Isolation

2.8.1a Isolation of DNA/RNA from Tissue

To isolate DNA/RNA from tissues, the tissue samples were thawed at RT as they were stored in RNA Stabilization Buffer. Tissue was crushed in a microfuge tube placed in liquid nitrogen using a pestle. RLT lysis buffer supplemented with 1% β-Mercaptoethanol (M6250, Sigma) was added to the tube. The tissue was then homogenized for 30 – 90 secs. In case tissue particles were remaining, they were passed through the QIAShredder (79656, Qiagen). The tissue lysates were transferred to columns provided with AllPrep DNA/RNA kit (80224, Qiagen) and the protocol was followed as instructed by the manufacturer. DNA was eluted in 100 µl of elution buffer and RNA was eluted in 50 µl of RNase-Free water.

DNA isolation from tail tissues was done using DNeasy Blood and Tissue kit (69506, Qiagen). The protocol was strictly followed as instructed by the manufacturer. DNA was eluted in 200 µl of elution buffer.

2.8.1b Isolation of DNA/RNA from Cells and Organoids

Monolayer cells were trypsinized with 0.25% Trypsin-EDTA, the cells were centrifuged, and the pellet was obtained. The pellet was lysed with RLT buffer containing 1% β-Mercaptoethanol and AllPrep DNA/RNA kit (80224, Qiagen) was used for the isolation.

For the DNA/RNA isolation from organoids, they were obtained as a pellet by removing the Matrigel using cell recovery solution. Cell lysis was done with RLT buffer with 1% β-Mercaptoethanol. AllPrep DNA/RNA kit (80224, Qiagen) was used for the isolation. DNA was eluted in 100 µl of elution buffer and RNA was eluted in 50 µl of RNase-Free water.

Quantification of DNA and RNA was done using the NanoDrop Spectrophotometer (Thermo Scientific).

2.8.2 Protein Isolation

Protein was isolated from tissue by crushing the tissue pieces in liquid nitrogen using a pestle. 150-200 µl of lysis buffer was added to the crushed tissue and was homogenised. After the tissue was carefully broken down till no tissue remains were seen the lysate was sonicated for 5-6 secs. This lysate was incubated on ice for 15 mins followed by centrifugation at 4ºC for 15 mins at 12,000 rpm. The supernatant containing the protein was collected and stored at -80ºC.

In case of cells, they were washed briefly with PBS to get rid of unattached dead cells, lysis buffer was added directly to the well. The cells were scraped and collected in a microfuge tube, followed by incubation on ice and centrifugation. The supernatant was collected and stored.

For the organoids, the Matrigel was disrupted using the cold wash buffer (as mentioned in Table 2.7.8) or PBS, the organoids were collected in a tube and centrifuged at 4ºC for 10 mins at 500g. Supernatant was removed leaving behind pellet with the Matrigel. Depending on the pellet size 300 -500 µl of cell recovery solution was added and resuspended thoroughly. This suspension was incubated on ice for a minimum of 30 mins. 1ml PBS was added and the cells were centrifuged again at 4ºC for 5 mins at 400g. Supernatant was discarded, and the pellet was resuspended in the lysis buffer, followed by incubation on ice and centrifugation. The supernatant was collected and stored for downstream processing.

Table 2.8.2: Preparation of Protein lysis buffer

Reagent	**Stock Conc.**	**Final Conc.**
RIPA Buffer (Sigma, R0278)	1X	1X
Phosphatase Inhibitor (Roche, 04906837001	10X	1X
Protease Inhibitor (Sigma, 11836145001)	25X	1X

2.9 Treatment and Evaluation

2.9.1 In-vitro treatment

In-vitro treatments included treatment on cell lines and organoids as well as co-cultures with two cell types.

2.9.1a Treatment of Fibroblasts with IKK inhibitor

Primary fibroblasts were passaged 15-20 times before the treatment to get rid of the adherent epithelial cells. Fibroblasts were plated in 24-well plate. After 2 hours when the cells adhered to the bottom of the plate 5 µM of IKK inhibitor (BMS-345542, S8044, Selleckchem; Stock conc. 5mM) was added to the media. The cells were trypsinized and collected after10, 15, 30 and 60 mins for further downstream processing.

2.9.1b Co-culture of organoids and fibroblasts

Murine and human organoids were co-cultured with primary esophageal fibroblasts and FEF cells respectively. The co-culture was done in two settings, in the first part, organoids were plated in a 24-well plate and after 48 hrs fibroblasts/FEF cells were added in the media. In the second part, organoids were plated and after 48 hours IKK inhibited fibroblasts/FEF cells were added in the media. The co-culture lasted for 72 hours.

2.9.1c Evaluation

Cell lines: For cell lines, growth curve was evaluated through eyeballing.

Organoids: For organoids, growth curve was evaluated by counting the number of organoids in each well from day 1-5. In case of treatments or co-culture, the day of treatment or co-culture was day 0 and then the organoids were counted from day 1-5. For size curves, images of 15-20 organoids per well per condition were taken in a randomized manner. For final evaluation, area of the organoids was calculated using ImageJ.

2.10 Downstream Processing

2.10.1 Sequencing

2.10.1a PyroSequencing

Pyrosequencing was used to perform methylation analysis of the DNA. For this analysis 200 ng genomic DNA isolated from organoids and tissues as mentioned in section 2.8.1a. This DNA was

bisulphite-converted with the EZ DNA Methylation-Direct kit (Zymo Research, Irvine, USA) according to the manufacturer's instructions. Bisulphite-treated DNA was eluted in 15 µl of water. 2 µl was used for PCR amplification using PyroMark PCR kit (Qiagen). PCR products were pyrosequenced using PyroMark Q48 Advanced CpG reagents on a PyroMark Q48 Autoprep instrument (Qiagen). Pyrosequencing assays were designed using PyroMark Assay Design 2.0 software (Qiagen).

Following p16 methylation assay primers were used:

Table 2.10.1a: Primer sequences for p16Ink4a

Primer Name	**Sequence**
p16Ink4a-F	AGTAGTGTTTTTAGGGGTGT
p16Ink4a-R	(Btn)-CCATACTACTCCAAATAACTCTC
p16Ink4a-Seq	GGAAGGAGGGATTTATTG

*Btn, biotinylated.

For assay optimisation, methylated (100%), non-methylated (0%) and a scale of control samples with the following DNA methylation: 25%, 50% and 75% were used. The methylated control was prepared using the CpG methyltransferase enzyme (M.SssI; Thermo Scientific). The non-methylated control was prepared using the REPLI-g Mini kit (Qiagen). This protocol was performed by Dr. Krzysztof Flisikowski, AG Schnieke, TUM Weihenstephan.

2.10.1b Low-coverage Whole Genome Sequencing

Low coverage whole genome sequencing (LcWGS) and Amplicon sequencing were performed to examine the status of mutations and amplifications in tissue as well as organoids. Genomic DNA (gDNA) was isolated as mentioned in section 2.8.1a. NEBNext Ultra II Q5 Master Mix (New England Biolabs) was used to fragment gDNA. After end repair and A-tailing a TruSeq adapter was ligated, and fragments were finally amplified using barcoded primers with Illumina P5 and P7 overhangs according to the manufacturers protocol. The libraries were sequenced on a NextSeq 500 (Illumina) in a 75 cycles single end run. This protocol was performed and the results were analysed by AG Rad, Institute of Molecular Oncology and Functional Genomics, TUM.

2.10.2 Protein Analysis

Protein was isolated as described in section 2.8.2. Depending on the experiment, a particular technique was chosen for the evaluation.

2.10.2a Cytokine Profiling

For the detection of chemokines and cytokine levels, conditioned media and tissue lysates were used. Conditioned media was collected from co-culture of primary esophageal fibroblasts and epithelial cells werecollected at 24 hrs. Protein was isolated from esophagus, forestomach and cardia regions of the mouse as described in Table 2.8.2. Protein was quantified using Pierce BCA Protein Assay Kit (Thermo Fisher Scientific) following manufacturers protocol. For tissue lysates, protein was pooled to obtain a final amount of 200 µg, L2 (n=4) and L2-Vim-p65 (n=4). In case of co-culture conditioned media was pooled n=4 per condition. Proteome Profiler Array (R and D Systems, Mouse XL Cytokine Array Kit) was used to determine relative levels of chemokines and cytokines in the samples. The cytokine array was performed as described in the manufacturers protocol without any exceptions. Once the membrane was finally washed, it was exposed to X-Ray film for 1-2 mins. Presence of cytokines and chemokines were observed by overlapping the X-ray film with the template provided by the manufacturer as shown in Figure 2.10.2a. The intensity of the dots was measured using ImageJ to evaluate the results.

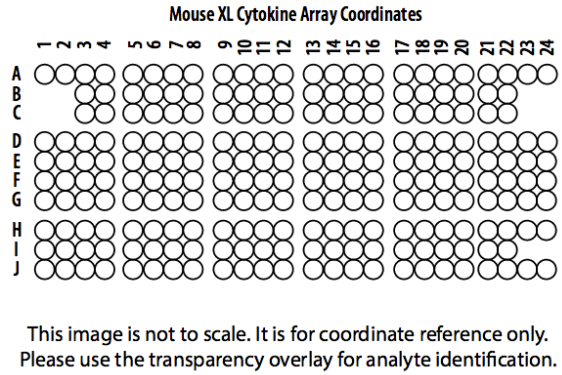

Figure 2.10.2a: Template overlay for the RD Systems Proteome Profiler Array.
Positive signals seen on developed film were identified by placing the transparency overlay template on the array image and aligning it with the pairs of reference spots in three corners of each array.

2.10.2b Western Blot

Western blot was performed to detect the expression of different proteins in treated and untreated cells, organoids and tissue samples. Protein was isolated as described in section 2.8.2. 20 µl of 1

µl/µg of protein was loaded per well along with the protein ladder. Once the samples were ran on a 10% SDS-PAGE gel, they were transferred on specific membranes (according to Table 2.10.2b). The membrane was blocked with a suitable blocking buffer and incubated overnight at 4ºC with primary antibodies (mentioned in Table 2.10.2b) in a dilution of 1:1000. The membrane was washed and incubated with HRP-conjugated anti-rabbit secondary antibody (GE Healthcare, NA934V) in a dilution of 1:2000 in the blocking buffer. The membrane was stripped when required with a stripping buffer (Thermo Scientific, 46430) for 15 mins and incubated with the second primary antibody. The bands were developed with enhanced chemiluminescence ECL system (GE Healthcare, GERPN2232) and visualized by BioRad Gel Documentation system.

Table 2.10.2b: Details and conditions of primary antibodies for western blot

Primary Antibody	**Membrane**	**Blocking Buffer**
Iκβα (Santa Cruz, SC-203)	0.45 µm PVDF (Merck-Millipore)	5% milk in TBST
β-Actin (Santa Cruz, 1:20,000)	0.45 µm PVDF /0.2 µm Nitrocellulose	5% milk in TBST

2.11 Statistical Analysis

All the statistical analysis was done using GraphPad Prism version 8. For two groups unpaired t-test was used and for more than two groups multiple comparison t-tests were used for significance tests.

Chapter 3: Results I

3.1 Cross-talk between epithelial and stromal cells in the inflammatory tumor microenvironment

Chronic inflammation forms the backbone of gastric tumor formation. In order to study BE initiation and tumor development, a novel BE mouse model has been established by Quante et al. [11]. This model demonstrated inflammation-based tumor initiation at 6 months of age, leading to tumor formation at 15 months. The model is based on the overexpression of the IL-1b gene in which the mice carried EBV-L2-IL-1b transgene, which overexpressed the human IL-1beta receptor in the basal epithelial cells in the squamous esophagus, leading to pL2-IL-1beta (L2-IL-1b) mice.

Stromal cells are an essential part of the tumor microenvironment. These cell types can form a desmoplastic stromal microenvironment that could contribute to cancer stemness and promotes angiogenesis around the tumor niche and proliferation of tumor cells.

In gastric carcinogenesis, it has been shown that with the increase of dysplasia, there is an increase in the a-SMA+ MFs, which contributes to the desmoplastic tumor microenvironment. However, the role of these MFs has not been studied in esophageal carcinogenesis. Hence, we do not know whether these cell types contribute to enhance inflammation in esophageal tumor microenvironment. To study the impact and the role of fibroblasts in the tumor microenvironment of L2-IL-1b mice during esophageal carcinogenesis, immunohistochemistry was performed for aSMA and Vimentin in order to identify activated MFs in the stromal microenvironment at different time-points (6, 9 and 12 months) and this was compared to the Wild-type mice. As seen in Figure 3.1.1. A (i) and (ii), a visible increase in the expression of both aSMA+ and Vimentin+ cells was observed with an increase in the age of mice. As statistically seen in Figure 3.1.1.B (i) and (ii), 9-months and 12-months old mice showed a significant increase in the positivity of the stromal cells around the epithelial cells when compared to wild-type mice at the SCJ.

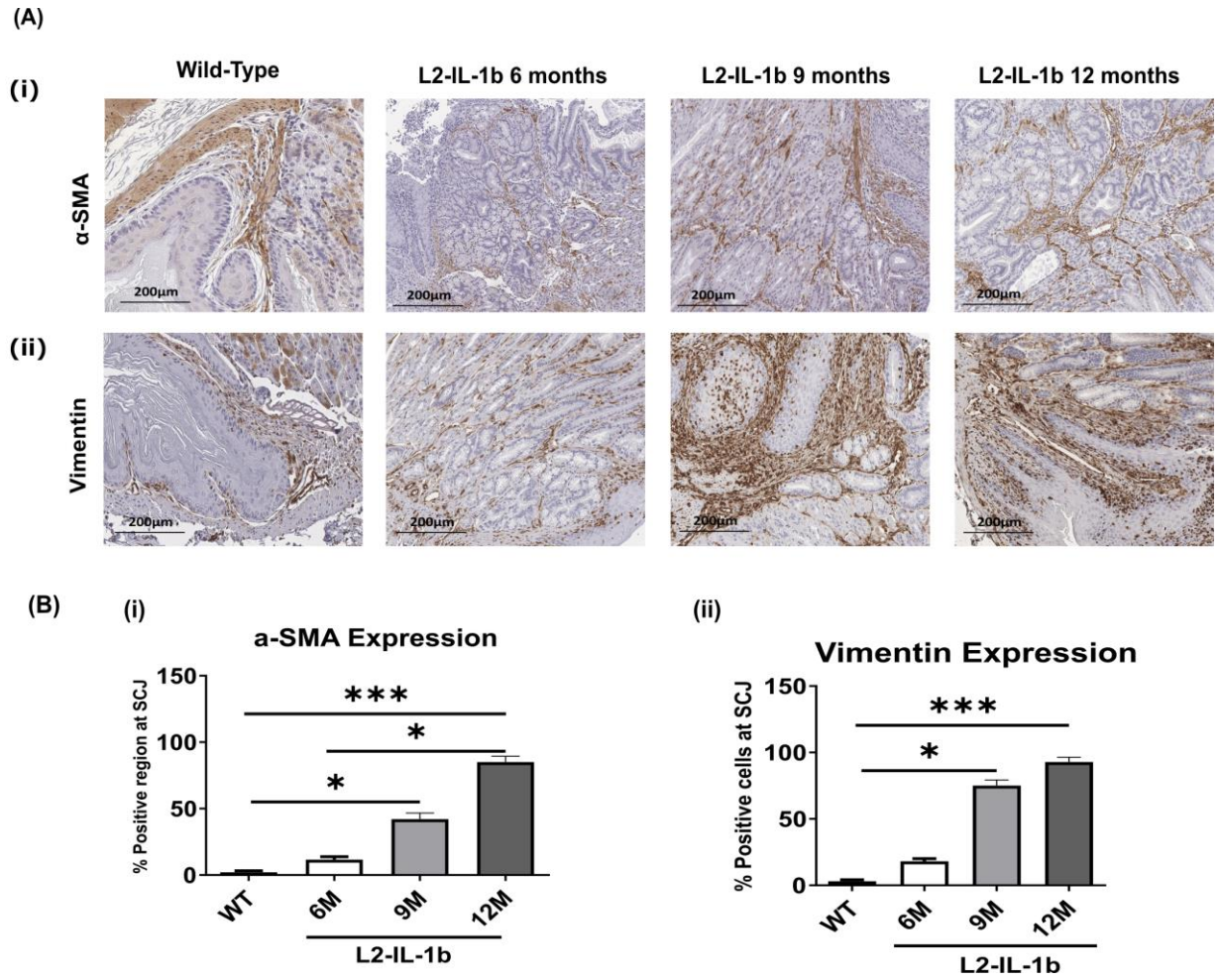

Figure 3.1.1 Expression of a-SMA and vimentin increases in L2-IL-1b mice with time at the SCJ: A (i) Increase in a-SMA expression in WT, 6, 9 and 12-month old L2-IL-1b mice, A (ii) Increase in expression of Vimentin+ cells in WT, 6, 9 and 12-month old L2-IL-1b mice. B (i) Statistical analysis of a-SMA expression in mice from different time-points WT compared to 6, 9 and 12-month-old L2-IL-1b mice (n=5), B (ii) Statistical differences in Vimentin expression in WT, 6, 9 and 12-month old L2-IL-1b mice (n=5). All the images were assessed at 40X magnification. The data is represented as mean±SEM (***p<0.001, **p<0.01, *p<0.05). Multiple comparison t-test was used for analysis.

It has been shown previously that aSMA+ and vimentin+ cells contribute to inflammation-induced carcinogenesis [48]. We also know that NF-kB signalling majorly contributes to tumor initiation and tumor growth in the epithelial cells [89, 90]. As demonstrated earlier in the gene expression analysis [48], inflammatory signalling via IKK-beta/NFkB RelA (p65) is activated by IL-1b receptor signalling as overexpressed in our L2-IL-1b model. Hence as seen in Figure 3.1.2A, we demonstrated that NF-kB was activated in vimentin+ stromal cells at the SCJ of L2-IL-1b mice.

To analyse the effect of NF-kB in stromal cells in a more homogenous environment, we inhibited the NF-kB signalling in myofibroblasts isolated from the SCJ of L2-IL-1b mice by treating them with a specific NF-kB inhibitor (IKK). As seen in Figure 3.1.2B, successful elimination of IKK was confirmed with the western blot after 10 mins of treatment with the inhibitor.

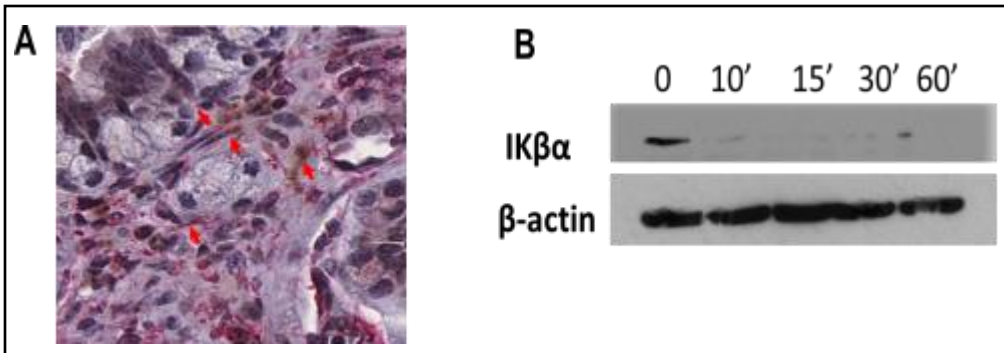

Figure 3.1.2 NF-kB is expressed in stromal cells: (A) Immunohistochemistry shows the expression of NF-kB (pIKα/β) in the vimentin+ stromal cells (n=3). (B) Fibroblasts, when treated with IKK inhibitor, shows downregulation of NF-kB after 10 mins of treatment (n=3).

To look into the fibroblast plasticity, primary esophageal fibroblasts were isolated from L2-IL-1b and WT mice. These fibroblasts were cultured outside of the matrigel drop. Fibroblasts demonstrate a tendency to migrate. In this case, L2-IL-1b fibroblasts at 72hrs showed a higher migration potential and moved towards the centre of the matrigel compared to WT fibroblasts. However, the L2-IL-1b and WT fibroblasts, inhibited for NF-kB signalling, abrogated this migration ability (Figure 3.1.3 A). Statistically, there was a significant decrease in migration of NF-kB inhibited fibroblasts compared to the non-inhibited fibroblasts, as shown in Figure 3.1.3 B. Hence, fibroblasts that are a part of inflammation stroma migrate faster than the fibroblasts, which are a part of the normal stroma. Also, NF-kB plays a crucial role to define this stromal microenvironment.

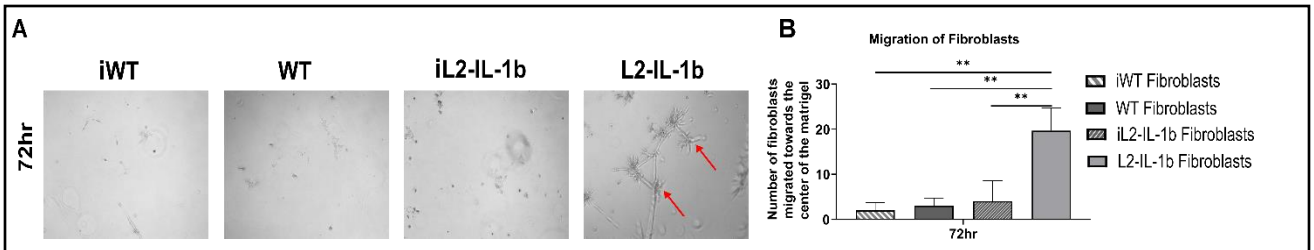

Figure 3.1.3 Migration potential of fibroblasts can be challenged by inhibiting NF-kB signalling: (A) Representative images of fibroblasts isolated from WT and L2-IL-1b mice with and without inhibiting NF-kB. (B) WT fibroblasts showed no migration capacity compared to L2-IL-1b fibroblasts. There was a significant increase in migration of L2-IL-1b fibroblasts compared to inhibited L2-IL-1b fibroblasts (n=3). All the images were assessed at 5X magnification. The data is represented as mean±SEM (***p<0.001, **p<0.01, *p<0.05). Multiple comparison t-test was used for analysis.

3.2 RelA deletion in Vimentin+ stromal cells attenuates the phenotype of L2-IL-1b mice

The canonical NF-kB pathway involves the activation of NF-kB1 p50, RelA (p65) and c-Rel; these subunits exist as heterodimers during the resting stage. When these subunits are triggered by a stimulus, a signalling cascade gets activated in which IkB kinase (IKK) phosphorylates the NF-kB/Rel dimer and translocate this unit into the nucleus [90, 91]. Inflammation has been seen to regulate the activation of NF-kB signalling [91, 92]. To study the role of NF-kB in the stromal cells of an inflammatory environment, an in-vivo mouse model was developed. NF-kB was eliminated in the MFs by crossing L2-IL-1b mice with Vim-Cre (Vim-Cre^{TM}) [93] mice and RelA$^{flox/flox}$(p65$^{fl/fl}$) mice. This lead to the mouse model termed as IL-1b.VimCre^{TM}.p65$^{fl/fl,}$ which was used to analyse the effect of inhibition of RelA in Vimentin-expressing stromal cells in esophageal carcinogenesis.

As shown in Figure 3.2.1 the macroscopic view of a 12-month old IL-1b.VimCre^{TM}.p65$^{fl/fl}$ mice showed a reduced SCJ region and no lesions in the esophagus as compared to the 12-month old L2-IL-1b mice. The IL-1b.VimCre^{TM}.p65$^{fl/fl}$ phenotypic view closer to WT mice. Statistically, the tumor extent and the tumor coverage of IL-1b.VimCre^{TM}.p65$^{fl/fl}$ was seen to be lower than the L2-IL-1b mice both in the cardia and the esophagus regions.

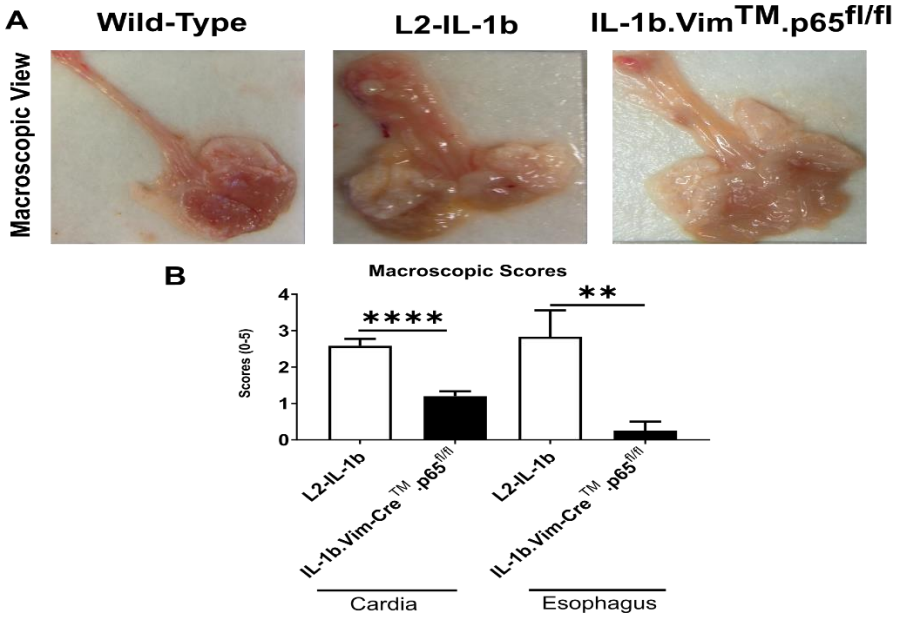

Figure 3.2.1 Macroscopic comparison of 12-month old WT, L2-IL-1b and IL-1b.Vim^{TM}.p65$^{fl/fl}$ mice: A. Physical examination of the different mice groups showed an inflamed and swollen cardia and lesions in the esophagus in L2-IL-1b mice compared to WT mice, but on p65 knock-out, the inflammation was observed to be reduced with normal esophageal epithelium. B. Statistical comparison of the macroscopic scores of the different mice in the cardia and esophagus. The macroscopic lesions in cardia and esophagus reduced significantly in p65 knock-out mice (n=8-10). The data is represented as mean±SEM (***p<0.001, **p<0.01, *p<0.05). An unpaired t-test was used for analysis.

From a histopathological standpoint, IL-1b.VimCre^{TM}.p65$^{fl/fl}$ mice showed reduced transformation to columnar epithelium, which suggests that IL-1b.VimCre^{TM}.p65$^{fl/fl}$ mice have a less severe outcome than L2-IL-1b mice, as shown in Figure 3.2.2A. The statistics in Figure 3.2.2B reflect that IL-1b.VimCre^{TM}.p65$^{fl/fl}$ mice have reduced inflammation and dysplasia, whereas a reduced tendency was observed in metaplasia and goblet-cell formation compared to L2-IL-1b mice.

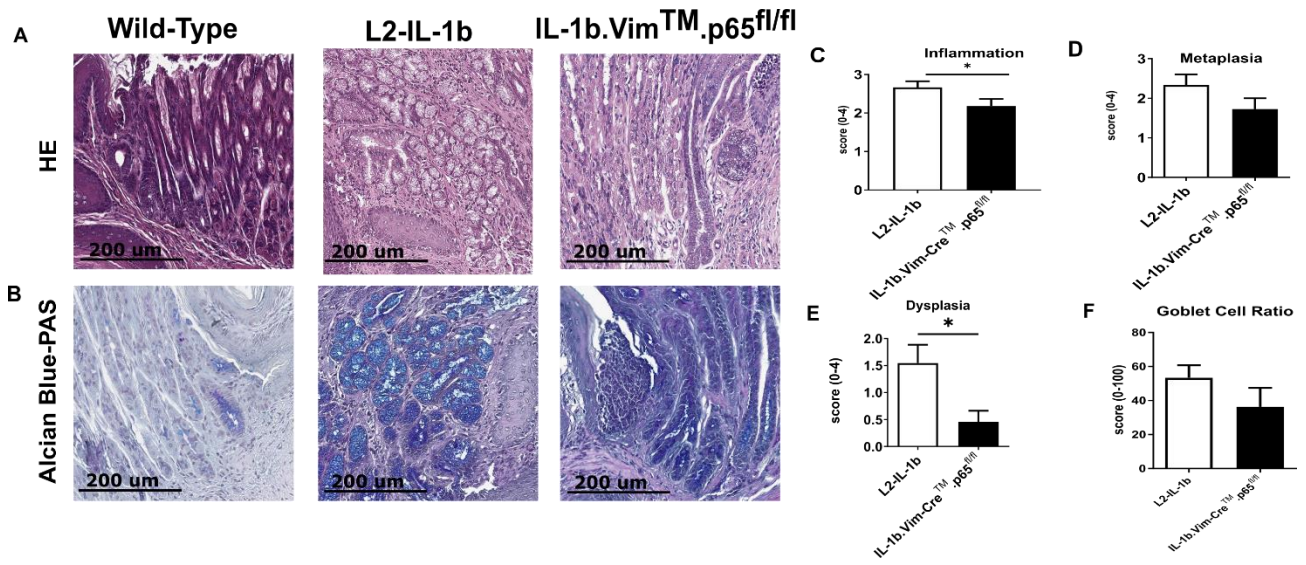

Figure 3.2.2 Histopathological analysis of 12-month old WT, L2-IL-1b and IL-1b.Vim^{TM}.p65$^{fl/fl}$ mice: A. Comparison of the tissue architecture in different mice cohorts from different genotypic groups show a highly dysplastic group of cells in L2-IL-1b mice compared to WT and IL-1b.Vim^{TM}.p65$^{fl/fl}$ mice. B. Presence of goblet cells at the SCJ is comparatively high in L2-IL-1b mice compared to IL-1b.Vim^{TM}.p65$^{fl/fl}$ mice. The statistical evaluation shows a significantly reduced inflammation (C), reduced metaplasia (D), significantly reduced dysplasia (E) and a reduced tendency of goblet cells (F) in IL-1b.Vim^{TM}.p65$^{fl/fl}$ mice compared to L2-IL-1b mice (n=8-10). All the images were assessed at 20X magnification. The data is represented as mean±SEM (***p<0.001, **p<0.01, *p<0.05). An unpaired t-test was used for analysis.

Another important aspect of these mice was to have a look at the proliferation rate of the epithelial cells at SCJ. Immunohistochemistry was performed to do the same, and a significant reduction in the percentage of proliferating positive cells was observed in IL-1b.VimCre^{TM}.p65$^{fl/fl}$ mice in the cardia region. Furthermore, reduced expressions of a-SMA and vimentin were also observed in IL-1b.VimCre^{TM}.p65$^{fl/fl}$ mice. Statistically, a significantly reduced number of proliferating cells were observed in IL-1b.VimCre^{TM}.p65$^{fl/fl}$ mice accompanied by a reduced expression of a-SMA and vimentin at the SCJ as shown in Figure 3.2.3.

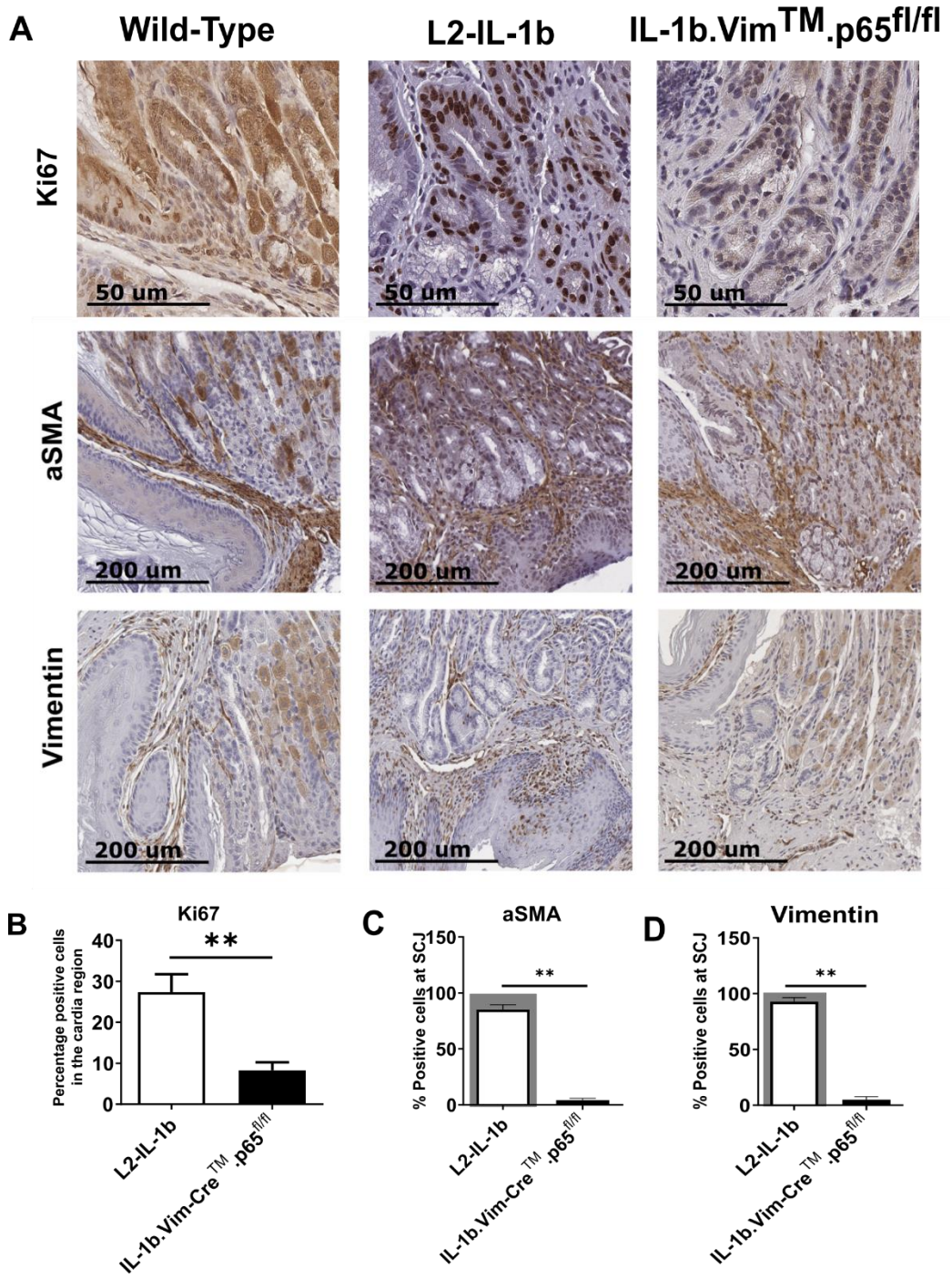

Figure 3.2.3 Immunohistochemistry on 12-month-old WT, L2-IL-1b and IL-1b.VimCre^{TM}.p65$^{fl/fl}$ mice show a significant difference in the expression levels: Markers for Ki67 (A), a-SMA (B) and Vimentin (C) expressed at the SCJ of the different mice and showed a variation in the expression levels. Statistical differences were observed in the proliferation marker with reduced proliferation in IL-1b.VimCre^{TM}.p65$^{fl/fl}$ mice (D). Followed by a reduced expression of stromal cell markers in IL-1b.VimCre^{TM}.p65$^{fl/fl}$ mice at the SCJ (E) and (F) (n=5). All the images were assessed at 40X magnification. The data is represented as mean±SEM (***p<0.001, **p<0.01, *p<0.05). An unpaired t-test was used for analysis.

These datasets suggest that inflammatory vimentin+ MFs contribute to the progression of esophageal carcinogenesis via NF-kB stimulated pathways.

3.3 Inflammatory epithelial cells indicate growth modulations when surrounded by fibroblasts

Based on histopathological analysis, it was observed that Vimentin+ MFs have an effect on the inflammatory epithelial cells of the tumor niche. To observe these changes in a homogenous environment and closely analyse the cross-talk between the two cell types, an in-vitro setting was established. Epithelial organoids from the SCJ of WT and L2-IL-1b mice were isolated and cultured to obtain a homogenous population. These organoids were subjected to interact with primary esophageal fibroblasts also isolated from WT and L2-IL-1b mice. In one of the conditions, both phenotypic organoids were co-cultured with the corresponding phenotypic fibroblasts. In the other condition, they were co-cultured with the corresponding phenotypic fibroblasts with NF-kB signal inhibition as seen in Figure 3.3.1 A and B. Based on this cell-cell direct communication, the effects on the epithelial organoids were noted. As seen in Figure 3.3.1C, after 72 hours, there was no effect on WT organoids, but a significant number of L2-IL-1b fibroblasts migrated towards the L2-IL-1b organoids compared to inhibited L2-IL-1b fibroblasts. This cell-cell interaction also impacted the size of the organoids after 24 hours, as seen in Figure 3.3.1D, wherein an increasing trend was observed with co-culture of L2-IL-1b fibroblasts with L2-IL-1b organoids. Still, the size of WT organoids was comparatively constant regardless of whether they were cultured with inhibited or non-inhibited WT fibroblasts. As a result of these changes, the growth characteristics of the organoids were also affected. After 24 hours, L2-IL-1b organoids expanded significantly more in number when co-cultured with L2-IL-1b fibroblasts than when co-cultured with inhibited L2-IL-1b fibroblasts. However, no impact was observed on WT organoids with the co-culture of inhibited and non-inhibited WT fibroblasts as seen in Figure 3.3.1E.

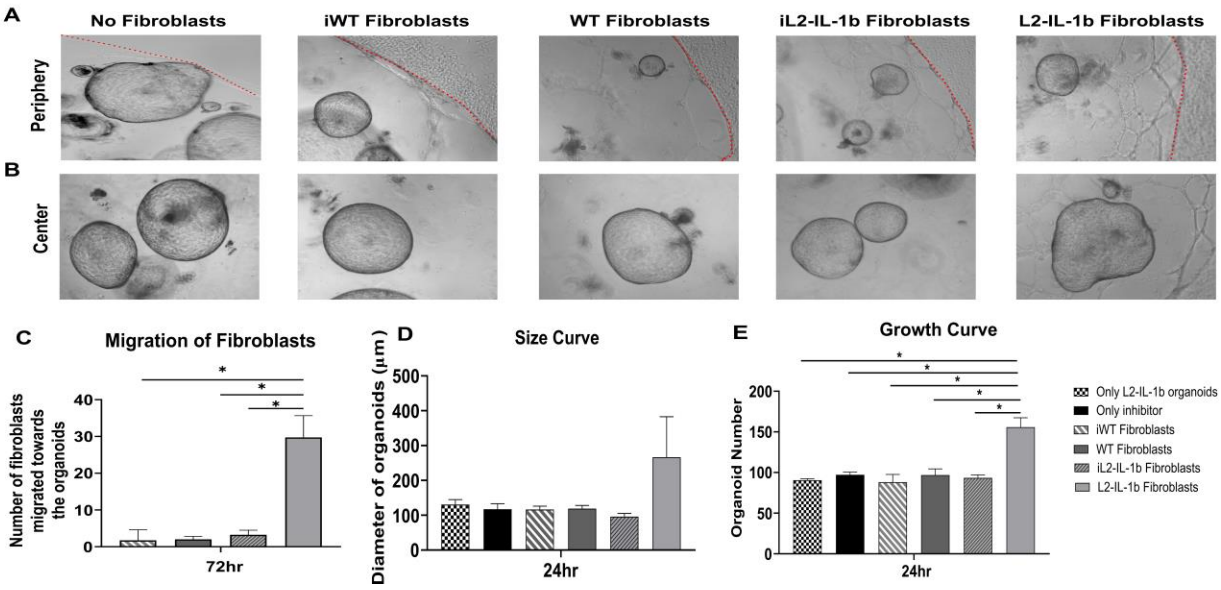

Figure 3.3.1 In-vitro analysis of the effect of NF-kB inhibition in primary fibroblasts on the neighbouring epithelial cells: L2-IL-1b fibroblasts in their original state migrated from the periphery of the Matrigel to the center compared to the inhibited L2-IL-1b fibroblasts and WT inhibited and not inhibited fibroblasts (A) and (B). The statistical analysis reflected the migration tendency, which showed a significant number of L2-IL-1b fibroblasts migrated towards the epithelial organoids compared to the other groups (C). This migration affected the size (D) and the growth (E) of the epithelial organoids significantly (n=6). All the images were assessed at 5X magnification. The data is represented as mean±SEM (***p<0.001, **p<0.01, *p<0.05). Multiple comparison t-test was used for analysis.

Furthermore, a co-culture experiment was set up to examine whether the findings from mice co-culture experiments can also be replicated in humans. Human organoids were cultured together with FEF cells with and without IKK inhibitor. As seen in Figure 3.3.2, the results coincided with the mice data hereby, resulting in a decrease in the size of human organoids co-cultured with inhibited FEF cells compared to human organoids co-cultured with FEF cells at 48 hours. Additionally, the growth of human organoids was significantly reduced after 48h when the FEF cells were inhibited.

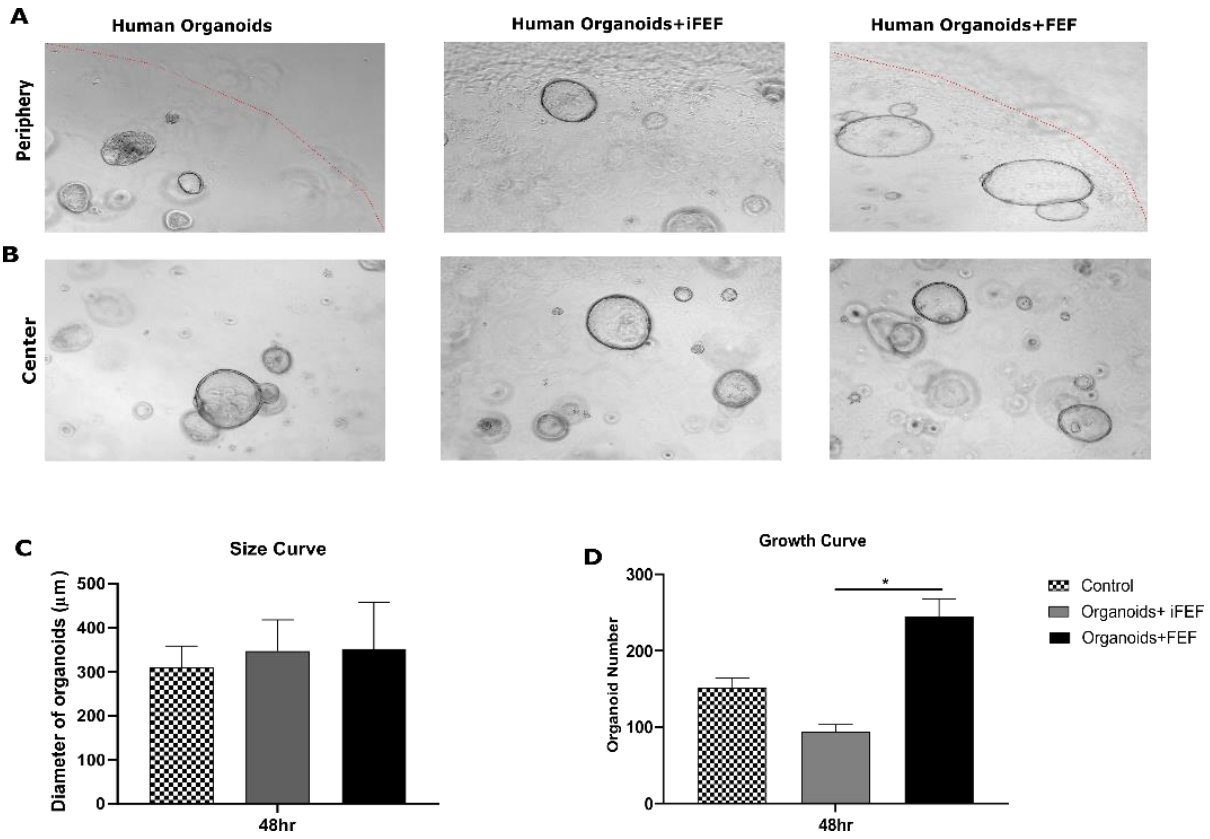

Figure 3.3.2 In-vitro co-culture of human organoids with FEF cells mimics the findings of in-vitro mouse organoid-fibroblast co-culture: (A) and (B) Human organoids derived from the endoscopic biopsy from the Barrett junction of the human patients co-cultured with FEF cells showed a visible migration of FEFs towards the epithelial organoids compared to the inhibited FEF cells. (C) shows the changes in the size of the organoids, which does not change significantly. (D) shows a significant decrease in the human organoids cultured with iFEF cells compared to FEF cells (n=3). All the images were assessed at 5X magnification. The data is represented as mean±SEM (***p<0.001, **p<0.01, *p<0.05). Multiple comparison t-test was used for analysis.

Hence, the in-vitro findings of both mice and humans demonstrated that NF-kB signalling is involved in the migration of the fibroblasts. It also plays are role in defining the growth of the inflamed epithelial cells. However, when it is inhibited in the fibroblasts, the migration and the expansion of the epithelial cells is attenuated. This reaffirms the hypothesis that inflamed epithelial cells are supported by the stromal cell niche via NF-kB signalling, and when this pathway is knocked-out it can diminish its effect on the epithelial cells hence it can lead to reduction in inflammatory epithelial cell growth.

3.4 NF-kB elimination in vimentin+ cells change chemokine and cytokine levels

Stromal cells are involved in various processes in the tumor microenvironment, such as migration, proliferation and angiogenesis. These cells can directly or indirectly modulate the functions and can impact the epithelial cells. Hence, to further analyse the role of NF-kB elimination in vimentin-expressing stromal cells on the surrounding tumor epithelial cells, a cytokine array was performed using tissue from both the esophagus and the cardia region of the stomach from IL-1b.VimCre^{TM}.p65$^{fl/fl}$ mice and compared them with L2-IL-1b mice. The different cytokines were sub-grouped according to their functions, as seen in Figure 3.4. Tumor Necrosis Factor (TNF) family is one of the primary activators in NF-kB signalling, which instigates the activation of IKKs. BAFF and CD40 are associated with the TNF family [94]. As seen in Figure 3.4.1A, the expression of these proteins is reduced in IL-1b.VimCre^{TM}.p65$^{fl/fl}$ tissue compared to L2-IL-1b tissue. This indicates that low amounts of BAFF and CD40 reduce the NF-kB activity in IL-1b.VimCre^{TM}.p65$^{fl/fl}$ mice. Similarly, the protein levels of key chemokines and cytokines CCL5 and CXCL1, which are involved in defining tumor growth and invasion [13, 95], showed a decrease in their expressions, as seen in Figure 3.4.1B. Proteins involved in angiogenesis such as matrix metalloproteinases (MMPs), fibroblast growth factor (FGF) and vascular cell adhesion molecule-1 (VCAM-1) and those responsible for migration of stromal cells like HGF and CXCL13 also showed reduced expression levels in IL-1b.VimCre^{TM}.p65$^{fl/fl}$ tissue as seen in Figure 3.4.1C. From this analysis it can be deduced that the elimination of RelA in vimentin+ stromal cells dysregulates the NF-kB signalling in epithelial cells of the tumor microenvironment at the SCJ of IL-1b.VimCre^{TM}.p65$^{fl/fl}$ mice. This dysregulation leads to a reduced tumor burden which can be seen histopathologically via reduced inflammation, dysplasia and proliferation of epithelial cells in these mice.

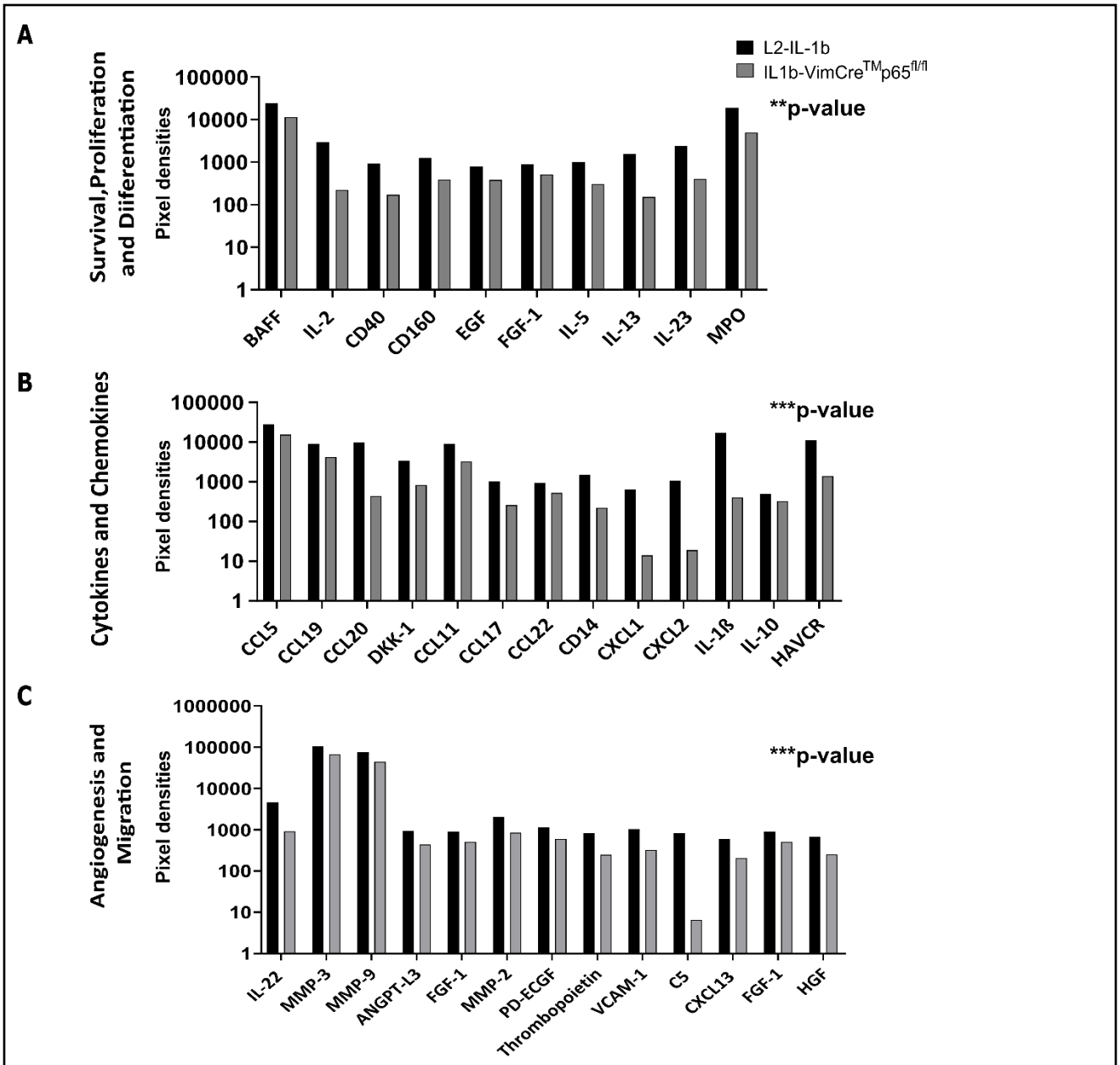

Figure 3.4.1 Reduced levels of chemokines and cytokines were observed in IL-1b.VimCre™.p65$^{fl/fl}$ mice: (A) Comparison of the pixel densities of the expression of proteins responsible for proliferation, differentiation and survival of cells in vivo. (B) Comparison of various chemokines and cytokines released in the tumor microenvironment upon the interaction of epithelial and stromal cells. (C) Comparison of proteins released responsible for the angiogenesis and migration of stromal cells towards the epithelial cells (n=4). For p-values (***p<0.001, **p<0.01, *p<0.05) paired t-test was used for analysis.

T-cells form a poignant part of the esophageal tumor niche in human patients. Two chemokines CCL5 and MIP-3α, were seen to be enriched in EAC patients [96]. Hence, the levels of these proteins were analysed in an in-vitro setting. 3D organoids were cultured from resected tissue from the barrett region. These organoids were subjected to co-culture with inhibited and non-inhibited FEF cells. As seen in Figures 3.4.2A and B, the protein levels for MIP-3α reduced from 588 to 413 pg/ml, and for CCL5, the levels reduced from 165 to 93 pg/ml after 24 hours. Therefore, it can be implied that the chemokine signalling can be attenuated in human patients by altering the NF-kB pathway in human fibroblasts.

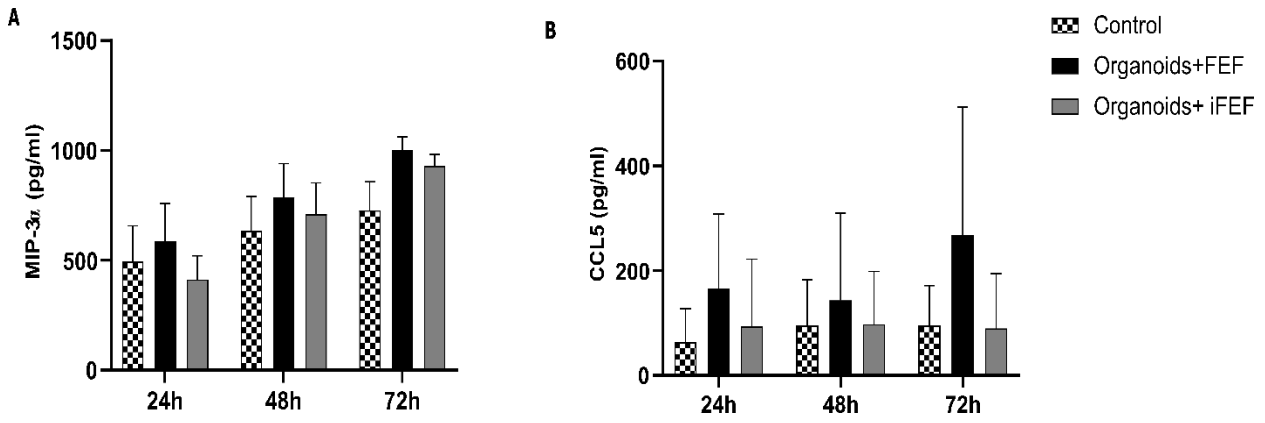

Figure 3.4.2 Protein analysis of MIP-3α and CCL5 markers in human organoids: (A) The cytokine levels of MIP-3α are elevated from 24 to 72 hours in organoids cultured with FEF cells compared to the ones cultured with iFEF cells (n=3). (B) The levels of CCL5 are also elevated from 24 to 72 hours in organoids cultured with FEF cells compared to the ones treated with iFEF cells (n=3).

Chapter 4: Result II

4.1 Effect of mutations in EAC mouse model

The link between inflammation and cancer has been well studied and established [97]. Inflammation has been identified as a critical component in tumor progression. This progression, however leads to changes in the DNA of the cells, hence causing mutations. Therefore, mutations are the underlying cause of tumorigenesis [98]. To integrate this knowledge for a deeper understanding of EAC, we generated a mouse model driven by key driver mutations and mimics human EAC.

In order to develop this mouse model, we utilized the already established inflammation-based BE mouse model, which has overexpression of the L2-IL-1b gene. This model has the ability to induce chronic inflammation and develop high-grade dysplasia at the SCJ in 12-15 months [11]. Furthermore, to induce mutations specific to SCJ, we used Lgr5-EGFP-ires-CreERT/2 (Lgr5) mice [99]. Lgr5 has been described as an actively cycling stem cell in the basal epithelial cells in the squamous esophagus and identified as a gastric cardia progenitor cell [100]. Therefore, to introduce the conditional knock-in/out, L2-IL-1b (L2) mice were crossed with Lgr5 (L) mice which gave us *L2-IL-1b.Lgr5-EGFP-ires-CreERT/2/+* (L2-L) mice.

We selected three genetic mutations that play a pivotal role in the disease progression according to different WGS studies carried over the past years and the recent TCGA data. These mutations are LSL-KRasG12D (K) [71], Tp53 (P) [76] and Rb (R) [82, 84].

To investigate the role of these individual mutations, mice bearing these single mutations flanked with the loxP sites at the mutation-specific exon sites as shown in Figures 1.4.2, 1.4.3 and 1.4.4 were crossed with L2-L mice. This resulted in *L2-IL-1b.Lgr5-EGFP-ires-CreERT/2/+.KRasG12D/+* (L2-LK), *L2-IL-1b.Lgr5-EGFP-ires-CreERT/2/+.p53-/-* (L2-LP), *L2-IL-1b.Lgr5-EGFP-ires-CreERT/2/+.p53+/-* (L2-LP+/-), *L2-IL-1b.Lgr5-EGFP-ires-CreERT/2/+.Rb-/-* (L2-LR) and *L2-IL-1b.Lgr5-EGFP-ires-CreERT/2/+.Rb+/-* (L2-LR+/-) combinations. All these different genotypic mice were induced with tamoxifen via tamoxifen food at 4 months and kept until 7 months. Lgr5 and KRasG12D were conditional knock-in alleles, whereas p53 and Rb were conditional knock-out alleles. Tamoxifen induction led to the expression of Lgr5 and KRas, whereas it led to the deletion of p53 and Rb activity in the epithelial cells. L2-L mice wherein Lgr5 functioned as the cre, was used as a control to compare different genotypes.

As shown in Figure 4.1.1A, control L2-L was compared macroscopically with L2-LR, L2-LP and L2-LK. L2-LR mice showed a visual resemblance with the control L2-L mice. Similarly, L2-LP mice also resembled macroscopically with L2-L mice. There was no visible inflammation observed in the cardia region in L2-L, L2-LR and L2-LP mice. However, there was a striking difference observed at the cardia region of L2-LK mice. In these mice, the cardia region appeared to be inflamed and enlarged compared to control L2-L mice and L2-LR and L2-LP mice. From the histopathological viewpoint, as shown in Figure 4.1.1B, L2-LR and L2-LP mice showed low-grade dysplasia in the epithelial cells at the SCJ compared to the L2-L group, which showed a few metaplastic cells. Hence, this suggests that p53 and Rb inactivation alter epithelial cells' growth and advance the disease to be low-grade dysplastic. However, L2-LK mice showed a relevant number of high-grade dysplastic cells at SCJ. This suggests that mutant KRas is more aggressive in progressing the disease compared to p53 and Rb. Proliferation is an important marker to account for the aberrant growth of epithelial cells in a particular disease. Hence Ki67 staining was performed, which showed very few proliferative cells at SCJ in L2-L, L2-LR and L2-LP groups. In contrast, more proliferating cells were seen in the cardia region of L2-LK mice, as shown in Figure 4.1.1C.

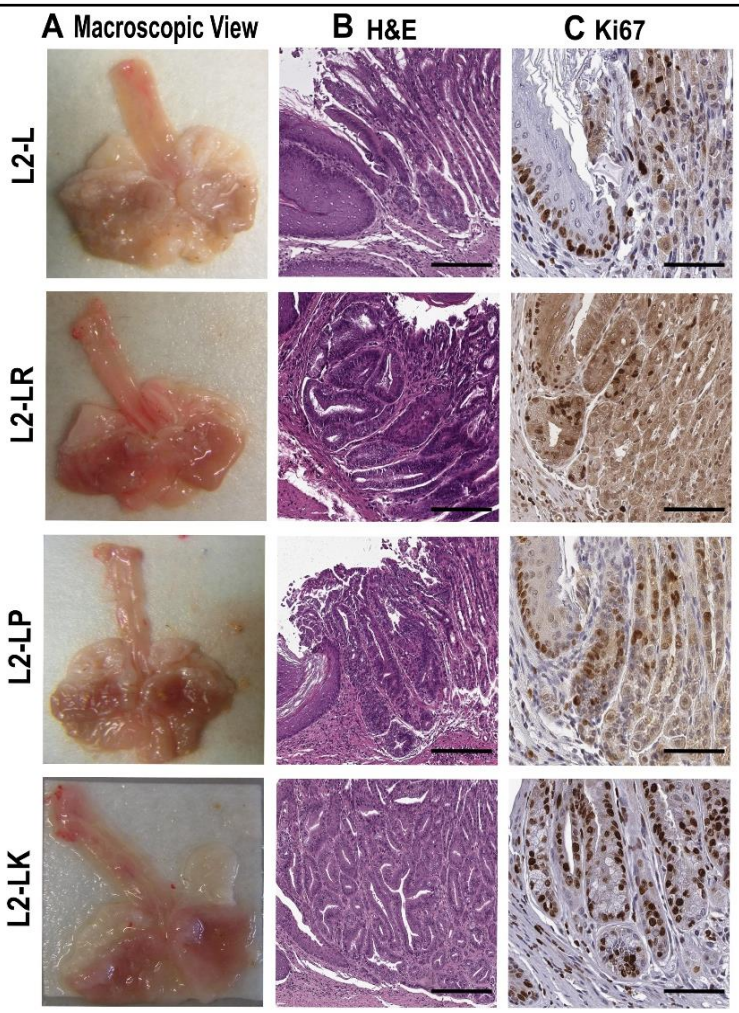

Figure 4.1.1 Single mutations in L2-IL-1b mice causes changes at the histopathological level. (A) Macroscopic comparison of L2-L, L2-LR, L2-LP and L2-LK mice, (B) Histological view of the tissue architecture at SCJ; Images were taken at 20X. Scalebar 200µm, (C) Proliferation capacity of the cells with different single mutations at SCJ; Images were taken at 40X. Scalebar 50µm.

Statistically, as indicated in Figure 4.1.2A, there was no difference in the macroscopic scores of L2-LR compared to L2-L and L2-LP compared to L2-L. There was a significant difference in the macroscopic scores of the L2-L and L2-LK groups. As shown in Figure 4.1.2B, the summary statistics compared the distribution of macroscopic scores according to the number of mice of a particular score corresponding to a particular genotype. This distribution reflected that L2-LK mice have a severe phenotype, wherein 2/12 mice developed tumors >2mm compared to L2-L, L2-LR and L2-LP groups in which the maximum tumor size achieved was ≤1mm. Histopathologically, as shown in Figure 4.1.2C, there was an increase in inflammation observed at the SCJ of L2-LR, L2-LP and L2-

LK groups compared to L2-L control mice. However, the inflammation was significantly high in the L2-LR group compared to the control L2-L group. In Figure 4.1.2D, an increase in metaplasia was observed in L2-LR, L2-LP and L2-LK groups compared to the L2-L group. This increase was significant in L2-LR and L2-LK groups compared to the L2-L group. Furthermore, an increase in dysplasia grading was observed inL2-LR, L2-LP and L2-LK groups compared to the L2-L group, as shown in Figure 4.1.2E. A significant difference was seen between L2-L and L2-LK groups where L2-L mice developed no dysplasia compared to L2-LK mice which developed low-grade to high-grade dysplasia. However, for L2-LR and L2-LP groups, the histological structure of the cells varied from no dysplasia to low-grade dysplasia only. These groups showed no highly dysplastic cell formation. This suggested that Rb and p53 alone have a low disease driving impact compared to KRas. As we observed from the pathological analysis, KRas is a prominent mutation for the progression of the disease. 22% (2/9) mice in the L2-LK group developed high-grade dysplasia, whereas none of the mice in L2-LR developed dysplasia compared to 11% (1/9) mice in L2-LP, which developed low-grade dysplasia. However, in control L2-L group, 79% (11/14) of mice developed no dysplasia. The proliferation data also supported the macroscopic and histopathological findings. Mice that belonged to the L2-LK group had the highest number of proliferative cells compared to mice in the L2-L group. However, there was a significant increase in the number of proliferative cells in L2-LR and L2-LP groups compared to the L2-L group. Hence, from this data, we could conclude that among the chosen mutations, LSL-KRasG12D has the most potential to drive the pathogenesis of the disease.

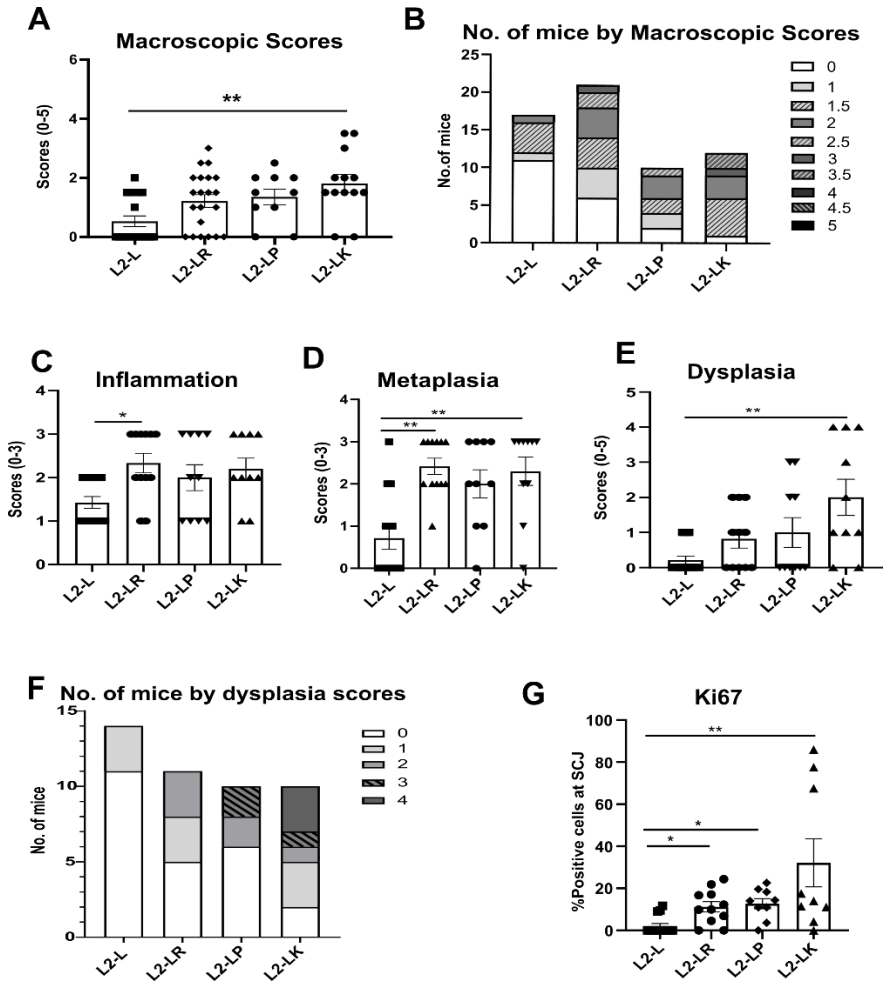

Figure 4.1.2 Statistical analysis shows significant disease progression in L2-LK mice compared to L2-LR and L2-LP mice. (A) Macroscopic evaluation of the tumor coverage and (B) Distribution of scores according to the number of mice for different genotypes (n=10-20). Histopathological analysis on the parameters of inflammation (C), Metaplasia (D) and Dysplasia (E) and the distribution of dysplasia scores according to the number of mice for every single mutated genotype (n=10-14). (F) Expression of Ki67 to mark proliferating cell at the SCJ (n=9-11). The data is represented as mean±SEM (***p<0.001, **p<0.01, *p<0.05). Multiple comparison t-test was used for analysis.

Since EAC tumors are developing from a heterogeneous pool of somatic mutations [18, 24], it is important to investigate the effect of single mutations and mutational combinations such as p53-Rb, KRas-p53 KRas-Rb and KRas-p53-Rb. We generated the following mouse lines to study the impact of different mutation combinations in tumorigenesis: *L2-IL-1b.Lgr5-EGFP-ires-CreERT/2/+.p53-/-.Rb-/-* (L2-LPR), *L2-IL-1b.Lgr5-EGFP-ires-CreERT/2/+.KRasG12D/+.Rb-/-* (L2-LKR), *L2-IL-1b.Lgr5-EGFP-ires-CreERT/2/+.KRasG12D/+.p53-/-* (L2-LKP) and *L2-IL-1b.Lgr5-EGFP-ires-CreERT/2/+.KRasG12D/+.p53-/-.Rb-/-* (L2-LKPR). These mice were induced with tamoxifen at the

age of 4 months and were kept until 7 months except L2-LKPR mice which survived until 6 months only. As seen in Figure 4.1.3A, the different combinations showed us that L2-LPR mice developed very small tumors by the age of 7 months contrary to the KRas combinations with Rb and p53 (L2-LKR; L2-LKP; L2-LKPR), which developed continuous tumors in the cardia region at the age of 6-7 months. As shown in Figure 4.1.2B, L2-LPR mice developed few dysplastic but mostly metaplastic cells at the histopathology level. However, L2-LKR, L2-LKP and L2-LKPR mice developed highly dysplastic to poorly differentiated cells, leading to invasive cancer in these mice. Proliferation in the epithelial cells at SCJ, as shown in Figure 4.1.3C, also complemented with the histological findings wherein a high number of proliferative epithelial cells were observed in the dysplastic region of L2-LPR mice and the tumor regions of L2-LKR, L2-LKP and L2-LKPR mice.

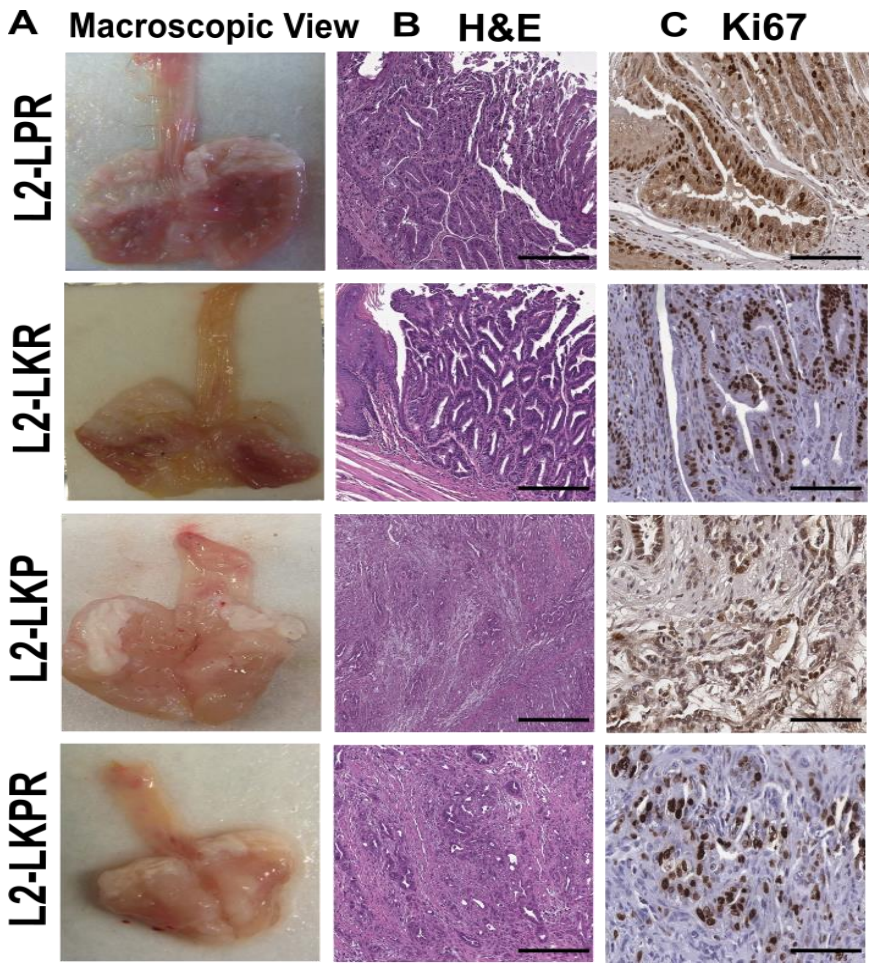

Figure 4.1.3 Mutational combinations in L2-IL-1b mice results in tumor phenotype: Representative images show (A) Macroscopic view of the mutational combinations L2-LPR, L2-LKR, L2-LKP and L2-LKPR, (B) Histopathological structure of cells to form a tumorigenic tissue architecture, images were taken at 20X magnification. Scalebar 200 µm (C) Proliferation of epithelial cells at the SCJ in different combinations, images were taken at 40X magnification. Scalebar 50 µm.

As shown in Figures 4.1.4A and B, the L2-LPR group developed a significantly lower number of macroscopic tumors with 57% (8/14) mice which showed 50-80% tumors with tumor size < 2mm compared to L2-LKR. L2-LKR mice had 53% (8/15) mice which developed tumors ~80% with an average tumor size of ≥3mm. L2-LKP mice had 50% (5/10) mice that developed continuous tumors with a tumor extent of ≥80% and a 5-8mm tumour size. Interestingly, L2-LKPR had the highest significance with 71% (12/17) of the mice which developed complete tumors with 100% tumor extent and a tumor size ranging from 5-16mm. The histopathological evaluation classified into inflammation, metaplastic and dysplastic stages showed no significant differences in the inflammatory cells and metaplastic glands at the SCJ (Figure 4.1.4C and D) among the different genotypes. However, only

20% (2/10) mice from the L2-LPR group developed high-grade dysplasia, whereas in L2-LKR and L2-LKP groups, 82% (9/11) and 83% (10/12) mice developed high-grade dysplasia to tumor phenotype, respectively. The disease was highly accelerated in the L2-LKPR group, where 93.75% (15/16) mice developed high-grade dysplasia to invasive cancer, as seen as the distribution of scores and number of mice across different genotypes in Figure 4.1.4E and F, respectively. To understand different stages of cancer, we further classified the mice which developed cancer into different grades. In Figure 4.1.4G, we observed that overall, the KRas mutated groups included a high number of mice that developed well-differentiated carcinoma (G1 T1). Specifically, in the L2-LKR group, we obtained moderately differentiated carcinoma in some mice, which got as worse as poorly differentiated carcinoma in L2-LKP and L2-LKPR groups. Apart from the stomach, certain irregular dysplastic cells and adenoma regions were observed in the duodenum of the small intestine and colon of L2-LKR mice. However, there were no metastases seen in any other organ for any of the groups. With such a severe histological diagnosis, it was evident that the cells are highly proliferative. Upon quantification, it was seen that KRas combination groups developed a higher proliferative index as shown in Figure 4.1.4H with nearly 100% proliferation compared to the non-KRas mutated group L2-LPR wherein the cells achieved an average of 25% proliferation only.

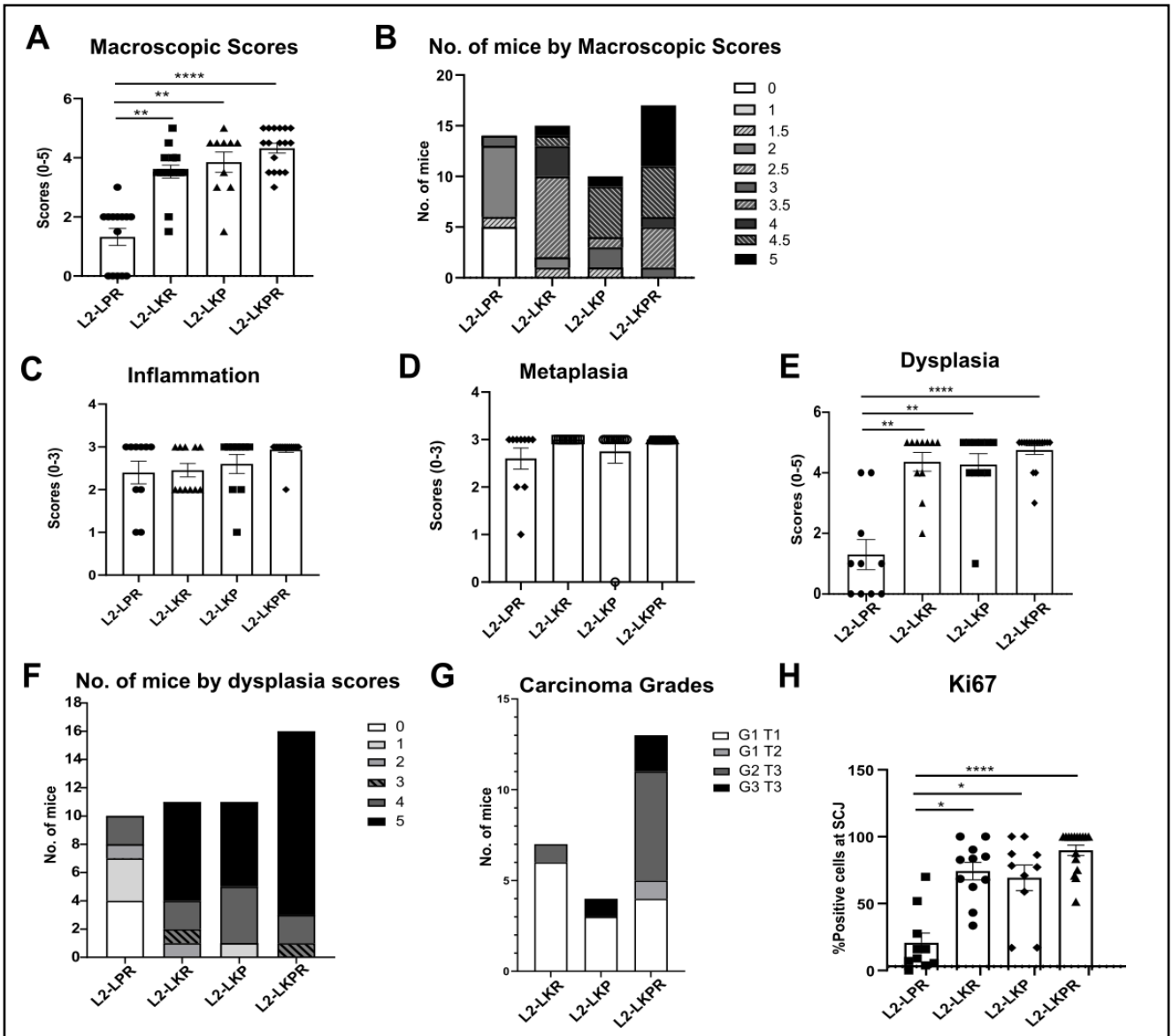

Figure 4.1.4 Statistical evaluation of the macroscopic and pathological observations: (A) and (B) Comparison of macroscopic scores with respect to the individual scores for different genotypic combinations and distribution of different scores in a particular genotype (n=10-16), Histopathological evaluation based on (C) Inflammation, (D) Metaplasia, (E) Dysplasia, (F) Distribution of the dysplasia scores for particular genotypes (n=10-16) and (G) Distribution of carcinoma grades (n=4-13), (H) Evaluation of the epithelial cell proliferation at SCJ in different combinations (n=10). The data is represented as mean±SEM (****p<0.0001, ***p<0.001, **p<0.01, *p<0.05). Multiple comparison t-test was used for analysis.

Adding on to the homozygous mice lines their corresponding heterozygous combinations led to the generation of the following combinations: *L2-IL-1b.Lgr5-EGFP-ires-CreERT/2/+.p53+/-.Rb+/-* (L2-LP+/-R+/-), *L2-IL-1b.Lgr5-EGFP-ires-CreERT/2/+.p53+/-.Rb-/-* (L2-LP+/-R-/-), *L2-IL-1b.Lgr5-EGFP-ires-CreERT/2/+.p53-/-.Rb+/-* (L2-LP-/-R+/-), *L2-IL-1b.Lgr5-EGFP-ires-*

CreERT/2/+.KRasG12D/+.Rb+/- (L2-LKR+/-), *L2-IL-1b.Lgr5-EGFP-ires-CreERT/2/+.KRasG12D/+.p53+/-* (L2-LKP+/-), *L2-IL-1b.Lgr5-EGFP-ires-CreERT/2/+.KRasG12D/+.p53+/-.Rb+/-* (L2-LKP+/-R+/-), *L2-IL-1b.Lgr5-EGFP-ires-CreERT/2/+.KRasG12D/+.p53+/-.Rb-/-* (L2-LKP+/-R-/-) and *L2-IL-1b.Lgr5-EGFP-ires-CreERT/2/+.KRasG12D/+.p53-/-.Rb+/-* (L2-LKP-/-R+/-).

In the case of heterozygous combinations without KRas (Figure 4.1.5A), the phenotype showed no remarkable differences. Histopathologically, the epithelial cellular structure varied from metaplastic to low-grade dysplastic cells (Figure 4.1.5B). Corresponding to the macroscopic and histological scores, the proliferation was seen in the metaplastic and dysplastic cells at the SCJ for each mutation and mutation combination (Figure 4.1.5C).

Figures 4.1.6A and B show that the average macroscopic score showed 20-50% of tumors. The epithelial cells mostly attained atypical architecture, and the epithelial tissue showed the development of mostly metaplastic cells at the SCJ. The histopathological scores for inflammation, metaplasia and dysplasia for the heterozygous groups can be seen in Figure 4.1.6 C, D, E and F. The groups show no significant differences among each other. These atypical and metaplastic cells achieved an average proliferation rate of 20%, plotted in a graph in Figure 4.1.6G.

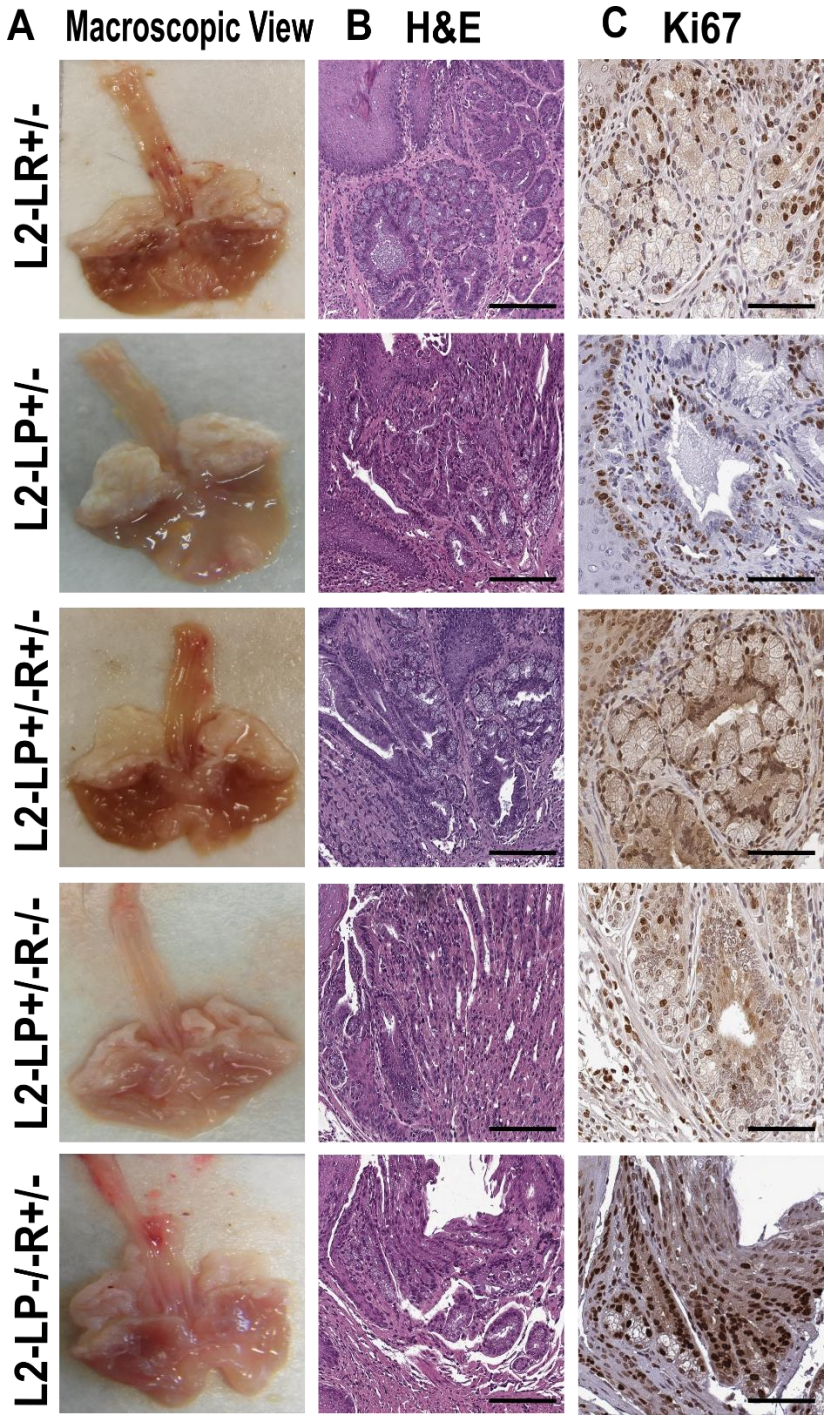

Figure 4.1.5 Heterozygous mutational combinations show no potential increase in the disease progression: Representative images of (A) Macroscopic view of the stomach and the SCJ, (B) Histological view of the tissue architecture at SCJ, images were taken at 20X magnification. Scalebar 200 µm and (C) Proliferation in the epithelial cells at the SCJ, images were taken at 40X magnification. Scalebar 50 µm

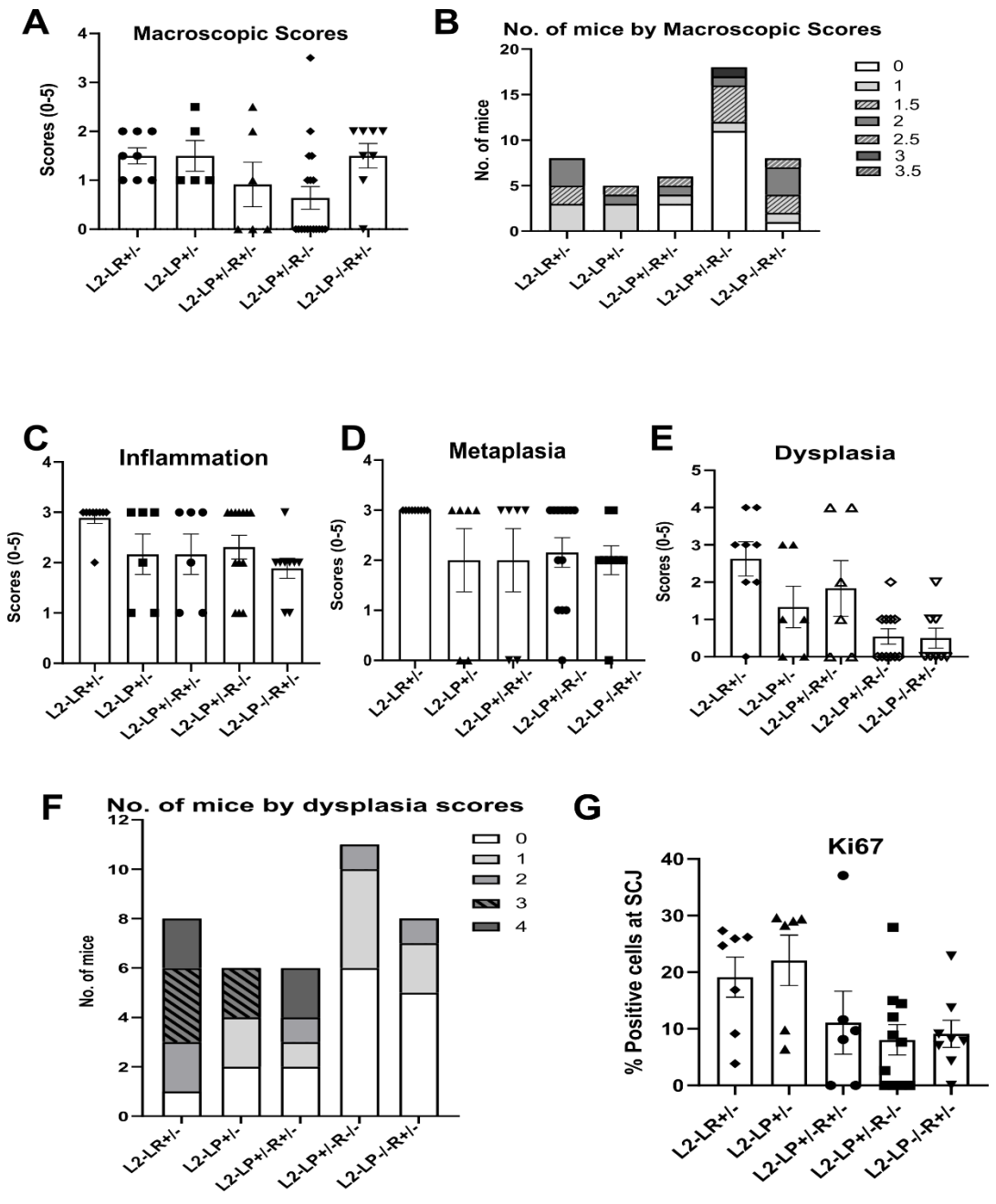

Figure 4.1.6 Statistical evaluation of the non-KRas mutated heterozygous combination of p53 and Rb genes: The data shows no significant difference in the (A) and (B) Macroscopic tumor extent and coverage of lesions, Histological evaluation show no difference in (C) Inflammation, (D) Metaplasia (E) and (F) Dysplasia in different combinations. (G) No difference was seen in the proliferative index of the epithelial cells at the SCJ. The data is represented as mean±SEM (****p<0.0001, ***p<0.001, **p<0.01, *p<0.05). Multiple comparison t-test was used for analysis.

For the KRas mediated heterozygous groups (Figure 4.1.7A), the macroscopic observations showed some differences compared to the non-KRas heterozygous combinations. There was a development of lesions and tumor-like structures observed in the cardia region of the stomach, specifically in L2-LKP+/-R+/-, L2-LKP+/-R+/- and L2-LKP-/-R+/- groups. Similarly, in the histological evaluation (Figure 4.1.7B), the development of dysplastic and undifferentiated cells was observed in these groups, supported by a high content of proliferative cells in the region (Figure 4.1.7C). As evaluated in Figure 4.1.8 A and B, compared to 20-50% tumor macroscopic score in non-KRas groups, a higher macroscopic score was observed with 50-80% tumors in L2-KR+/-, L2-LKP+/- and L2-LKP+/-R+/- groups but 80-100% tumors in L2-LKP-/-R+/- and L2-LKP+/-R-/- groups. Adding on, the histopathological scoring in Figure 4.1.8 C, D, E and F showed 36% (4/7) mice from L2-LKR+/- group and 33.33% (2/6) mice from L2-LKP+/- group attained high-grade dysplasia. However, the triple transgenic combinations, L2-LKP+/-R+/-, L2-LKP-/-R+/-, L2-LKP+/-R-/-, showed an increased progression to carcinogenesis. Epithelial cells in triple transgenic mice transitioned from highly dysplastic to well-differentiated carcinoma with 71.43% (5/7) L2-LKP+/-R+/-, 54.56% (6/11) L2-LP+/-R-/- and 66.67% (6/9) L2-LKP-/-R+/- mice developed dysplastic or tumor tissue formation. The histological findings co-related with the proliferation index of the epithelial cells in these dysplastic or cancer regions high rate of proliferating rate of 50-100% epithelial cells compare in Figure 4.1.8G. This data suggests a sub-group of EAC, which is KRas driven, and when combined with other mutations, it can accelerate the disease. However, it seems that in this mouse model, p53 and Rb mutations could not drive the disease by themselves, but they behave like passenger mutations which, when coupled with KRas, have the potential to enhance tumorigenesis.

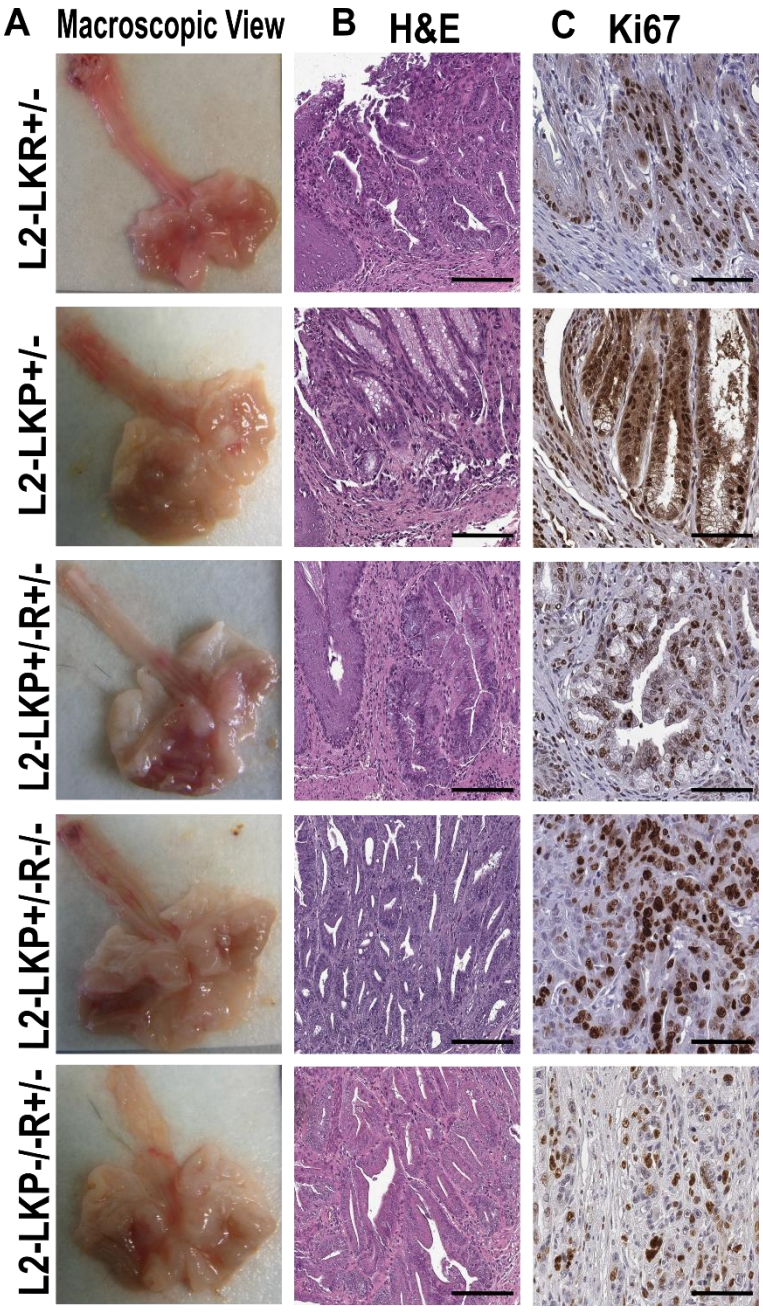

Figure 4.1.7 KRas-mediated combinations with p53 and Rb genes can induce tumor formation at the SCJ: Representative images of (A) Macroscopic view of the stomach for different combinations, (B) Histological evaluation of the stomach tissue focussed at the SCJ, images were taken at 20X magnification. Scalebar 200 µm and (C) Proliferation of epithelial cells at SCJ in different combinations, images were taken at 40x magnification. Scalebar 50 µm.

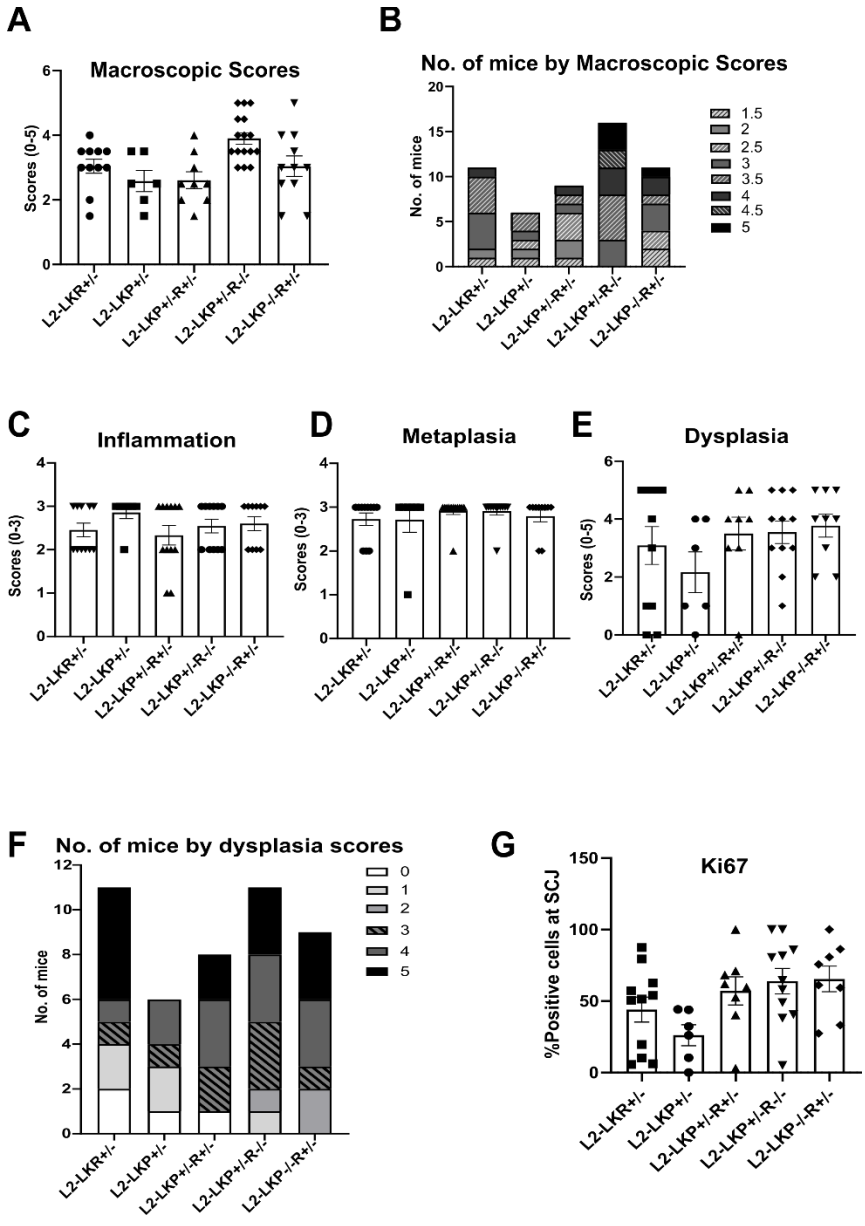

Figure 4.1.8 Statistical evaluation of KRas-mediated combinations of p53 and Rb genes: The data shows no significant difference in the (A) and (B) Macroscopic tumor extent and coverage of lesions, Histological evaluation show no difference in (C) Inflammation, (D) Metaplasia (E) and (F) Dysplasia in different combinations. (G) No difference was seen in the proliferative index of the epithelial cells at the SCJ. The data is represented as mean±SEM (****p<0.0001, ***p<0.001, **p<0.01, *p<0.05). Multiple comparison t-test was used for analysis.

The pictorial representation shown in Figure 4.1.9 depicts that in the state of inflammation, progenitor cells expand at the squamo-columnar junction; one of these progenitor cells are Lgr5+ stem cycles.

In our inflammation-based BE model with the overexpression of IL-1b, we selected Lgr5+ cells as cre to induce KRas, p53 and Rb mutations.

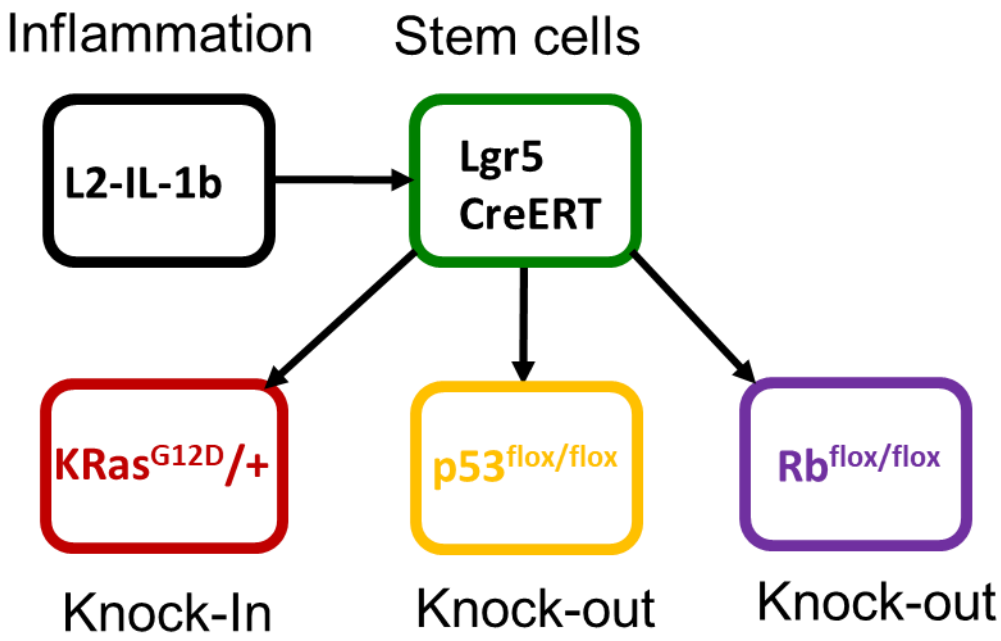

Figure 4.1.9 Schematic representation of the L2-LKPR mouse model for EAC: L2-IL-1b causes inflammation at the SCJ, Lgr5 are the progenitor cells cycling at SCJ, KRas activation and p53 and Rb inactivation in the Lgr5 cells induces EAC.

4.2 Analysis of cell death and the tumor microenvironment

Mutations cause stress in the cellular functions. This stress is mostly reflected via DNA damage as DNA in a cell is the reservoir of mutational changes. To examine this stress-related cellular response, we analysed the cardia region for the expression of y-H2AX across different genotypes, as shown in Figure 4.2.1. A and F. As observed here, L2-L, L2-LR and L2-LP, L2-LK and L2-LPR mice show very low positivity for y-H2AX. These mice displayed metaplastic and well-differentiated cells, but they have chronic inflammation, which is one of the prime reasons for the presence of few cells with DNA damage in these cohorts. However, the KRas-driven groups coupled with p53 and Rb co-inactivation, i.e., L2-LKP, L2-LKR and L2-LKPR, showed a comparatively higher percentage of DNA damage. This change was significantly more compared to the L2-L cohort. This data showed that due to a high mutational burden, the changes in the epithelial cells were beyond repair, which led to cell death.

p53 and Rb are two important cell cycle regulators. p53 has been pointed out to play a key role in the mechanism involved in initiating DNA damage. Hence, we examined the role of p53 and its target gene, p21, in our mice cohorts. We performed immunohistochemistry and calculated percentage positivity with respect to the cardia region. As represented in Figure 4.2.1 B and C, the control L2-L cohort showed no positivity for either p53 or p21 marker. However, the L2-LR group had a very low positivity rate. This could be explained because of the low proliferation rate of epithelial cells in this group.

Furthermore, a considerable number of positive cells were observed in the L2-LK cohort. This is a notable feature of this group that even though L2-LK mice are either non-dysplastic or at an early dysplastic stage, it still displays the potential to advance to EAC [101]. p53/p21 protein expression in these tissues is a mark of such progression. Adding on, the L2-LKR cohort also expressed p53 and p21, showing that mutant p53 gets activated at advanced tumor stages as well. The cells which show the accumulation of the protein go into senescence which leads to apoptosis. It is also evidence for the activation of DNA damage response.

Moreover, a very low to a negligible expression of p53/p21 markers was observed in L2-LP, L2-LPR, L2-LKP and L2-LKPR; this was because, in all these cohorts, p53 alleles were knocked out. This is also proof of the p53 knock-out in the mouse model. However, there was still some protein expression observed. This is because the conditional alleles of p53 have been inactivated in only Lgr5+ cells. And this knock-out in a few Lgr5+ cells present in the cardia is enough to induce cancer. To conclude, p53 and p21 immunoreactivity showed strong concordance in all the groups, which is also reflected statistically in the graphs in Figure 4.2.1G and H.

DNA damage and p53 accumulation are directly related to cell death; hence we investigated the rate of apoptosis in these mice. The single transgenics, as well as L2-LPR groups, showed no significant number of apoptotic cells. However, KRas-associated groups, L2-LKR, L2-LKP and L2-LKPR, showed a significantly higher number of apoptotic cells when compared with the L2-L group. Strikingly, there was a significant increase in the apoptotic cells in L2-LKPR compared to the L2-LK cohort. This shows that KRas alone may not be able to drive the tumorigenesis, but it needs to be combined with other mutations for the progression of the disease, as shown in Figures 4.2.1D and I.

Apoptosis, DNA damage and pathways leading to cell death creates a tumor niche around the epithelial tissue. Cancer-associated fibroblasts are an integral part of this niche. Hence, to observe the fibrosis around the tumor tissue, we performed immunohistochemistry for a-SMA, a known fibroblast marker. As seen in Figures 4.2.1E and J, the fibrotic tissue around the tumor increases

with the severity of the mutations and the progression of the disease. The single transgenics have low a-SMA+ fibroblasts positivity compared to control L2-L.

Furthermore, L2-LPR also did not show a considerably high amount of fibrosis. However, L2-LKP, L2-LKR and L2-LKPR showed a significantly high fibroblast positive region around the tumor epithelial tissue. This indicates that the increase in the aSMA+ fibroblasts in the tumor microenvironment correlates with increased dysplasia with mutation combinations.

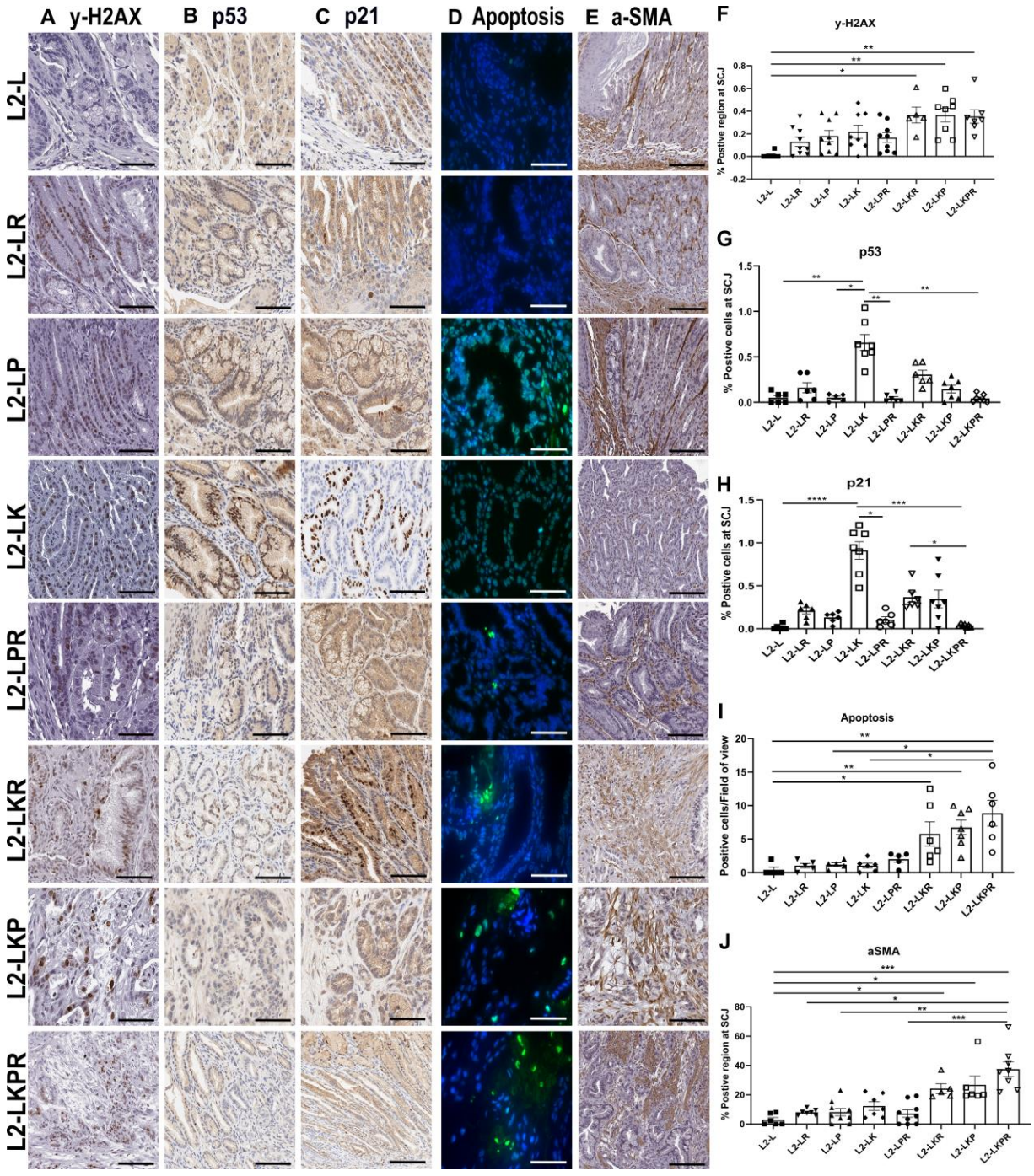

Figure 4.2.1 Analysis and evaluation of tumor microenvironment and DNA damage of the epithelial cells: (A) DNA damage at the SCJ evaluated by y-H2AX immunohistochemistry, (B) Immunohistochemistry of p53 protein expression, (C) Immunohistochemistry of p21 protein expression at SCJ, (D) TUNEL assay performed to mark apoptotic cells, (E) Immunohistochemistry for a-SMA to mark fibroblasts in the SCJ. All the images were taken at 40X. Scalebar 50 µm. Quantification of epithelial cells for (F) y-H2AX, (G) p53, (H) p21, (I) Apoptosis and (J) a-SMA immunohistochemistry at the SCJ (n=6). The data is represented as mean±SEM (****p<0.0001, ***p<0.001, **p<0.01, *p<0.05). Multiple comparison t-test was used for analysis.

For a diverse analysis of the tumor microenvironment, we evaluated the status of immune cell infiltration in different genotypic cohorts. Malignant cells recruit immune cells such as neutrophils, macrophages, myeloid-derived suppressor cells (MDSCs) to the tumor niche. These immune cells are known to support a pro-invasive and immunosuppressive phenotype [44, 102]. To analyse the population and distribution of immune cells, we used flow cytometry (FACs). We classified the immune cells into three groups: Myeloid cells, T-cells and NK cells. Myeloid cells contained subsets of neutrophils which are the first line of defence in the innate immune system [103], macrophages, which play a critical role in the maintenance of inflammation [104] and immature myeloid cells (IMCs), which are the precursors of antigen-presenting cells and are involved in the mechanism of immune suppression [105]. The T-cells were divided into subsets of T-Helper cells (Th) and Cytotoxic T-cells (Tc). We also analysed NK cells as they contribute to protecting the immune system against malignant cells [106]. The samples were prepared from the cardia region of the stomach, which is also the tumor site for the L2-LKPR mouse model. A gating strategy to mark these cell populations have been shown in Figure 4.2.2. All the cell populations were defined from the CD45+ expressing cell population to mark the leukocytes. Although we investigated an array of immune cells, no significant difference was obtained in any subsets as plotted in the graphs in Figure 4.2.3.

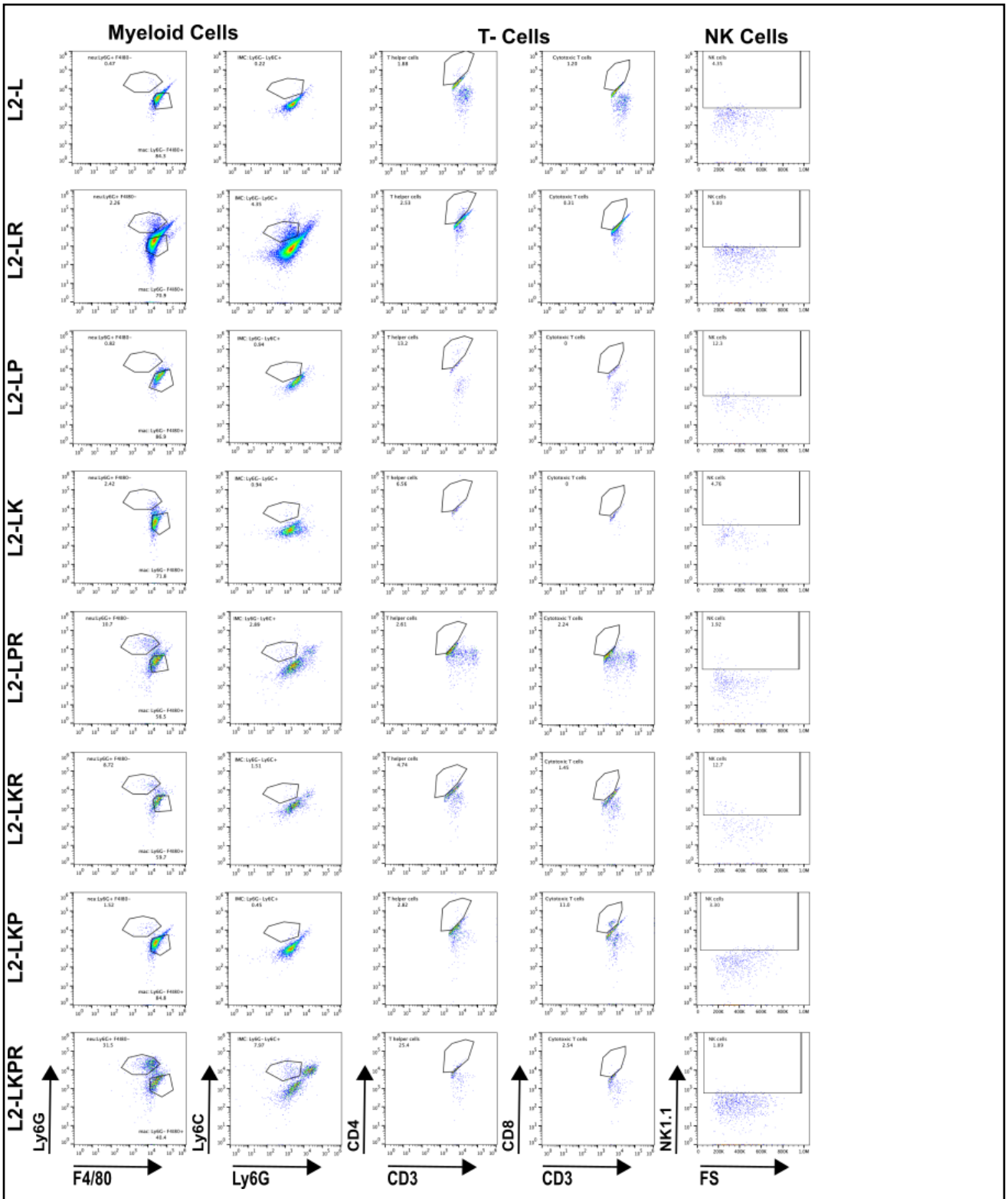

Figure 4.2.2 Immune cell infiltration is similar for different mutational combinations: Representative images of myeloid cell population neutrophils, macrophages and immature myeloid cells, T-cell subtypes T-Helper cells and Cytotoxic T-cells and NK cell population in the cardia region.

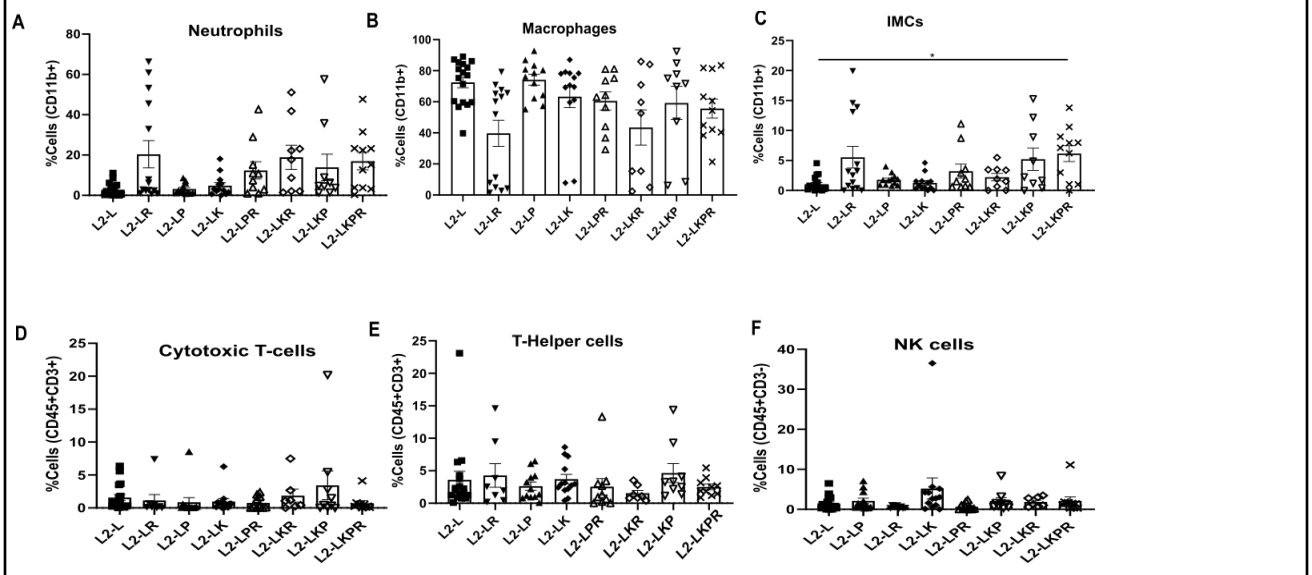

Figure 4.2.3 Statistical evaluation of immune cells: Quantification of (A) Neutrophils, (B) Macrophages, (C) Immature myeloid cells (IMCs), (D) Cytotoxic T-cells, (E) T-Helper cells and (F) NK cells (n=7-17). The data is represented as mean±SEM (****p<0.0001, ***p<0.001, **p<0.01, *p<0.05). Multiple comparison t-test was used for analysis.

4.3 In-vitro organoid system mimics the in-vivo mutations

The tumor niche draws a lot of support from its microenvironment. This microenvironment is known to help the epithelial cells to grow and develop tumorigenesis. This integration of different cell types creates a very heterogeneous microenvironment wherein it becomes difficult to understand the mechanism and responses of tumor epithelial cells and to differentiate between their functioning uninterrupted by different cell types. Hence, to create a more homogenous culture of epithelial cells, we cultured organoids from the cardia region, where we observed the macroscopic and microscopic changes due to the mutations.

Figure 4.3.1 shows a comparison of organoids in different genotypes microscopically. Small node-like structures protruding from the organoids were observed in KRas mutated groups (shown in red) in the microscopic data. To further classify this feature, we embedded the organoids and performed hematoxylin and eosin staining to understand the organoids at a histopathological level. The histopathology of organoids from the cohorts revealed that the structure of the cells and the placement of the nucleus is different for different genotypes. This arrangement correlated with the different stages of the disease driven by a particular mutation or combination of mutations.

As shown in the in-vivo data that different groups have different proliferation rates, we also analysed the organotypic epithelial cells for the same. Herein, we also observed different rates of proliferation which supported the in-vivo data. Another important aspect of the in-vivo analysis was the DNA damage in the epithelial cells. To confirm that this DNA damage response was due to the mutations and not because of the surrounding stromal or immune cells, we stained the organoids for y-H2AX. The results showed that DNA damage occurred due to the changes in the epithelial cells themselves and was not influenced by the microenvironment, as seen in Figure 4.3.1.

Statistical quantification of the data showed an increasing trend of growth of the organoids. Moreover, the p53 and Rb knock-out groups L2-LR, L2-LP and L2-LPR did not show a change from the control L2-L group. The KRas activation groups, L2-LK, L2-LKR, L2-LKP and L2-LKPR, showed a comparatively higher number of organoids than the control group. Although there was an increase in the growth of the KRas-mediated organoids, there was no significant difference seen in the size of the organoids. The histopathological screening of the organoids demonstrated a strong tumor phenotype in the L2-LKR, L2-LKP and L2-LKPR groups. The overall scores were significantly higher than the control group where only initiating columnar phenotype was observed. For all the other groups L2-LR, L2-LP, L2-LK and L2-LPR, an amalgamation of columnar and apoptotic cells was seen in the organoid histology.

Further, a comparison of the number of mice plotted against the histology scores. This also corroborated with the above analysis and showed that the highest scores representing the tumor phenotype existed in the mice in KRas-activated double and triple transgenic groups. However, the L2-LK group only achieved apoptotic cell formation. This notable point proves that in this mouse model, KRas is an important driving factor, but it cannot achieve a tumor phenotype on its own and hence needs to be combined with more mutations to drive the disease. Proliferation and DNA damage statistics also correlated with the histology findings, which showed more proliferation in L2-LKR, L2-LKP and L2-LKPR organoids. Moreover, there was a significant increase in proliferating cells in L2-LKPR mice compared to single transgenics L2-LR and L2-LP, double transgenic L2-LPR, and control. In y-H2AX also there was a significant rise in DNA damage in L2-LKPR organoids compared to single transgenics L2-LR, L2-LP and control L2-L.

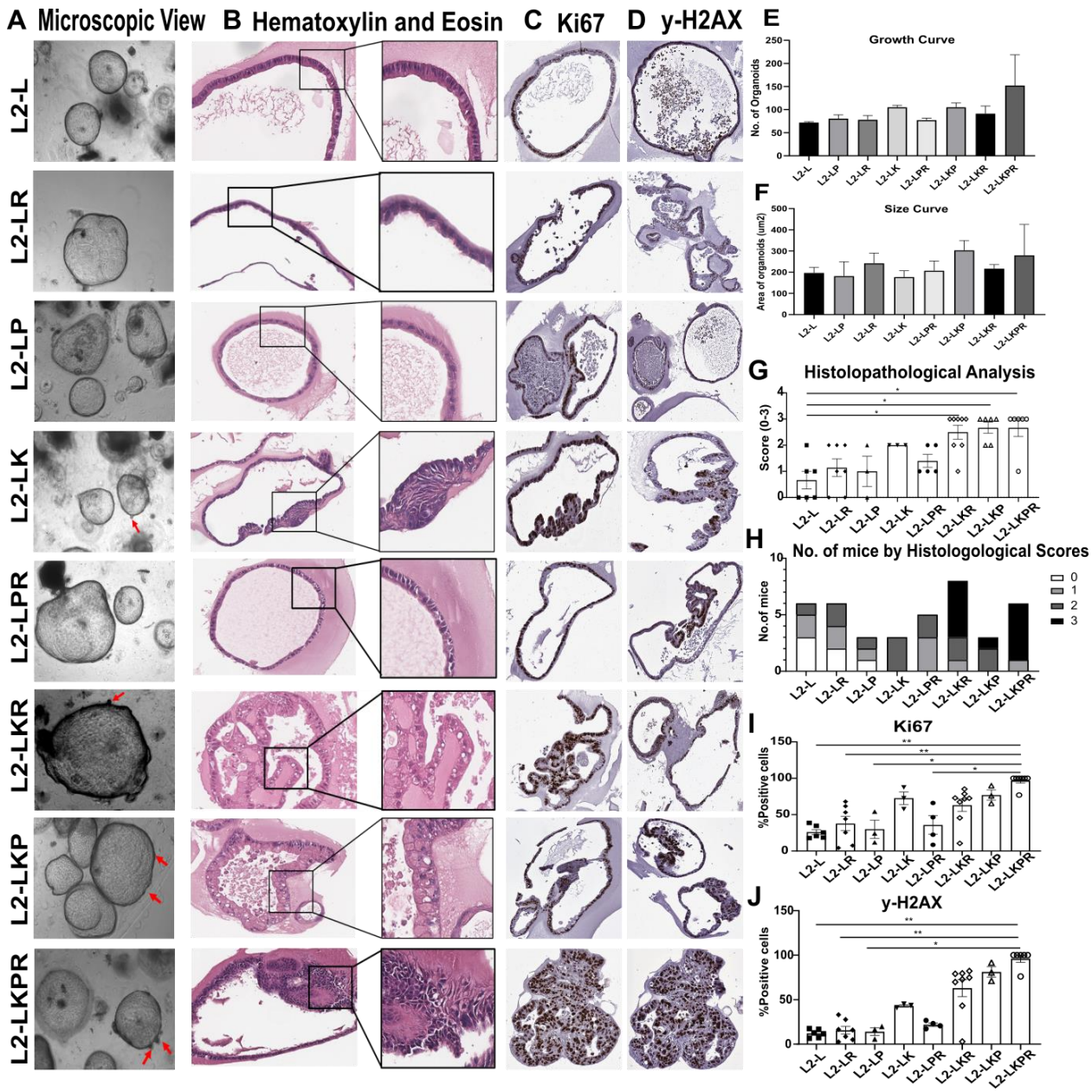

Figure 4.3.1 In-vitro organoid model mimics the in-vivo characterization of different mutations: Representative images of (A) Microscopic view of organoids which the indication of proliferating nodes (in red), the images were taken at 5X, (B) Histology of organoids from different mutations, images were taken at 20X, and 40 X, (C) Ki67 immunohistochemistry for the proliferation, images were taken at 40X, (D) y-H2AX immunohistochemistry for DNA damage, images were taken at 40 X. Statistical evaluation of the (E) Organoid number (n=3-7), (F) Size (n=3-7), (G) Histopathological scoring (n=3-7), (H) Distribution of histology scores according to the number of mice per genotype (n=3-7), (I) Proliferation of epithelial cells through Ki67 marker (n=3-7) and (J) DNA damage cell count through y-H2AX marker (n=3-7). The data is represented as mean±SEM (****p<0.0001, ***p<0.001, **p<0.01, *p<0.05). Multiple comparison t-test was used for analysis.

Apart from the homozygous knock-out of p53 and Rb alleles, we also analysed the heterozygous-homozygous combinations with double and triple transgenics. As demonstrated in Figure 4.3.2 and Figure 4.3.3, we did not observe a change in the formation and growth of L2-LP+/-R+/-, L2-LP+/-R-/- and L2-LP-/-R+/- organoids among the groups. The histological grading also showed only 50% (2/4) of the mice with an undifferentiated phenotype in L2-LKP+/-R-/- and L2-LKP-/-R+/- organoid groups. However, all the other groups showed at least columnar to utmost apoptotic cell formation. Taking this into account, we investigated the proliferation rate and the DNA damage in the cells. Although no significant difference was observed among the different groups, the KRas driven groups with L2-LKP+/-R+/-, L2-LKP+/-R-/- and L2-LKP-/-R+/- compared to non-KRas groups, showed higher proliferation and DNA damage in the epithelial cells. This data corroborates very well with the in-vivo findings for these respective groups.

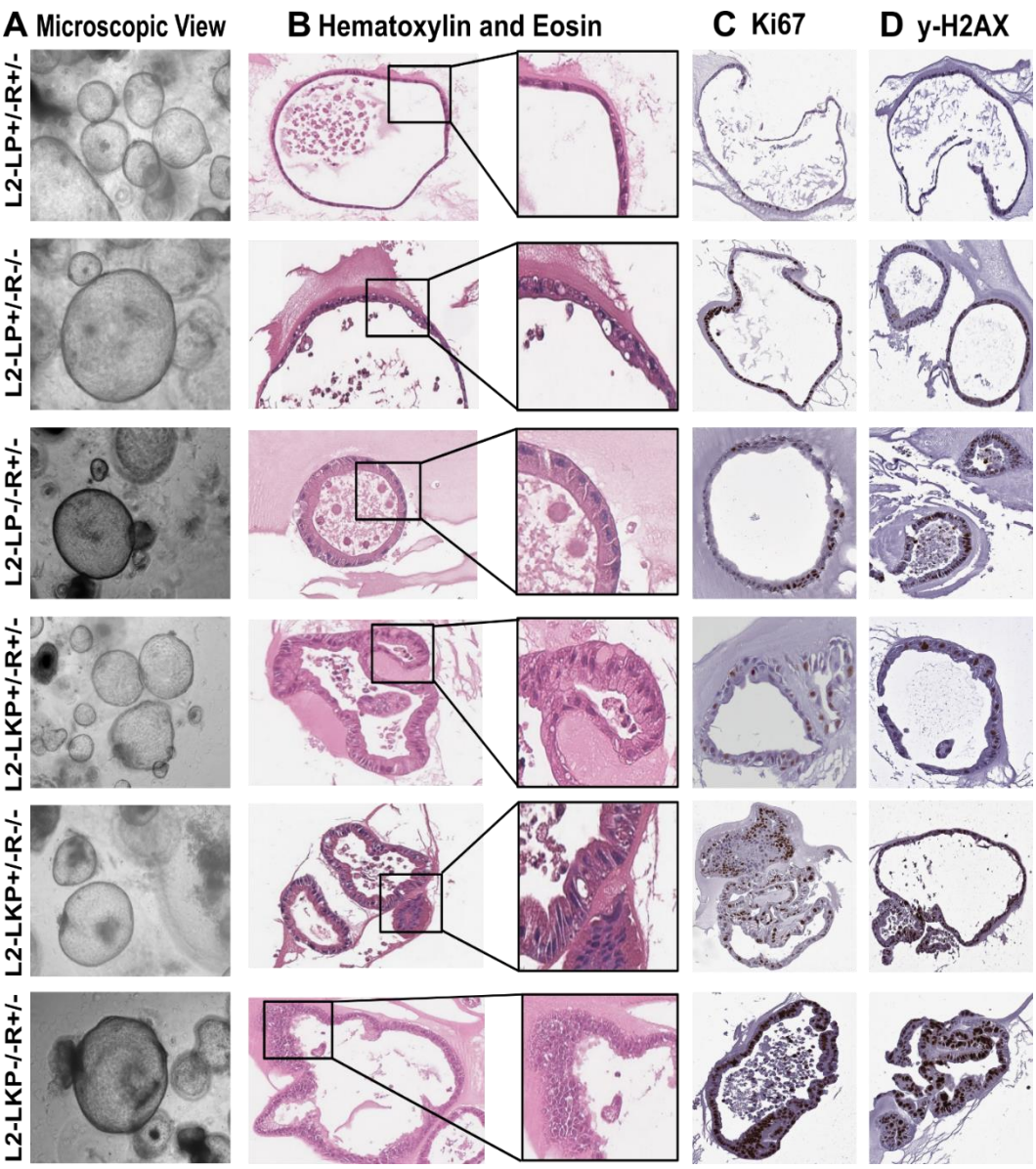

Figure 4.3.2 Heterozygous-Homozygous combinations of p53 and Rb genes with and without KRas highlights the findings from the in-vivo results: Representative images of (A) Microscopic view of the organoids, images taken at 5X, (B) Histological view of the structure of cells in the organoids, images taken at 20X and 40X, (C) Ki67 immunohistochemistry for proliferation, images were taken at 40X and (D) y-H2AX immunohistochemistry for DNA damage, images were taken at 40X.

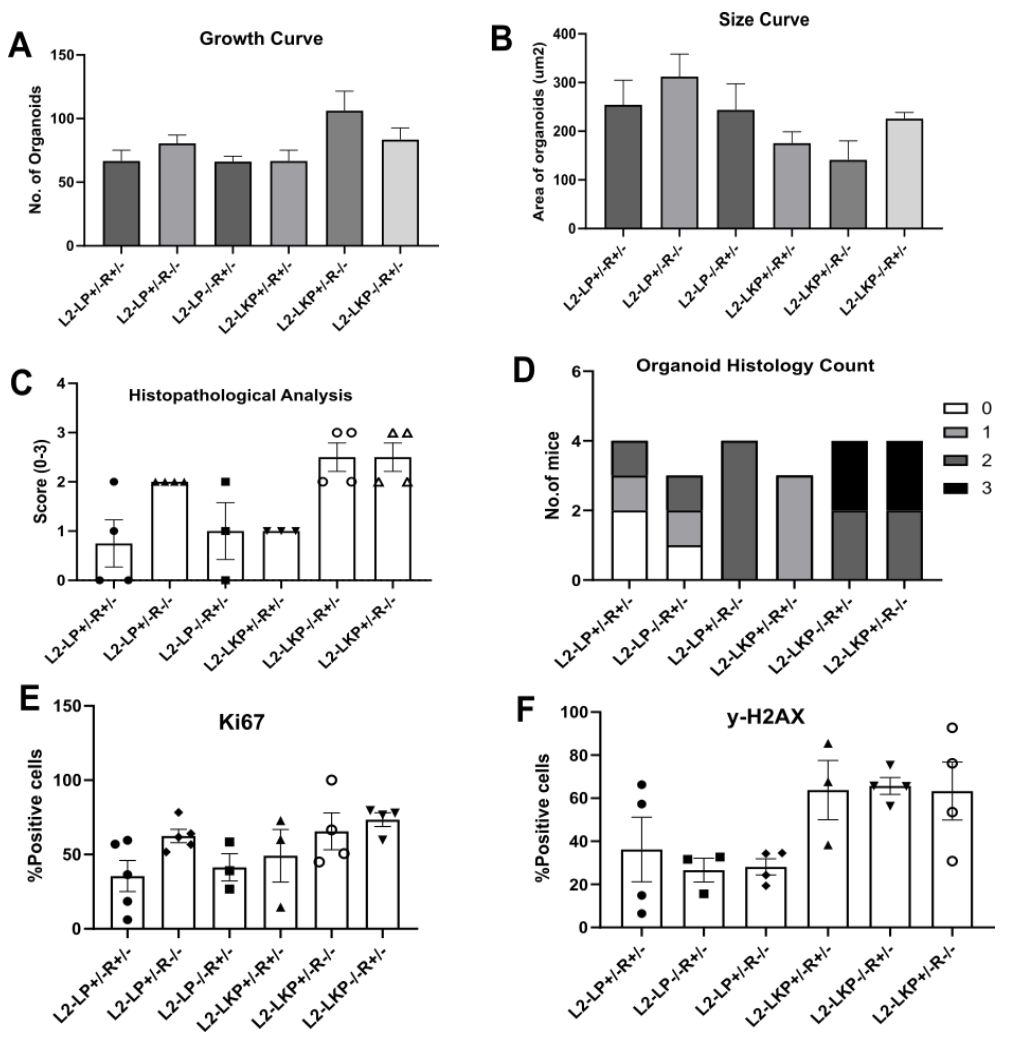

Figure 4.3.3 Statistical evaluation of the organoids with different allele combinations of p53 and Rb genes with and without KRas: (A) Organoid Growth (n=3-7), (B) Size (n=3-7), (C) Histological scoring (n=3-4), (D) Distribution of dysplasia scores across different genotypes (n=3-4), (E) Ki67 expression evaluation (n=3-5) and (F) y-H2AX expression evaluation (n=3-4). The data is represented as mean±SEM (****p<0.0001, ***p<0.001, **p<0.01, *p<0.05). Multiple comparison t-test was used for analysis.

4.4 Analysis of genetic and epigenetic changes in different mutational cohorts

P16 methylation has been noted to be one of the markers to predict the onset of cancer development. To assess the status of p16 methylation in our mice cohorts, we performed CpG methylation in the p16INK4a promoter to check for p16 inactivation. As shown in Figure 4.4.1A, we did not observe methylation in our in-vivo samples when we compared the tumor phenotype to the normal phenotype. The possible reason for this is the presence of different cell types and the tumor cells during the

tissue sampling, which could have colluded the DNA and alleviated the methylation response. To understand the role of this epigenetic silencing in our model, we isolated DNA from homogenous epithelial organoids and performed the methylation studies. As seen in Figure 4.4.1B, we observed an increasing trend of CpG island methylation from the control L2-L group to the tumor L2-LKPR group. Hence, with this observation, we could infer p16 inactivation increases in the tumor organoids and shows in effect with every mutational addition.

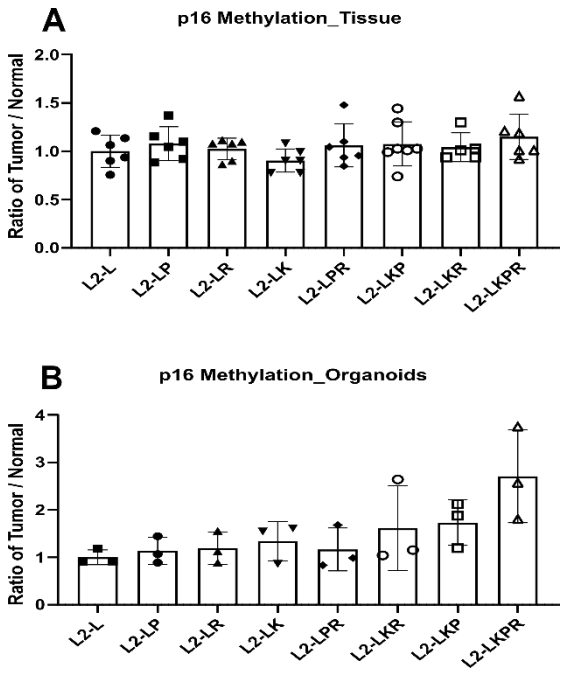

Figure 4.4.1 Epigenetic silencing in different genotypic cohorts assessed by p16 inactivation: The graphs show modulations in the expression of p16INK4A through evaluation of CpG islands 1-7 in (A) In-vivo tissue samples (n=6) and (B) In-vitro organoids across different cohorts (n=3). The data is represented as mean±SEM (****p<0.0001, ***p<0.001, **p<0.01, *p<0.05). Multiple comparison t-test was used for analysis.

To demonstrate the chromosomal instability that occurs due to different mutations' introduction, we performed low coverage whole genome sequencing. As shown in Figure 4.4.2A, the in-vivo tissue samples do not show any variation in the control L2-L, L2-LK, L2-LPR and L2-LKR mice tissue. However, there were some chromosomal aberrations observed in the chromosomal genomes of L2-LKP and L2-LKPR mice. To investigate the changes in the epithelial cells, we used epithelial 3D organoids isolated from the cardia region. In the organoids also there were no aberrations observed in L2-L, L2-LK, L2-LPR and L2-LKR groups. However, strong chromosomal abnormalities were observed in L2-LKP and L2-LKPR groups indicated by the deviation from the mean (Figure 4.4.2B). To quantify these aberrations, the total number of copy number changes were determined and

plotted according to different genotypes. As the graphs are shown in Figure 4.4.3A, the copy number variations in tissue samples do not show any significant changes. This does not mean that there are no changes observed in the tissue samples. With different mutations, there is a possibility that the tissue resected for DNA isolation also includes DNA from the normal regions and the DNA from the neighbouring cell types of the tumor microenvironment. The normal DNA compensated for the alterations of the tumor DNA. However, to resolve this issue, we evaluated the copy number variations in the epithelial organoid samples. These samples showed us an increasing trend of copy number variations of L2-LKPR organoids compared to L2-L organoids. Furthermore, there was a significant difference in the copy numbers observed in L2-LKP organoids compared to L2-L organoids, as observed in Figure 4.4.3B.

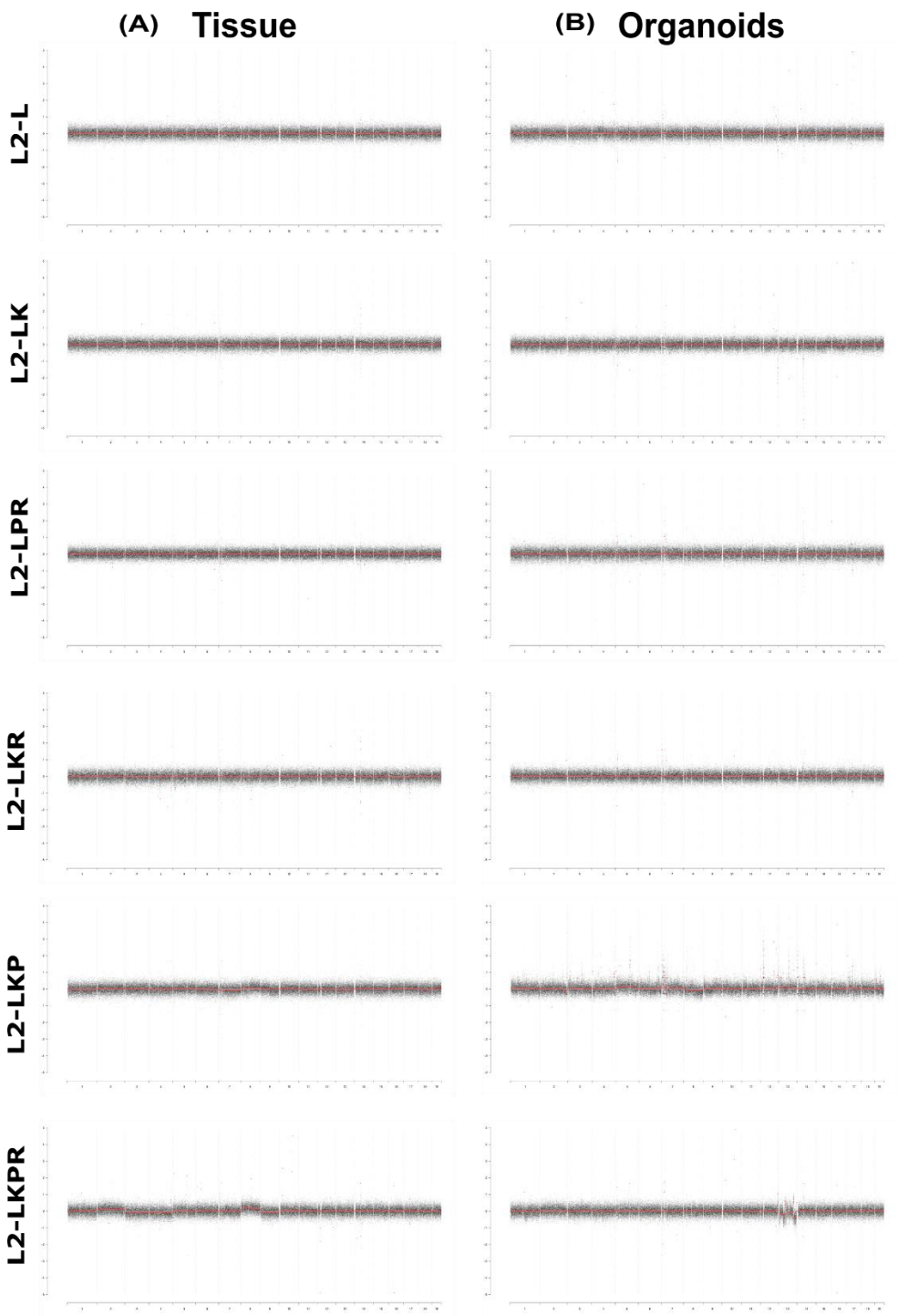

Figure 4.4.2 Chromosomal view of the copy number variations: Chromosomal instability demonstrated by the changes in the chromosome at different loci in (A) In-vivo tissue samples and (B) In-vitro organoid samples.

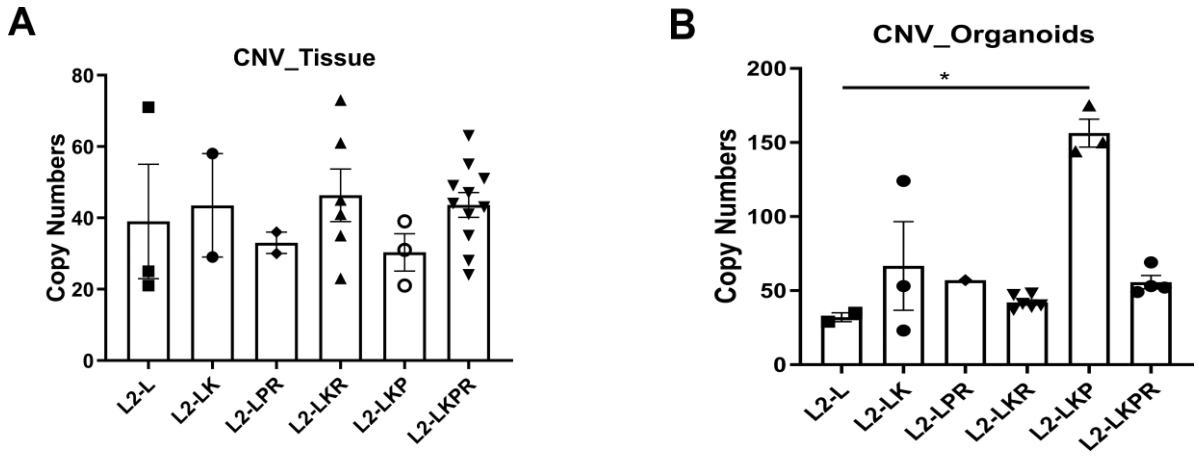

Figure 4.4.3 Statistical evaluation of the copy number changes: (A) Copy number variations in tissue (n=3-11) and (B) Copy number variations in organoids (n=1-4). The data is represented as mean±SEM (****p<0.0001, ***p<0.001, **p<0.01, *p<0.05). Multiple comparison t-test was used for analysis.

Chapter 5: Discussion

Barrett Esophagus (BE) is the replacement of the squamous epithelium with the columnar epithelium. The most common cause of BE is acid reflux, which causes inflammation at the squamous-columnar junction and damages the tissue. This damage can prolong and can lead to esophageal adenocarcinoma. Currently, BE is the only known and established precursor for EAC. The limiting factor for this disease is a late diagnosis. Although EAC is a stepwise progression disease, with the onset of inflammation which is medically termed as esophagitis, it leads to metaplasia, dysplasia and then to invasive cancer [107]. However, only a few patients progress to EAC, and it is possible that some of them may not have ever been detected with BE [15]. This creates another sub-class of non-dysplastic BE cases (NDBE). To date, there are no tools to differentiate between dysplastic and non-dysplastic progressors or even to detect progressors among non-progressors. This has been the most challenging part of EAC due to the lack of biomarkers and a deep understanding of the disease. In addition, there are only a few models to study EAC, most of which are surgical models that are difficult to replicate the disease [8, 108]. This thesis attempts to understand the disease from two perspectives: first, to understand the effect of the microenvironment on BE and second, to develop a genetic-based mutation-driven model of EAC that mimics human invasive cancer and provides a tool for future therapeutic approaches.

5.1 Effect of NF-kB elimination in stromal cells on the progression of BE

5.1.1 Role of Rel A in mediating migration of vimentin+ stromal cells to interact with epithelial cells

We know that stromal cells play a pivotal role in the tumor microenvironment. They play a role in enhancing tumor growth and invasion. However, a gap in this knowledge was to determine whether tumor growth can be regulated by altering factors and pathways in stromal cells. One of the aims of this thesis was to address this question. BE arises from repeated exposure to acid reflux which initiates a wound-healing mechanism. During this process, several cytokines such as IL-1b, IL-6 and IL-8 are upregulated. These cytokines are primarily released in the cardia region [109]. This is where the IL-1b mouse model fits in very well because, in this model, the overexpression of human IL-1b induces chronic inflammation, which is specific in the basal epithelial cells in the squamous esophagus. This chronic inflammation leads to carcinogenesis [11]. This model demonstrates the upregulation of these cytokines, which are a part of the inflammatory milieu of IL-1b mice. NF-kB has been identified as an important mediator of different cancers, including esophageal carcinogenesis

[11, 110]. These cytokines are also associated with NF-kB signalling. Hence, it is important to understand the role of NF-kB in this epithelial-stromal crosstalk.

On the one hand, where we understood the essential role of NF-kB in esophageal tumorigenesis, on the other hand, we also stipulated mediatory function of myofibroblasts which are important cell types in the stromal compartment in stimulating inflammation, tumor proliferation and angiogenesis, which contribute to tumor growth [111-113]. MFs have been identified to express proinflammatory gene expressions encoding TNF, IL-1b, IL-6 and other cytokines and chemokines, which promote tumorigenesis in an NF-kB dependent manner [114]. In this study, we demonstrated that MFs migrate to the site of inflammation and form a part of the tumor microenvironment and insinuates metaplasia and dysplasia [48, 111, 113, 114].

5.1.2 NF-kB-dependent effect on epithelial cells

In our mouse model, we observed that eliminating NF-kB in the vimentin-positive stromal cells abrogated dysplasia formation. This shows that MFs play a crucial role in a tumor-promoting environment, like in gastric cancer [48]. Hence, activated MFs can have dual functionality; either they can have a direct impact on the proliferation of epithelial cells in an NF-kB dependent manner, or they can have an indirect character leading to recruitment and polarization of adaptive and innate immune system towards a tumor-promoting phenotype [115, 116]. Another recent study showed that the inactivation of NF-kB in Lgr5 stem cells in the L2-IL-1b mouse model led to reduced proliferation and tumorigenesis. Moreover, NF-kB inactivation treatment on human and mouse organoids showed reduced growth and increased differentiation. This supports our concept that stromal activation of NF-kB is crucial for the fate of epithelial cells [113, 117]. We have also demonstrated this in our data with both humans as well as mice organoids.

The crosstalk between epithelial cells and CAFs is an essential part of tumor progression [118]. Moreover, this communication is important for the migration of the stromal cells to the tumor site and the co-existence of these two cell types together in the tumor niche. According to the literature, CAFs can induce paracrine activities by secreting growth factors and chemokines such as CXCL12, which interacts with CXCR4, which promotes cancer cell proliferation and motility of CAFs in models of EAC [119], endometrial cancer [120] and breast cancer [121]. On the other hand, in pancreatic cancer, tumor cells secrete cytokines like TGF-b, PDGF and CXCL2 to recruit and activate fibroblasts [122]. In a recent study, IL-6 has been identified as a potential mediator of crosstalk in esophageal cancer along with other cytokines RANTES, ENA-78, GRO-a, IL8 and MCP-3 in-vitro and in-vivo

[123]. Growth factor such as HGF is also known to contribute to this crosstalk in gastric cancers [124].

NF-kB is a part of the regular physiological processes in a cell. However, when it is upregulated from its normal expression levels, it instigates tumorigenesis. In several cancer types, this instigation and promotion of tumor formation are mediated by a series of cytokines involving IL-6, IL-8 which promote the migration of stromal cells towards the tumor niche. It has been demonstrated that a role reversal is possible when the activated hepatic MFs are brought to a quiescent state which causes the fibrotic liver to become normal. We used a similar concept to reprogram the activated stromal cells of the inflammatory tumor environment to form a normal stroma which could inhibit esophageal tumorigenesis. This normal stroma is capable of deregulating the signalling pathways involved in tumor growth. Our data also suggests a similar result by inhibiting the NF-kB pathway in the stromal cells, which reverses the role of fibroblasts surrounding cancer epithelial cells in-vivo and in-vitro. This reversal modifies and regresses the state of the tumorigenic epithelial cells, which is evident from the reduction in inflammation, proliferation and dysplasia in NF-kB inhibited mice.

5.1.3 Interaction of tumor microenvironment with epithelial cell compartment

The data presented in chapter 3, sections 3.1 and 3.3 shows that myofibroblasts have the potential to migrate towards the epithelial cells. This migration velocity increases when the myofibroblasts belong to the inflammatory environment of the epithelial cells. NF-kB has been known to control processes like survival, apoptosis and inflammation, but NF-kB also plays a role in promoting tumorigenesis. Therefore, it was important to see the interaction of stromal cells with the epithelial cell compartment regulated by NF-kB. In chapter 3, section 3.2, we have demonstrated that in the IL-1b.VimCre^{TM}.p65$^{fl/fl}$, the elimination of NF-kB signalling in stromal cells surrounding the BE epithelial cell population, abrogates the progression of the disease. This means that in BE, NF-kB has an important contribution to tumorigenesis, and by altering this pathway, we can stop or even reverse the disease progression.

The involvement of stromal cells has been widely studied across different cancer types such as colorectal and breast cancers. It has been well-established that the direct or indirect stromal-epithelial cell interaction can contribute to preneoplastic cell formation leading to malignancy. In colorectal cancer, it has been shown that the myofibroblasts upregulate the levels of IL-6 and IL-8, which induces differentiation in tumor-infiltrating myeloid cells, hence resulting in tumorigenesis [115]. In breast cancer, the tumor microenvironment has been identified as a key player in tumor progression. The study also suggests therapeutic strategies to normalize the surrounding stroma to modulate anti-

tumor activity by identifying protumorigenic pathways [125]. Herein, our study proves beneficial as NF-kB seems to be one such pathway that could be modulated to activate anti-tumor activity and a potential therapeutic target.

5.2 Genomic instability accelerates BE to EAC

5.2.1 Impact of inflammation on carcinogenesis

The link between inflammation and cancer is a complex relationship. From a cell-intrinsic view, it is seen as a result of genetic alterations which initiate protective inflammatory signalling that creates an inflamed microenvironment. However, from a cell-extrinsic view, it is seen as a mechanism in which infection and subsequent chronic inflammation progress towards carcinogenesis [126]. In the past years, inflammation has been accepted as one of the hallmarks of cancer [127]. Even though the cells of origin of cancer occur from genetic alterations, various environmental factors drive the malignant transformation, giving rise to a tumor niche [127]. Inflammation within the tumor microenvironment contributes to cellular proliferation and survival of malignant cells, deoxyribonucleic acid (DNA) damage, angiogenesis, metastasis, inhibition of apoptosis and reduced response to hormones and chemotherapeutic agents [128, 129]. Inflammation can promote carcinogenesis by inactivating tumour-suppressor genes or posttranslational modifications in DNA repair proteins via reactive oxygen species (ROS) [129]. Inflammation and DNA damage together contribute to mutations and cancer. This can be deduced from the fact that DNA damage during increased cell division cycles induced by inflammation-based proliferation has been shown to spike the mutation frequency [98, 130]. The correlation between inflammation and DNA damage has been demonstrated in liver cancer, where cellular transformation treated with DNA alkylating agent N-methyl-N-nitrosourea (MNU) correlated with the number of proliferating cells in the tissue [131]. Furthermore, it was shown in pancreatic cancer studies that the frequency of mutant cell populations increased with the DNA damage occurring during increased proliferation [130, 132]. Similar studies in mouse models for colon cancer have shown that introduction of DNA damage through inflammation drives mutations as well as carcinogenesis. Mice lacking BER glycosylase Aag (Aag-/-) were treated with DSS (Dextran sodium sulphate) in drinking water. The Aag-/- mice developed severe tissue damage with an increase in DNA damage compared to the wild-type mice. Sequencing the tumors revealed a point mutation in oncogenes which corresponded with mutational signatures related to inflammation [133, 134]. Similar results were observed when Aag-/- mice were treated with *Helicobacter pylori*, which is a source of gastric inflammation and carcinogenesis [135]. Similarly, in the inflammation-based model of BE, bile acid-induced DNA damage has been shown as a major component of GERD that has been linked to the development of BE metaplasia and dysplasia [11].

5.2.2 Role of mutations in causing esophageal adenocarcinoma

Barrett's esophagus is the sixth most commonly occurring disease globally. Out of which, only 0.33% of BE patients develop EAC [63]. However, this is a small number compared to the other prevalent cancer types. This disease particularly is of importance due to its poor prognosis and late detection. The availability of biomarkers and tools to differentiate between the progressor and the non-progressor patients is yet to be determined. There is a lot of scope to determine the early detection of the disease and to outline a clear treatment pathway for therapy [87].

For the past decade, there has been a lot of focus to study the disease at a molecular level and understand the genetics and the pathogenesis of EAC to develop biomarkers and use the molecular findings for precision therapies. A number of studies that have been carried out by sequencing samples from human EAC patients have led to the identification of amplification and deletions of specific genetic mutations, chromosomal variations and instability, dysregulation of pathways and a better understanding of the clonal heterogeneity [18, 24, 63, 136].

The large-scale studies on esophageal adenocarcinoma can be used to address the challenges to distinguish driver mutations from passenger mutations and to identify specific genes for tumor progression [73]. The early attempts of genomic profiling to identify somatic genetic events in the basal epithelial cells in the squamous esophagus included esophagus, colon and stomach, marked TP53, CDKN2A and RUNX1 as tumor suppressors, which were deleted in EAC. This was followed by genes involved in focal alterations such as EGFR, KRAS, CDK6 and MYC [64]. This data was supported by individual sequencing studies on EAC. These studies showed that EAC is a highly mutagenic disease. The mutational burden in EAC leads to heterogeneity of the genetic mutations, which causes several genes to mutate in small proportions; thus, it becomes difficult to define a small subset of genes driving the disease [63, 137]. However, followed by more clinical studies on chromosomal aberrations and epigenetic changes in EAC, specific genes were grouped as driver and passenger genes depending on their ability to drive the disease individually or mutually. Among these gene sets, TP53-mutant was known to be the most dominant driver in EAC, with a significant increase in the copy number variations. CDKN2A, SMAD4, CDK6, among other driver genes, were found to drive tumor progression in EAC patients. Apart from this, there have also been some driver genes clustered, which show extrachromosomal amplification such as KRas, MYC and ERBB2. It is important to identify these driver genes since they play key roles in DNA damage, signal transduction, cell cycle and chromatin remodelling [18].

5.2.3 Generation of a triple transgenic L2-LKPR mouse model for EAC

As discussed in section 1.1.4, there are several hypotheses to define the origin of BE [29]. However, our L2-IL-1B model for BE is based on the hypothesis of the expansion of progenitor cells in the gastric cardia region followed by the migration to the esophagus. Among these progenitor cells, Lgr5 was one of the most actively circulating progenitor cells and was significantly increased in BE. The functionality of Lgr5 progenitor cells in BE was also shown by lineage tracing experiments [11].

The conclusions from the sequencing studies were important to understand the genetic architecture of EAC. However, this still does not resolve the problem of the heterogeneous nature of the disease. Hence, to address this problem, we generated the triple transgenic mouse model with KRas, p53 and Rb mutations in Lgr5+ stem cells. It is important to understand that it is a controlled model system where the mutational hits may not necessarily be in all the cells. However, as we can see in the pathological findings from our L2-LKPR model, only a few hits in Lgr5+ stem cells are enough to induce invasive cancer. To generate this model, we selected the KRasG12D gene mutation. KRas is one of the most common mutations in many cancer types, including gastroesophageal adenocarcinomas [138, 139]. Although the status of KRas has been linked to the histological phenotype in gastric cancer [138]. The effect of KRas amplification is still unexplored in esophageal cancers. Here in this model, we have shown that KRas amplification by itself can induce high-grade dysplasia in 22% (2/9) cases. Moreover, when KRas amplification is coupled with double co-inactivation of tumor suppressors Tp53 and Rb, it leads to the formation of invasive cancer in mice in 93.75% (12/13) cases. This histological phenotype is similar to the cancer phenotype in human EAC patients.

From the pathological analysis, the effect of the different genes we observed that the single mutagenic transformations were able to induce dysplasia but could not lead to carcinogenesis. Hence, it was important to introduce multiple mutations. Therefore, we selected tumor suppressor genes Tp53 and Rb to introduce oncogenic signals which regulate DNA damage and cell cycle arrest pathways [140]. As observed in the screening of EAC patients, Tp53 is a highly mutated and most common driver gene in the patients [63, 73]. In gastric cancer, it has already been shown that the co-deletion of CDKN2A and Tp53 sensitizes to DNA damage blockade and can give rise to premalignant lesions [141, 142].

The CDKN2A locus consists of two gene products – $p14^{ARF}$ and $p16^{INK4A}$ [143]. Although a lot has been studied on the interaction between p53 and $p14^{ARF}$, very little is known about the functionality of p53 and $p16^{INK4A}$ interaction, which are believed to function as two parallel processes of cell cycle

regulation. Even though CDKN2A shows deletion, mutation and hypermethylation in BE, it does not progress to cancer [62, 144]. In order to study the co-inactivation of the two cell cycle pathways, we hence selected Rb, which is downstream of $p16^{INK4A}$ in the CDKN2A locus. As we can see in our findings, Rb alone cannot induce cancer; however, along with KRas amplification, the combination can progress to high-grade dysplasia and invasive cancer phenotype in 82% (9/11) cases.

Therefore, with the generation of our L2-LKPR mouse model, we inculcated a group of mutations that give us adenocarcinoma phenotype and an opportunity to explore different stages of premalignancy with specific controlled mutations. It also shows that mutational heterogeneity is pivotal to create clonal evolution of the tumor cells. The model also concludes that the more the mutational burden, the faster the disease progresses. Figure 5.2.3 shows the summary of the proposed L2-LKPR EAC mouse model.

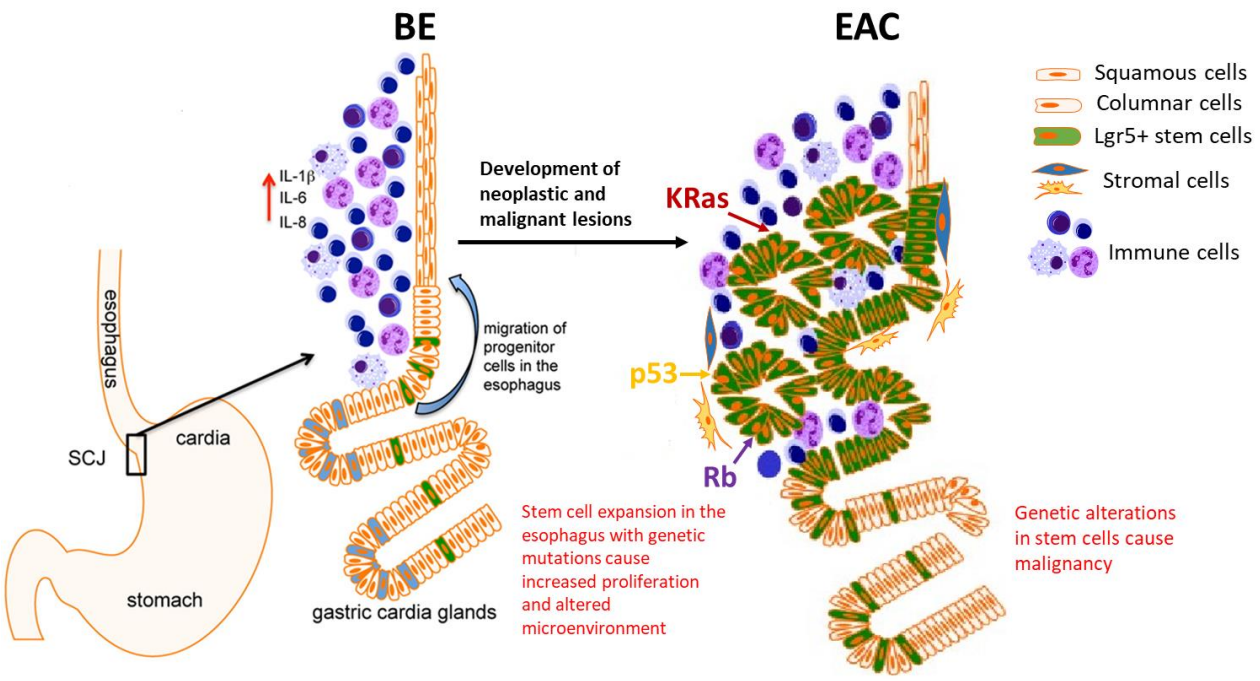

Figure 5.2.3 Proposed model for esophageal adenocarcinoma: Chronic inflammation at squamo-columnar junction (SCJ) causes progenitor cells to migrate and expand at the site of inflammation and alter the microenvironment. This induces genetic alterations such as KRas, p53 and Rb, in the stem cells causing increased proliferation and DNA damage which leads to malignancy and hence the disease progresses from BE to EAC.

5.2.4 Role of the immune microenvironment in the progression of EAC

The immune microenvironment in the L2-LKPR EAC model shows no significant difference in the various immune cell populations. However, we obtain a tumor formation even though we do not observe an escalation in different immune cells in the microenvironment. A possible explanation of this ineffectiveness of the immune microenvironment could be that the tumor formation is driven by the mutations, and the tumor microenvironment, especially the immune cells, do not have a direct effect on this progression. As previously shown in some BE models [117], we observed a cell-intrinsic interaction purely driven by the amplification and elimination of specific KRas, p53 and Rb genes which accelerated an inflammatory phenotype to a dysplastic and malignant phenotype in our mouse model. These cell-specific modulations were also supported by the 3D in-vitro organoids where there was a lack of immune environment.

Another possible explanation of no significant increase in any of the immune cell populations, including neutrophils, macrophages, IMCs, T-cells or natural killer cells, could be the concept of immune escape. This concept has been explored in solid tumors. In this phenomenon, the tumor cells develop several mechanisms of resistance such as manipulations over antigen-presenting cells via loss of MHC I or through immune tolerance, which includes upregulation of inhibitory checkpoint ligands such as PD-L1. These mechanisms develop an immunosuppressive environment in the tumour microenvironment and allow unrestrained and constitutive growth of tumor cells. However, these tumour cells can be detected clinically, but they manage to escape the body's immune system [145, 146].

Although the concept of immune escape in the L2-LKPR model is a proposed hypothesis, a more detailed study is required to prove this concept in EAC.

Conclusion and Future Perspectives

In conclusion, in this study, we characterized two BE mouse models generated on the backdrop of chronic inflammation. In the first part, we understood the role of NF-kB signalling in the tumor microenvironment. On eliminating NF-kB in vimentin+ stromal cells, we could attenuate the dysplastic phenotype to a relatively metaplastic phenotype and hence abrogates esophageal tumorigenesis. We also showed through 3D organoid co-cultures that the migration ability of the MFs could differ when they belong to different microenvironments. This difference in the ability of MFs to migrate can determine the fate of the neighbouring epithelial cells. However, we need a better understanding of the different stromal cell types and the immune environment to design better surveillance and therapeutic strategies for BE patients.

Our second mouse model is a novel design of the integration of genetic mutations to generate a study model very close to human EAC. The selection of frequently mutated genes from the knowledge of human EAC patients led to the establishment of the L2-LKPR mouse model. This model provides us with a better understanding of the development of disease. However, with our data, we were not able to characterize it as a progression model, which means we cannot point out the sequence of the occurrence of mutations.

Nevertheless, we know that KRas is one of the driver mutations which aggressively drives tumorigenesis. This also provides a tool to target the L2-LKPR model for therapeutic applications especially involving the MAPK pathways. Hence in future, we will aim to design combinatorial treatments, chemotherapeutic studies and drug screenings for preclinical trials.

Summary

In this thesis, we have generated an inflammation-based, mutation-driven transgenic L2-LKPR mouse model to study esophageal adenocarcinoma. From the various genomic, epigenomic and transcriptome studies on human EAC patients, we know that EAC is a complex and heterogeneous pool of mutations whose genetic diversity varies from patient to patient. We understand the necessity and the limitation of the L2-LKPR model; therefore, we selected the most typical and frequently occurring genetic mutations KRas, p53 and Rb, to create our mouse model.

From our study, we found out that p53 and Rb inactivation (L2-LP and L2-LR) can cause low-grade dysplasia in the epithelial cells of the squamous mucosa at SCJ at the age of 7 months. However, mutant KRas amplification (L2-LK) can accelerate the progression to high-grade dysplasia at the age of 7 months. When the complexity of the mutations was enhanced, we observed that p53-Rb co-inactivation (L2-LPR) could also cause high-grade dysplasia. On combining mutant KRas amplification with p53 inactivation (L2-LKP) and Rb inactivation (L2-LKR), we obtained invasive carcinomas at the age of 7 months. However, when we combined mutant KRas amplification with the co-inactivation of p53 and Rb (L2-LKPR), we obtained an accelerated phenotype of invasive carcinoma at the age of 6 months, which resembled the human EAC histopathologically. A schematic diagram shows the progression of the disease with each mutation in Figure 6.1. These results were in concordance with the rate of proliferation and DNA damage of epithelial cells at the SCJ for each mutation and combination. We know that these genetic alterations affect the cells intrinsically. We observed differences in the epithelial organoids cultured from different genotypes, wherein control BE organoids (L2-L) formed distinct columnar epithelial cells. p53 (L2-LP), Rb (L2-LR), KRas (L2-

LK) single mutations along with co-inactivation of p53 and Rb (L2-LPR) formed differentiated but apoptotic epithelial cells, whereas mutant KRas amplification with p53 inactivation (L2-LKP) and Rb inactivation (L2-LKR) and mutant KRas amplification with the co-inactivation of p53 and Rb (L2-LKPR) formed undifferentiated clusters of cells. This indicates that different genetic modifications impacted the growth and the behaviour of epithelial cells differently. We also saw no significant change in the population of immune cells for the different genotypes. This clearly suggests that the tumor development in this mouse model is driven by mutations and not by the tumor microenvironment and mutant KRas when combined with other mutations such as loss of p53 and Rb in our cause multi-fold acceleration in disease progression.

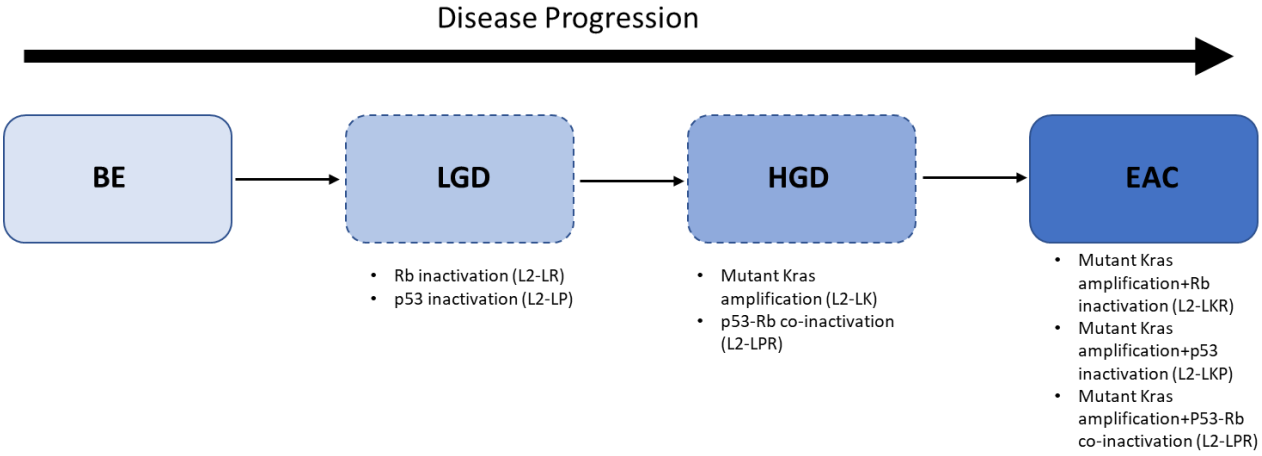

Figure 6.1 Schematic representation of different stages of the disease and the mutations complying with each stage: The diagram shows the progression of the disease from Barrett's esophagus (BE), Low-grade dysplasia (LGD), High-grade dysplasia (HGD) and Esophageal adenocarcinoma (EAC). Below there are mutations and their combinations which the particular stage of the disease.

Cdkn2a and p53 are thought to be two parallel axes of cell cycle regulation. Cdkn2a has been seen to be frequently deleted, mutated and hypermethylated in BE but may not always progress to cancer. Cdkn2a inactivation is not sufficient to progress to EAC. However, Rb has been observed to be downregulated or inactivated in most human cancers such as breast, liver and colon. In prostrate [147, 148], Rb inactivation has been identified as an early event in the development of tumors. However, our findings demonstrate that Rb could be a "late" event in the development of esophageal adenocarcinoma. Only when Rb inactivation is combined with mutant KRas amplification, it progresses to early tumor formation. These findings associate with Rb inactivation in gastric carcinoma as well [148]. Since the half-life of mutant Rb protein is more than that of the wild Rb

protein, it could be used as a possible prognostic marker for EAC and to detect the mutation in the Cdkn2a pathway.

TP53 is alteration occurs very commonly in different cancer types. It is not only found in premalignant lesions but also predicts the progression of cancer [73]. In BE, TP53 inactivation often leads to genome doubling, followed by the development of EAC [149]. However, in our mouse model, p53 seems to be a late-stage event in the development of EAC. This contradicts the findings in gastric cancer, which predicts p53 as an early event that progresses to carcinoma [101].

We know that KRas can give rise to one of the most aggressive tumors. It has been shown in our L2-LKPR EAC mouse model, as well as studies in EAC patients show that complex chromosomal alterations cause amplification of this potent oncogene [150]. In colon cancer, it has been seen that the process of crypt fission in the colon mucosa can be increased with loss of APC function or mutant KRas [151-153]. The metastatic mouse model for pancreatic cancer, which mimics the human disease, shows the role of KRas in the initiation of the disease [154, 155]. Studies also show that even in the presence of another mutation such as p53, KRas is essential for tumor maintenance [156]. This supports our observation in the L2-LKPR mouse model, where along with the loss of function of p53 and Rb, we need KRas amplification to develop tumors. Furthermore, in this modelled we analysed the effects of different mutations and their role in disease progression; however, we need a detailed study of the mechanisms to map the sequence of occurrence of these specific mutations.

References

1. Yazaki, E. and D. Sifrim, *Anatomy and physiology of the esophageal body.* Dis Esophagus, 2012. **25**(4): p. 292-8.
2. Braden, K.a.D.U., *Esophagus - anatomy and development. GI Motility online*. 2006., Nature.
3. Quante, M., J.A. Abrams, and T.C. Wang, *The rapid rise in gastroesophageal junction tumors: is inflammation of the gastric cardia the underwater iceberg?* Gastroenterology, 2013. **145**(4): p. 708-11.
4. Pandolfino, J., Kahrila PJ, *Esophageal Neuromuscular Function and Motility Disorders, in Gastrointestinal and Liver Disease*. 2016, Elsevier Saunders.
5. El-Serag, H.B., *Time trends of gastroesophageal reflux disease: a systematic review.* Clin Gastroenterol Hepatol, 2007. **5**(1): p. 17-26.
6. Dent, J., et al., *Epidemiology of gastro-oesophageal reflux disease: a systematic review.* Gut, 2005. **54**(5): p. 710-7.
7. Badillo, R. and D. Francis, *Diagnosis and treatment of gastroesophageal reflux disease.* World J Gastrointest Pharmacol Ther, 2014. **5**(3): p. 105-12.
8. Quante, M., et al., *Barrett esophagus: what a mouse model can teach us about human disease.* Cell Cycle, 2012. **11**(23): p. 4328-38.
9. Kapoor, H., et al., *Animal Models of Barrett's Esophagus and Esophageal Adenocarcinoma-Past, Present, and Future.* Clin Transl Sci, 2015(8(6)): p. 841-7.
10. Hayakawa, Y., et al., *Oesophageal adenocarcinoma and gastric cancer: should we mind the gap?* Nat Rev Cancer, 2016. **16**(5): p. 305-18.
11. Quante, M., et al., *Bile acid and inflammation activate gastric cardia stem cells in a mouse model of Barrett-like metaplasia.* Cancer Cell, 2012. **21**(1): p. 36-51.
12. Fein, M., et al., *Duodenoesophageal reflux induces esophageal adenocarcinoma without exogenous carcinogen.* J Gastrointest Surg, 1998. **2**(3): p. 260-8.
13. Munch, N.S., et al., *High-Fat Diet Accelerates Carcinogenesis in a Mouse Model of Barrett's Esophagus via Interleukin 8 and Alterations to the Gut Microbiome.* Gastroenterology, 2019. **157**(2): p. 492-506 e2.
14. Spechler, S.J., et al., *History, molecular mechanisms, and endoscopic treatment of Barrett's esophagus.* Gastroenterology, 2010. **138**(3): p. 854-69.
15. di Pietro, M., D. Alzoubaidi, and R.C. Fitzgerald, *Barrett's esophagus and cancer risk: how research advances can impact clinical practice.* Gut Liver, 2014. **8**(4): p. 356-70.
16. Barrett, N.R., *Chronic peptic ulcerz of the œophagus and 'œsophagitis'.* British Journal of Surgery, 2005. **38**(150): p. 175-182.
17. Rustgi, A.K. and H.B. El-Serag, *Esophageal carcinoma.* N Engl J Med, 2014. **371**(26): p. 2499-509.
18. Secrier, M., et al., *Mutational signatures in esophageal adenocarcinoma define etiologically distinct subgroups with therapeutic relevance.* Nat Genet, 2016. **48**(10): p. 1131-41.
19. Bird-Lieberman, E.L. and R.C. Fitzgerald, *Early diagnosis of oesophageal cancer.* Br J Cancer, 2009. **101**(1): p. 1-6.
20. Brown, L.M., S.S. Devesa, and W.H. Chow, *Incidence of adenocarcinoma of the esophagus among white Americans by sex, stage, and age.* J Natl Cancer Inst, 2008. **100**(16): p. 1184-7.
21. Bray, F., et al., *Global cancer statistics 2018: GLOBOCAN estimates of incidence and mortality worldwide for 36 cancers in 185 countries.* CA Cancer J Clin, 2018. **68**(6): p. 394-424.
22. May, M. and J.A. Abrams, *Emerging Insights into the Esophageal Microbiome.* Curr Treat Options Gastroenterol, 2018. **16**(1): p. 72-85.

23. Bresalier, R.S., *Barrett's Esophagus and Esophageal Adenocarcinoma.* Annual Review of Medicine, 2009. **60**(1): p. 221-231.
24. Frankell, A.M., et al., *The landscape of selection in 551 esophageal adenocarcinomas defines genomic biomarkers for the clinic.* Nat Genet, 2019. **51**(3): p. 506-516.
25. Coleman, H.G., S.H. Xie, and J. Lagergren, *The Epidemiology of Esophageal Adenocarcinoma.* Gastroenterology, 2018. **154**(2): p. 390-405.
26. Spechler SJ., S.R., *Barrett's Esophagus, in Gastrointestinal and Liver Disease. 2016*, E. Saunders, Editor. 2016.
27. Napier, K.J., M. Scheerer, and S. Misra, *Esophageal cancer: A Review of epidemiology, pathogenesis, staging workup and treatment modalities.* World J Gastrointest Oncol, 2014. **6**(5): p. 112-20.
28. Marcia Irene Canto, K.D., *Barrett Esophagus Progression*. 2012: John Hopkins.
29. Jiang, M., et al., *Transitional basal cells at the squamous-columnar junction generate Barrett's oesophagus.* Nature, 2017. **550**(7677): p. 529-533.
30. Tosh, D. and J.M. Slack, *How cells change their phenotype.* Nat Rev Mol Cell Biol, 2002. **3**(3): p. 187-94.
31. Sarosi, G., et al., *Bone marrow progenitor cells contribute to esophageal regeneration and metaplasia in a rat model of Barrett's esophagus.* Dis Esophagus, 2008. **21**(1): p. 43-50.
32. Barbera, M. and Rebecca C. Fitzgerald, *Cellular origin of Barrett's metaplasia and oesophageal stem cells.* Biochemical Society Transactions, 2010. **38**(2): p. 370-373.
33. Dvorak, K., et al., *Molecular mechanisms of Barrett's esophagus and adenocarcinoma.* Annals of the New York Academy of Sciences, 2011. **1232**(1): p. 381-391.
34. Leedham, S.J., et al., *Individual crypt genetic heterogeneity and the origin of metaplastic glandular epithelium in human Barrett's oesophagus.* Gut, 2008. **57**(8): p. 1041-8.
35. Wang, X., et al., *Residual embryonic cells as precursors of a Barrett's-like metaplasia.* Cell, 2011. **145**(7): p. 1023-35.
36. Corley, D.A., et al., *Abdominal obesity and body mass index as risk factors for Barrett's esophagus.* Gastroenterology, 2007. **133**(1): p. 34-41; quiz 311.
37. Lavery, D.L., et al., *The stem cell organisation, and the proliferative and gene expression profile of Barrett's epithelium, replicates pyloric-type gastric glands.* Gut, 2014. **63**(12): p. 1854-63.
38. O'Neil, A., et al., *Unique Cellular Lineage Composition of the First Gland of the Mouse Gastric Corpus.* J Histochem Cytochem, 2017. **65**(1): p. 47-58.
39. Karin, M., T. Lawrence, and V. Nizet, *Innate immunity gone awry: linking microbial infections to chronic inflammation and cancer.* Cell, 2006. **124**(4): p. 823-35.
40. Wang, J., et al., *Crosstalk between cancer and immune cells: Role of tumor-associated macrophages in the tumor microenvironment.* Cancer Med, 2019. **8**(10): p. 4709-4721.
41. Albini, A., et al., *Contribution to Tumor Angiogenesis From Innate Immune Cells Within the Tumor Microenvironment: Implications for Immunotherapy.* Frontiers in Immunology, 2018. **9**(527).
42. Melaiu, O., et al., *Influence of the Tumor Microenvironment on NK Cell Function in Solid Tumors.* Front Immunol, 2019. **10**: p. 3038.
43. Hold, G.L. and M.E. El-Omar, *Genetic aspects of inflammation and cancer.* Biochem J, 2008. **410**(2): p. 225-35.
44. Quante, M., et al., *The gastrointestinal tumor microenvironment.* Gastroenterology, 2013. **145**(1): p. 63-78.
45. Varro, A., *Stromal Cells and Tumor Microenvironment*, in *The Biology of Gastric Cancers*, T.C. Wang, J.G. Fox, and A.S. Giraud, Editors. 2009, Springer New York: New York, NY. p. 587-600.

46. Eyden, B., *The myofibroblast: a study of normal, reactive and neoplastic tissues, with an emphasis on ultrastructure. part 2 - tumours and tumour-like lesions.* J. Submicrosc. Cytol. Pathol., 2005(37): p. 109-204.
47. Serini, G., Gabbiani, G., *Mechanisms of Myofibroblast Activity and Phenotypic Modulation.* Exp Cell Res., 1999(250(2)): p. 273-83.
48. Quante, M., et al., *Bone marrow-derived myofibroblasts contribute to the mesenchymal stem cell niche and promote tumor growth.* Cancer Cell, 2011. **19**(2): p. 257-72.
49. Otranto, M., et al., *The role of the myofibroblast in tumor stroma remodeling.* Cell Adh Migr, 2012. **6**(3): p. 203-19.
50. Maeshima, A.M., et al., *Modified scar grade: a prognostic indicator in small peripheral lung adenocarcinoma.* Cancer, 2002. **95**(12): p. 2546-54.
51. Tsujino, T., et al., *Stromal myofibroblasts predict disease recurrence for colorectal cancer.* Clin Cancer Res, 2007. **13**(7): p. 2082-90.
52. Soly Wang, Z.L., Lunshan Wang & Xiaoren Zhang, *NF-kB Signaling Pathway, Inflammation and Colorectal Cancer.* Cellular and Molecular Immunology, 2009(6): p. 327-334.
53. Karin, V.B.a.M., *Signal transduction by tumor necrosis factor and its relatives.* TRENDS in Cell Biology, 2001. **11**(9): p. 372-377.
54. Bonizzi, G. and M. Karin, *The two NF-κB activation pathways and their role in innate and adaptive immunity.* Trends in Immunology, 2004. **25**(6): p. 280-288.
55. Karin, M., et al., *NF-κB in cancer: from innocent bystander to major culprit.* Nature Reviews Cancer, 2002. **2**(4): p. 301-310.
56. Richmond, A., *NF-κB, chemokine gene transcription and tumour growth.* Nature Reviews Immunology, 2002. **2**(9): p. 664-674.
57. Schulze-Bergkamen, H. and P.H. Krammer, *Apoptosis in cancer—implications for therapy.* Seminars in Oncology, 2004. **31**(1): p. 90-119.
58. Kucharczak, J., et al., *To be, or not to be: NF-κB is the answer – role of Rel/NF-κB in the regulation of apoptosis.* Oncogene, 2003. **22**(56): p. 8961-8982.
59. Luo, J.-L., H. Kamata, and M. Karin, *IKK/NF-κB signaling: balancing life and death – a new approach to cancer therapy.* The Journal of Clinical Investigation, 2005. **115**(10): p. 2625-2632.
60. Milholland, B., et al., *Differences between germline and somatic mutation rates in humans and mice.* Nature Communications, 2017. **8**(1): p. 15183.
61. Maley, C.C., *Multistage carcinogenesis in Barrett's esophagus.* Cancer Letters, 2007. **245**(1): p. 22-32.
62. Maley, C.C., et al., *Selectively Advantageous Mutations and Hitchhikers in Neoplasms.* Cancer Research, 2004. **64**(10): p. 3414.
63. Ross-Innes, C.S., et al., *Whole-genome sequencing provides new insights into the clonal architecture of Barrett's esophagus and esophageal adenocarcinoma.* Nat Genet, 2015. **47**(9): p. 1038-1046.
64. Dulak, A.M., et al., *Gastrointestinal adenocarcinomas of the esophagus, stomach, and colon exhibit distinct patterns of genome instability and oncogenesis.* Cancer Res, 2012. **72**(17): p. 4383-93.
65. Abdel-Latif, M.M.M., et al., *Inflammation and esophageal carcinogenesis.* Current Opinion in Pharmacology, 2009. **9**(4): p. 396-404.
66. O'Hagan, R.C. and J. Heyer, *KRAS Mouse Models: Modeling Cancer Harboring KRAS Mutations.* Genes Cancer, 2011. **2**(3): p. 335-43.
67. Westcott, P.M.K. and M.D. To, *The genetics and biology of KRAS in lung cancer.* Chinese journal of cancer, 2013. **32**(2): p. 63-70.
68. Seger R., K.E., *The MAPK signalling cascade.* FASEB J., 1995(9): p. 726-735.

69. Zeitouni, D., et al., *KRAS Mutant Pancreatic Cancer: No Lone Path to an Effective Treatment.* Cancers (Basel), 2016. **8**(4).
70. Jackson, E.L., et al., *Analysis of lung tumor initiation and progression using conditional expression of oncogenic K-ras.* Genes Dev, 2001. **15**(24): p. 3243-8.
71. Mullins, C.D., et al., *Germinal center B-cells resist transformation by Kras independently of tumor suppressor Arf.* PLoS One, 2013. **8**(6): p. e67941.
72. Soussi, T. and G. Lozano, *p53 mutation heterogeneity in cancer.* Biochemical and Biophysical Research Communications, 2005. **331**(3): p. 834-842.
73. Stachler, M.D., et al., *Detection of Mutations in Barrett's Esophagus Before Progression to High-Grade Dysplasia or Adenocarcinoma.* Gastroenterology, 2018. **155**(1): p. 156-167.
74. Suzuki, K. and H. Matsubara, *Recent Advances in p53 Research and Cancer Treatment.* Journal of Biomedicine and Biotechnology, 2011. **2011**: p. 978312.
75. Varna, M., et al., *TP53 Status and Response to Treatment in Breast Cancers.* Journal of Biomedicine and Biotechnology, 2011. **2011**: p. 284584.
76. Marino, S., et al., *Induction of medulloblastomas in p53-null mutant mice by somatic inactivation of Rb in the external granular layer cells of the cerebellum.* Genes & development, 2000. **14**(8): p. 994-1004.
77. Al-saran, N., et al., *Zinc enhances CDKN2A, pRb1 expression and regulates functional apoptosis via upregulation of p53 and p21 expression in human breast cancer MCF-7 cell.* Environmental Toxicology and Pharmacology, 2016. **47**: p. 19-27.
78. Luan, Y., et al., *CDKN2A inhibits cell proliferation and invasion in cervical cancer through LDHA-mediated AKT/mTOR pathway.* Clinical and Translational Oncology, 2021. **23**(2): p. 222-228.
79. Bhattacharyya, S., et al., *CDKN2A-p53 mediated antitumor effect of Lupeol in head and neck cancer.* Cell Oncol (Dordr), 2017. **40**(2): p. 145-155.
80. Foulkes, W.D., et al., *The CDKN2A (p16) Gene and Human Cancer.* Molecular Medicine, 1997. **3**(1): p. 5-20.
81. Burkhart, D.L. and J. Sage, *Cellular mechanisms of tumour suppression by the retinoblastoma gene.* Nature Reviews Cancer, 2008. **8**(9): p. 671-682.
82. Viatour, P., et al., *Notch signaling inhibits hepatocellular carcinoma following inactivation of the RB pathway.* J Exp Med, 2011. **208**(10): p. 1963-76.
83. Sherr, C.J., *The INK4a/ARF network in tumour suppression.* Nature Reviews Molecular Cell Biology, 2001. **2**(10): p. 731-737.
84. MacPherson, D., et al., *Conditional mutation of Rb causes cell cycle defects without apoptosis in the central nervous system.* Molecular and cellular biology, 2003. **23**(3): p. 1044-1053.
85. Sage, J., *Targeted disruption of the three Rb-related genes leads to loss of G1 control and immortalization.* Genes & Development, 2000. **14**(23): p. 3037-3050.
86. Benaglia, T., et al., *Health Benefits and Cost Effectiveness of Endoscopic and Nonendoscopic Cytosponge Screening for Barrett's Esophagus.* Gastroenterology, 2013. **144**(1): p. 62-73.e6.
87. Contino, G., et al., *The Evolving Genomic Landscape of Barrett's Esophagus and Esophageal Adenocarcinoma.* Gastroenterology, 2017. **153**(3): p. 657-673 e1.
88. Cowie, A., F. Noble, and T. Underwood, *Strategies to improve outcomes in esophageal adenocarcinoma.* Expert Review of Anticancer Therapy, 2014. **14**(6): p. 677-687.
89. Fang, H.Y. and F.R. Greten, *Cell Autonomous and Non-Autonomous Functions of IKKbeta and NF-kappaB during the Pathogenesis of Gastrointestinal Tumors.* Cancers (Basel), 2011. **3**(2): p. 2214-22.
90. Kuraishy, A., M. Karin, and S.I. Grivennikov, *Tumor promotion via injury- and death-induced inflammation.* Immunity, 2011. **35**(4): p. 467-77.

91. Sun, S.C., *The non-canonical NF-kappaB pathway in immunity and inflammation.* Nat Rev Immunol, 2017. **17**(9): p. 545-558.
92. Ji, Z., et al., *Inflammatory regulatory network mediated by the joint action of NF-kB, STAT3, and AP-1 factors is involved in many human cancers.* Proceedings of the National Academy of Sciences, 2019. **116**(19): p. 9453-9462.
93. Troeger, J.S., et al., *Deactivation of hepatic stellate cells during liver fibrosis resolution in mice.* Gastroenterology, 2012. **143**(4): p. 1073-83 e22.
94. Mackay, F. and J.L. Browning, *BAFF: a fundamental survival factor for B cells.* Nat Rev Immunol, 2002. **2**(7): p. 465-75.
95. Bandapalli, O.R., et al., *Down-regulation of CXCL1 inhibits tumor growth in colorectal liver metastasis.* Cytokine, 2012. **57**(1): p. 46-53.
96. Kavanagh, M.E., et al., *Altered T Cell Migratory Capacity in the Progression from Barrett Oesophagus to Oesophageal Adenocarcinoma.* Cancer Microenviron, 2019. **12**(1): p. 57-66.
97. Coussens, L.M. and Z. Werb, *Inflammation and cancer.* Nature, 2002. **420**(6917): p. 860-867.
98. Kay, J., et al., *Inflammation-induced DNA damage, mutations and cancer.* DNA Repair, 2019. **83**: p. 102673.
99. Barker, N., et al., *Identification of stem cells in small intestine and colon by marker gene Lgr5.* Nature, 2007. **449**(7165): p. 1003-7.
100. Schepers, A.G., et al., *Lineage Tracing Reveals Lgr5⁺ Stem Cell Activity in Mouse Intestinal Adenomas.* Science, 2012. **337**(6095): p. 730.
101. Sethi, N.S., et al., *Early TP53 alterations engage environmental exposures to promote gastric premalignancy in an integrative mouse model.* Nat Genet, 2020. **52**(2): p. 219-230.
102. Shou, D., et al., *Suppressive role of myeloid-derived suppressor cells (MDSCs) in the microenvironment of breast cancer and targeted immunotherapies.* Oncotarget, 2016. **7**(39): p. 64505-64511.
103. Hao, S., M. Andersen, and H. Yu, *Detection of immune suppressive neutrophils in peripheral blood samples of cancer patients.* American journal of blood research, 2013. **3**(3): p. 239-245.
104. Nagatoshi Fujiwara, K.K., *Macrophages in Inflammation.* Current Drug targets - Inflammation and Allergy, 2005(4): p. 281-286.
105. Kusmartsev, S. and D.I. Gabrilovich, *Immature myeloid cells and cancer-associated immune suppression.* Cancer Immunol Immunother, 2002. **51**(6): p. 293-8.
106. Zamai, L., et al., *NK Cells and Cancer.* The Journal of Immunology, 2007. **178**(7): p. 4011.
107. Kapoor, H., et al., *Animal Models of Barrett's Esophagus and Esophageal Adenocarcinoma-Past, Present, and Future.* Clin Transl Sci, 2015. **8**(6): p. 841-7.
108. Garman, K.S., R.C. Orlando, and X. Chen, *Review: Experimental models for Barrett's esophagus and esophageal adenocarcinoma.* American Journal of Physiology-Gastrointestinal and Liver Physiology, 2012. **302**(11): p. G1231-G1243.
109. Fitzgerald, R.C., et al., *Inflammatory gradient in Barrett's oesophagus: implications for disease complications.* Gut, 2002. **51**(3): p. 316.
110. Grivennikov, S. and M. Karin, *Autocrine IL-6 Signaling: A Key Event in Tumorigenesis?* Cancer Cell, 2008. **13**(1): p. 7-9.
111. Erez, N., et al., *Cancer-Associated Fibroblasts Are Activated in Incipient Neoplasia to Orchestrate Tumor-Promoting Inflammation in an NF-kappaB-Dependent Manner.* Cancer Cell, 2010. **17**(2): p. 135-47.
112. Wang, J., et al., *The role of cancer-associated fibroblasts in esophageal cancer.* J Transl Med, 2016. **14**: p. 30.

113. Anand, A., et al., *Elimination of NF-kappaB signaling in Vimentin+ stromal cells attenuates tumorigenesis in a mouse model of Barrett's Esophagus.* Carcinogenesis, 2021. **42**(3): p. 405-413.
114. Taniguchi, K. and M. Karin, *NF-kappaB, inflammation, immunity and cancer: coming of age.* Nat Rev Immunol, 2018. **18**(5): p. 309-324.
115. Kim, J.H., et al., *The role of myofibroblasts in upregulation of S100A8 and S100A9 and the differentiation of myeloid cells in the colorectal cancer microenvironment.* Biochemical and Biophysical Research Communications, 2012. **423**(1): p. 60-66.
116. Su, X., et al., *Tumor Microenvironments Direct the Recruitment and Expansion of Human Th17 Cells.* The Journal of Immunology, 2010. **184**(3): p. 1630.
117. Kunze, B., et al., *Notch Signaling Mediates Differentiation in Barrett's Esophagus and Promotes Progression to Adenocarcinoma.* Gastroenterology, 2020. **159**(2): p. 575-590.
118. Bu, L., et al., *Biological heterogeneity and versatility of cancer-associated fibroblasts in the tumor microenvironment.* Oncogene, 2019. **38**(25): p. 4887-4901.
119. Sugihara, H., et al., *Cancer-associated fibroblast-derived CXCL12 causes tumor progression in adenocarcinoma of the esophagogastric junction.* Med Oncol, 2015. **32**(6): p. 618.
120. Teng, F., et al., *Cancer-associated fibroblasts promote the progression of endometrial cancer via the SDF-1/CXCR4 axis.* J Hematol Oncol, 2016. **9**: p. 8.
121. Orimo, A., et al., *Stromal fibroblasts present in invasive human breast carcinomas promote tumor growth and angiogenesis through elevated SDF-1/CXCL12 secretion.* Cell, 2005. **121**(3): p. 335-48.
122. Zhan, H.X., et al., *Crosstalk between stromal cells and cancer cells in pancreatic cancer: New insights into stromal biology.* Cancer Lett, 2017. **392**: p. 83-93.
123. Karakasheva, T.A., et al., *IL-6 Mediates Cross-Talk between Tumor Cells and Activated Fibroblasts in the Tumor Microenvironment.* Cancer Res, 2018. **78**(17): p. 4957-4970.
124. Wu, X., et al., *Hepatocyte growth factor activates tumor stromal fibroblasts to promote tumorigenesis in gastric cancer.* Cancer Lett, 2013. **335**(1): p. 128-35.
125. Soysal, S.D., A. Tzankov, and S.E. Muenst, *Role of the Tumor Microenvironment in Breast Cancer.* Pathobiology, 2015. **82**(3-4): p. 142-152.
126. Gales, D., et al., *The Chemokine CXCL8 in Carcinogenesis and Drug Response.* ISRN Oncol, 2013. **2013**: p. 859154.
127. Hanahan, D. and R.A. Weinberg, *Hallmarks of cancer: the next generation.* Cell, 2011. **144**(5): p. 646-74.
128. Colotta, F., et al., *Cancer-related inflammation, the seventh hallmark of cancer: links to genetic instability.* Carcinogenesis, 2009. **30**(7): p. 1073-1081.
129. Hardikar, S., et al., *Inflammation and Oxidative Stress Markers and Esophageal Adenocarcinoma Incidence in a Barrett's Esophagus Cohort.* Cancer Epidemiology Biomarkers & Prevention, 2014. **23**(11): p. 2393.
130. Kiraly, O., et al., *Inflammation-Induced Cell Proliferation Potentiates DNA Damage-Induced Mutations In Vivo.* PLOS Genetics, 2015. **11**(2): p. e1004901.
131. Maguire, S. and H.M. Rabes, *Transformation sensitivity in early S-phase and clonogenic potential are target-cell characteristics in liver carcinogenesis by n-methyl-N-nitrosourea.* International Journal of Cancer, 1987. **39**(3): p. 385-389.
132. Kiraly, O., et al., *DNA glycosylase activity and cell proliferation are key factors in modulating homologous recombination in vivo.* Carcinogenesis, 2014. **35**(11): p. 2495-2502.
133. Meira, L.B., et al., *DNA damage induced by chronic inflammation contributes to colon carcinogenesis in mice.* The Journal of Clinical Investigation, 2008. **118**(7): p. 2516-2525.
134. Yu, A.M., et al., *The Mbd4 DNA glycosylase protects mice from inflammation-driven colon cancer and tissue injury.* Oncotarget; Vol 7, No 19, 2016.

135. Parkin, D.M., *The global health burden of infection-associated cancers in the year 2002.* International Journal of Cancer, 2006. **118**(12): p. 3030-3044.
136. Cancer Genome Atlas Research, N., et al., *Integrated genomic characterization of oesophageal carcinoma.* Nature, 2017. **541**(7636): p. 169-175.
137. Dulak, A.M., et al., *Exome and whole-genome sequencing of esophageal adenocarcinoma identifies recurrent driver events and mutational complexity.* Nat Genet, 2013. **45**(5): p. 478-86.
138. Hewitt, L.C., et al., *KRAS status is related to histological phenotype in gastric cancer: results from a large multicentre study.* Gastric Cancer, 2019. **22**(6): p. 1193-1203.
139. Laszlo, L., et al., *Recent Updates on the Significance of KRAS Mutations in Colorectal Cancer Biology.* Cells, 2021. **10**(3).
140. Sherr, C.J. and F. McCormick, *The RB and p53 pathways in cancer.* Cancer Cell, 2002. **2**(2): p. 103-112.
141. Sethi, N., et al., *Mutant p53 induces a hypoxia transcriptional program in gastric and esophageal adenocarcinoma.* JCI Insight, 2019. **4**(15).
142. Fu, D.J., et al., *Gastric squamous-columnar junction contains a large pool of cancer-prone immature osteopontin responsive Lgr5(-)CD44(+) cells.* Nat Commun, 2020. **11**(1): p. 84.
143. Sharpless, N.E. and R.A. DePinho, *The INK4A/ARF locus and its two gene products.* Current Opinion in Genetics & Development, 1999. **9**(1): p. 22-30.
144. Maley, C.C., et al., *The Combination of Genetic Instability and Clonal Expansion Predicts Progression to Esophageal Adenocarcinoma.* Cancer Research, 2004. **64**(20): p. 7629.
145. Mortezaee, K., *Immune escape: A critical hallmark in solid tumors.* Life Sci, 2020. **258**: p. 118110.
146. Prendergast, G.C., *Immune escape as a fundamental trait of cancer: focus on IDO.* Oncogene, 2008. **27**(28): p. 3889-3900.
147. Phillips, S.M.A., et al., *Loss of the retinoblastoma susceptibility gene (RB1) is a frequent and early event in prostatic tumorigenesis.* British Journal of Cancer, 1994. **70**(6): p. 1252-1257.
148. Chou, N.-H., et al., *Expression of altered retinoblastoma protein inversely correlates with tumor invasion in gastric carcinoma.* World journal of gastroenterology, 2006. **12**(44): p. 7188-7191.
149. Stachler, M.D., et al., *Paired exome analysis of Barrett's esophagus and adenocarcinoma.* Nature Genetics, 2015. **47**(9): p. 1047-1055.
150. Nones, K., et al., *Genomic catastrophes frequently arise in esophageal adenocarcinoma and drive tumorigenesis.* Nature Communications, 2014. **5**(1): p. 5224.
151. Clevers, H., *At the Crossroads of Inflammation and Cancer.* Cell, 2004. **118**(6): p. 671-674.
152. Snippert, H.J., et al., *Biased competition between Lgr5 intestinal stem cells driven by oncogenic mutation induces clonal expansion.* EMBO reports, 2014. **15**(1): p. 62-69.
153. Baker, A.M., et al., *Quantification of crypt and stem cell evolution in the normal and neoplastic human colon.* Cell Rep, 2014. **8**(4): p. 940-7.
154. Aguirre, A.J., et al., *Activated Kras and Ink4a/Arf deficiency cooperate to produce metastatic pancreatic ductal adenocarcinoma.* Genes & Development, 2003. **17**(24): p. 3112-3126.
155. Hingorani, S.R., et al., *Preinvasive and invasive ductal pancreatic cancer and its early detection in the mouse.* Cancer Cell, 2003. **4**(6): p. 437-450.
156. Collins, M.A., et al., *Metastatic Pancreatic Cancer Is Dependent on Oncogenic Kras in Mice.* PLOS ONE, 2012. **7**(12): p. e49707.

Publications and Presentations

1. **ANAND, A**., FANG, H.-Y., MOHAMMAD-SHAHI, D., INGERMANN, J., BAUMEISTER, T., STRANGMANN, J., SCHMID, R. M., WANG, T. C. & QUANTE, M. 2020. Elimination of NF-κB signaling in Vimentin+ stromal cells attenuates tumorigenesis in a mouse model of Barrett's Esophagus. Carcinogenesis.

2. BARBER, G., **ANAND, A.**, KATARZYNA, O., PHELAN, J. J., HEERAN, A. B., FLIS, E., CLARKE, N. E., WATSON, J. A., STRANGMANN, J., FLOOD, B., O'NEILL, H., O'TOOLE, D., MACCARTHY, F., RAVI, N., REYNOLDS, J. V., KAY, E. W., QUANTE, M., O'SULLIVAN, J. & CREAGH, E. M. 2020. Characterizing caspase-1 involvement during esophageal disease progression. Cancer Immunol Immunother, 69, 2635-2649.

3. BAUMEISTER, T., INGERMANN, J., MARCAZZAN, S., FANG, H.-Y., OELLINGER, R., RAD, R., ENGLEITNER, T., KLEIGREWE, K., **ANAND, A.**, STRANGMANN, J., SCHMID, R. M., WANG, T. C. & QUANTE, M. 2021. Anti-inflammatory chemoprevention attenuates the phenotype in a mouse model of esophageal adenocarcinoma. Carcinogenesis, 42, 1068-1078.

4. FLIS, E., BARBER, G., NULTY, C., KEOGH, B., MCGUIRK, P., **ANAND, A.**, O'SULLIVAN, J., QUANTE, M. & CREAGH, E. M. 2021. Identification of TLR2 Signalling Mechanisms Which Contribute to Barrett's and Oesophageal Adenocarcinoma Disease Progression. Cancers, 13.

5. KUNZE, B., MIDDELHOFF, M., MAURER, H. C., AGIBALOVA, T., **ANAND, A.**, BÜHRER, A.-M., FANG, H.-Y., BAUMEISTER, T., STEIGER, K., STRANGMANN, J., SCHMID, R. M., WANG, T. C. & QUANTE, M. 2021. Notch signaling drives development of Barrett's metaplasia from Dclk1-positive epithelial tuft cells in the murine gastric mucosa. Scientific Reports, 11, 4509.

6. KUNZE, B., WEIN, F., FANG, H. Y., **ANAND, A.**, BAUMEISTER, T., STRANGMANN, J., GERLAND, S., INGERMANN, J., MUNCH, N. S., WIETHALER, M., SAHM, V., HIDALGO-SASTRE, A., LANGE, S., LIGHTDALE, C. J., BOKHARI, A., FALK, G. W., FRIEDMAN, R. A., GINSBERG, G. G., IYER, P. G., JIN, Z., NAKAGAWA, H., SHAWBER, C. J., NGUYEN, T., RAAB, W. J., DALERBA, P., RUSTGI, A. K., SEPULVEDA, A. R., WANG, K. K., SCHMID, R. M., WANG, T. C., ABRAMS, J. A. & QUANTE, M. 2020. Notch Signaling Mediates Differentiation in Barrett's Esophagus and Promotes Progression to Adenocarcinoma. Gastroenterology, 159, 575-590.

7. MUNCH, N. S., FANG, H. Y., INGERMANN, J., MAURER, H. C., **ANAND, A.**, KELLNER, V., SAHM, V., WIETHALER, M., BAUMEISTER, T., WEIN, F., EINWACHTER, H., BOLZE, F., KLINGENSPOR, M., HALLER, D., KAVANAGH, M., LYSAGHT, J., FRIEDMAN, R., DANNENBERG, A. J., POLLAK, M., HOLT, P. R., MUTHUPALANI, S., FOX, J. G., WHARY, M. T., LEE, Y., REN, T. Y., ELLIOT, R., FITZGERALD, R., STEIGER, K., SCHMID, R. M., WANG, T. C. & QUANTE, M. 2019. High-Fat Diet Accelerates Carcinogenesis in a Mouse Model of Barrett's Esophagus via Interleukin 8 and Alterations to the Gut Microbiome. Gastroenterology, 157, 492-506 e2.

8. **ANAND A,** BAUMEISTER T, INGERMANN J, STRANGMANN J, EHMER U, RAD R, WANG TC, AND QUANTE M. "465 Alteration Of Kras, Tp53 And Rb1 Signalling In Lgr5 Stem Cells Induce Invasive Cancer In The IL-1b Mouse Model Of Barrett Esophagus." *Gastroenterology* 158, no. 6 (2020): S-89. Presented at Digestive Disease Week 2020.

9. **ANAND A**, FANG H-Y, MOHAMMAD-SHAHI D, INGERMANN J, BAUMEISTER T, STRANGMANN J, SCHMID RM, WANG TC, QUANTE M. "P0524 Elimination Of Nf-Kb Signaling In Vimentin+ Stromal Cells Attenuates

Tumorigenesis In A Mouse Model Of Barrett's Esophagus". Poster presented at United European Gastroenterology 2018.

Acknowledgement

My PhD journey started in July 2016, and since then, it has been a roller-coaster ride, but a good one and I have a bunch of people to thank for it.

It is my greatest pleasure to thank Prof. Dr. Michael Quante, who opened the doors of his lab for me and gave me an opportunity to work for him and learn from him in AG Quante. I would like to thank him for his guidance, the knowledge, motivation and excitement for science and research that he instilled in me throughout my time period in the Quante lab.

I would like to thank Dr. Timothy C.Wang, who recommended me to Michael, and it is because of him, I could embark on this wonderful journey.

I am grateful to my thesis committee members, Prof. Dr. Angelika Schnieke and Dr. Guido von Figura, for the discussions and ideas they provided me during the committee meetings. I would also like to thank Dr. Krzysztof Flisikowski, Dr. Sebastian Lange, Dr. Rupert Öllinger and Dr. Katja Steiger for your collaboration and help in shaping this study.

I would like to thank Dr. Hsin-Yu Fang for introducing me to my projects, especially the extensive mouse work. I would also like to thank Dr. Jonas Ingermann and Thorsten Neuss for patiently going through my thesis and providing suggestions and revisions. A very special thanks to Thorsten Neuss for the wonderful time we spent together, especially the long hours in cell culture. It was a great pleasure to know you and your quirkiness. Further along, I would like to thank Julia Strangmann for her assistance in the mouse room. My heartfelt thank you to Theresa Baumeister for being a great labmate and a kind person, for her friendship and support. I hope we stay in touch forever. A big thank you to the new members of the Quante lab, Marcos, Donja and Sabrina. It was great fun to work with you guys. I would also like to thank my pseudo lab Tatiana, Sebastian, Junika and Jessica, for making me a part of their group. A special thank you to Dr. Katrin Böttcher for looking at my extensive FACs data and helping me out with the analysis. Thank you to Li Tran for a fantastic job during her master's thesis, her work helped me speed up my study. And a huge thank you to Andrea Proano-Vasco, for understanding my mouse work and taking my project forward and above all, for being a great colleague and an excellent addition to the group. Furthermore, thank you to Judit Desztics for her help in times when I needed the most. Thank you to Dr. Kivanc Görgülu, for the scientific discussions and constant encouragement to move forward. And a thank you to all the colleagues of II.Med.

Joanna Madej, thank you for the time we spent together, for the discussions we had, for all your help in my project, and most of all, thank you for your friendship and support!!

I am incredibly thankful to my family, my mom and dad for the positive motivation and steady support throughout my studies. Thank you for encouraging me to follow and pursue my dreams. Thank you to my mother-in-law and father-in-law for creating positive energy and having faith in me and my work. To my sister Swati and my brother Shashank, thank you guys for all your idiosyncrasies and for lightening up my mood every time I talked to both of you. I hope I could inspire you both a little to achieve your dreams and we can share each other's successes.

Last but not least, I would like to extend a huge thank you to my husband, Mohit Verma, for being the most extraordinary partner I could have asked for. Thank you for your support, for standing like a rock with me every day and every moment. Thank you for your motivation and encouragement, for the love and laughter, for all the highs and lows of life. It has been an incredible journey with you, and I am looking forward to seeing what our next adventure withholds for us.

Abbreviations

ANGPT-L3	Angiopoietin-like 3
a-SMA	Alpha-Smooth muscle actin
BAFF	B-cell activating factor
BE	Barrett's esophagus
BMDCs	Bone-marrow derived cells
BSA	Bovine serum albumin
C5	Complement component 5
CaCl2	Calcium chloride
CAFs	Cancer-associated fibroblasts
CCL11	C-C Motif Chemokine ligand 11
CCL17	C-C Motif Chemokine ligand 17
CCL19	C-C Motif Chemokine ligand 19
CCL20	C-C Motif Chemokine ligand 20
CCL22	C-C Motif Chemokine ligand 22
CCL3	C-C Motif Chemokine ligand 3
CCL4	C-C Motif Chemokine ligand 4
CCL5	C-C Motif Chemokine ligand 5
CCR2	C-C Chemokine receptor type 2
CCR5	C-C Chemokine receptor type 5
CD14	Cluster of differentiation 14
CD160	Cluster of differentiation 160
CD40	Cluster of differentiation 40
CDK	Cyclin dependent kinase
CDK6	Cyclin dependent kinase 6
Cdkn2a	cyclin-dependent kinase inhibitor 2A
CXCL1	C-X-C Motif Chemokine Ligand 1
CXCL13	C-X-C Motif Chemokine Ligand 13
CXCL2	C-X-C Motif Chemokine Ligand 2
CXCL8	C-X-C Motif Chemokine Ligand 8
CXCR3	C-X-C Chemokine receptor 3
DKK1	Dickkopf WNT signaling pathway inhibitor 1
DMEM	Dulbecco's Modified Eagle Medium
DSS	Dextran Sodium Sulphate
E2F	E2 Transcription factor
EAC	Esophageal Adenocarcinoma
EBV	Epstein-barr virus
EDTA	Ethylenediaminetetraacetic acid
EGF	Epidermal growth factor
EGFR	Epidermal growth factor receptor

EGTA	Ethylene glycol-bis(β-aminoethyl ether)-N,N,N′,N′-tetraacetic acid
ENA-78	Epithelial-derived neutrophil-activating protein 78
ERBB2	Erb-B2 Receptor Tyrosine Kinase 2
FACs	Fluorescence-activated cell sorting
FBS	Fetal bovine serum
FEF	Fetal Embryo Fibroblast
FGF1	Fibroblast growth factor 1
FGF2	Fibroblast growth factor 2
GDP	Guanosine diphosphate
GEJ	Gastroesophageal junction
GERD	Gastroesophageal reflux disease
GRO-a	Growth-regulated alpha protein precursor
GTP	Guanosine triphosphate
HAVCR	Hepatitis A virus cellular receptor
HE	Hematoxylin and eosin
HEPES	4-(2-hydroxyethyl)-1-piperazineethanesulfonic acid
HGF	Hepatocyte Growth Factor
IHC	Immunohistochemistry
IL-10	Interleukin 10
IL-13	Interleukin 13
IL-1b	Interleukin-1 beta
IL-2	Interleukin 2
IL-22	Interleukin 22
IL-23	Interleukin 23
IL-4	Interleukin 4
IL-5	Interleukin 5
IL-6	Interleukin 6
IMCs	Immature myeloid cells
KCl	Potassium chloride
KH2PO4	Potassium dihydrogen phosphate
Kras	Ki-ras2 Kirsten rat sarcoma viral oncogene homolog
LcWGS	Low coverage whole genome sequencing
LES	lower esophageal sphincter
Lgr5	Leucine rich repeat containing G protein-coupled receptor 5
L-WRN	L- Wnt3A, R-spondin 3, Noggin
MAPK	Mitogen-activated protein kinase
MCP-3	Monocyte-chemotactic protein 3
MDSCs	Myeloid derived suppressor cells
MF	Myofibroblasts
MgCl2	Magnesium chloride
MgSO4	Magnesium sulphate
MHC-1	Major histocompatibility complex 1
MMP3	Matrix metalloproteinase-3
MMP9	Matrix metalloproteinase-9

MMPs	Matrix metalloproteinases
MNU	N-methly-N-nitrosourea
MPO	Myeloperoxidase
MYC	MYC-Proto-Oncogene
NaCl	Sodium chloride
NaHCO3	Sodium bicarbonate
NDBE	Non-dysplastic Barrett esophagus
NF-kB	Nuclear Factor 'kappa-light-chain-enhancer' of activated B-cells
NK	Natural-killer cells
P/S	Penicillin and Streptomycin
PAS	Periodic Acid Schiff
PBS	Phosphate-buffer saline
PCR	Polymerase chain reaction
PD-ECGF	Platelet-derived endothelial cell growth factor
PDGF	Platelet-derived growth factor
PD-L1	Programmed death-ligand-1
PFA	Paraformaldehyde
PFPE	Paraformaldehyde-Fixed Paraffin-Embedded
PGE2	Prostaglandin E2
PIK3CA	Phosphatidylinositol-4,5-Bisphosphate 3-Kinase Catalytic Subunit Alpha
RANTES	Regulated on Activation, Normal T Expressed and Secreted
Rb	Retinoblastoma
ROS	Reactive Oxygen Species
RPMI	Roswell Park memorial Institute Medium
RT	Room temperature
SCJ	Squamous-columnar junction
SDS-PAGE	Sodium Dodecyl Sulfate-Polyacrylamide Gel Electrophoresis
SEM	Standard error mean
TAMs	Tumor-associated macrophages
Tc	Cytotoxic T-cells
TGF-β	Transforming growth factor beta
Th	T-Helper cells
TLRs	Toll-like receptors
TME	Tumor microenvironment
TNF-a	Tumor Necrosis Factor-alpha
VCAM-1	vascular adhesion molecule-1
VEGF	Vascular endothelial growth factor
WT	Wild-type